MULTIFRACTAL CHARACTERIZATION OF ELECTROMYOGRAM SIGNALS

By

Tina Ehtiati

A Thesis
Submitted to the Faculty of Graduate Studies
in Partial Fulfillment of the Requirements
For the Degree of

Master of Science

Department of Electrical and Computer Engineering
University of Manitoba
Winnipeg, Manitoba, Canada

Thesis Advisor: W. Kinsner, Ph. D., P. Eng.

January, 1999

THE UNIVERSITY OF MANITOBA

FACULTY OF GRADUATE STUDIES

*****

COPYRIGHT PERMISSION PAGE

MULTIFRACTAL CHARACTERIZATION OF ELECTROMYOGRAM SIGNALS

BY

TINA EHTIATI

A Thesis/Practicum submitted to the Faculty of Graduate Studies of The University of Manitoba in partial fulfillment of the requirements of the degree of MASTER OF SCIENCE

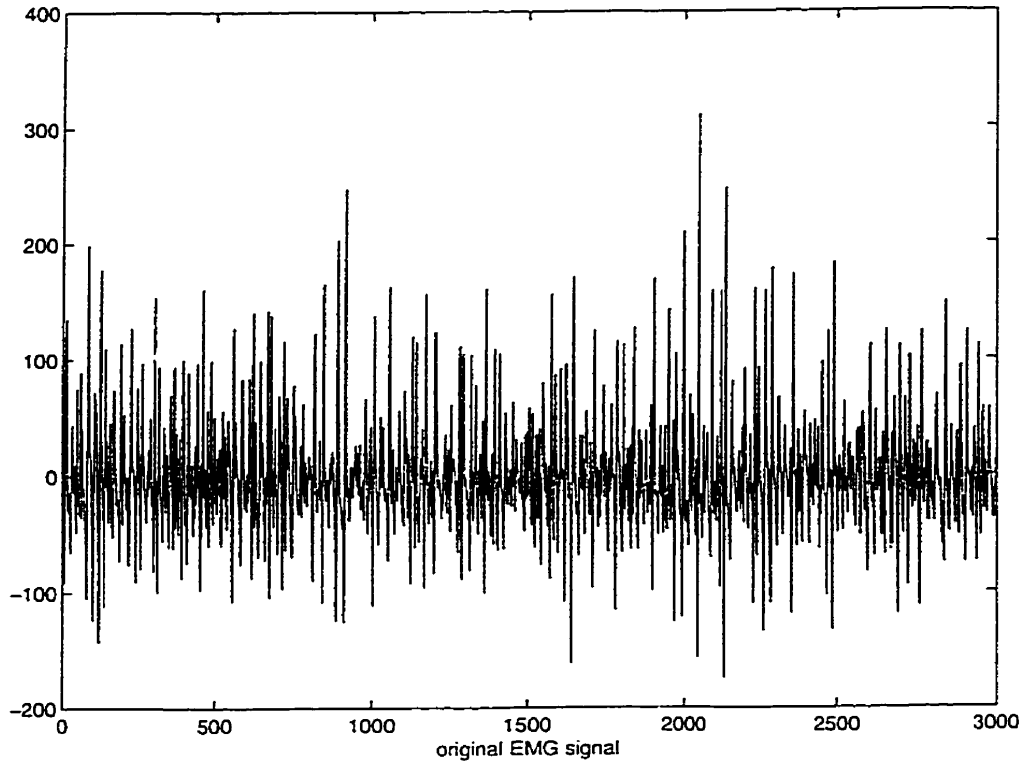
400
300
200
100
0
−100
−200
0
500
1000
1500
2000
2500
3000
original EMG signal

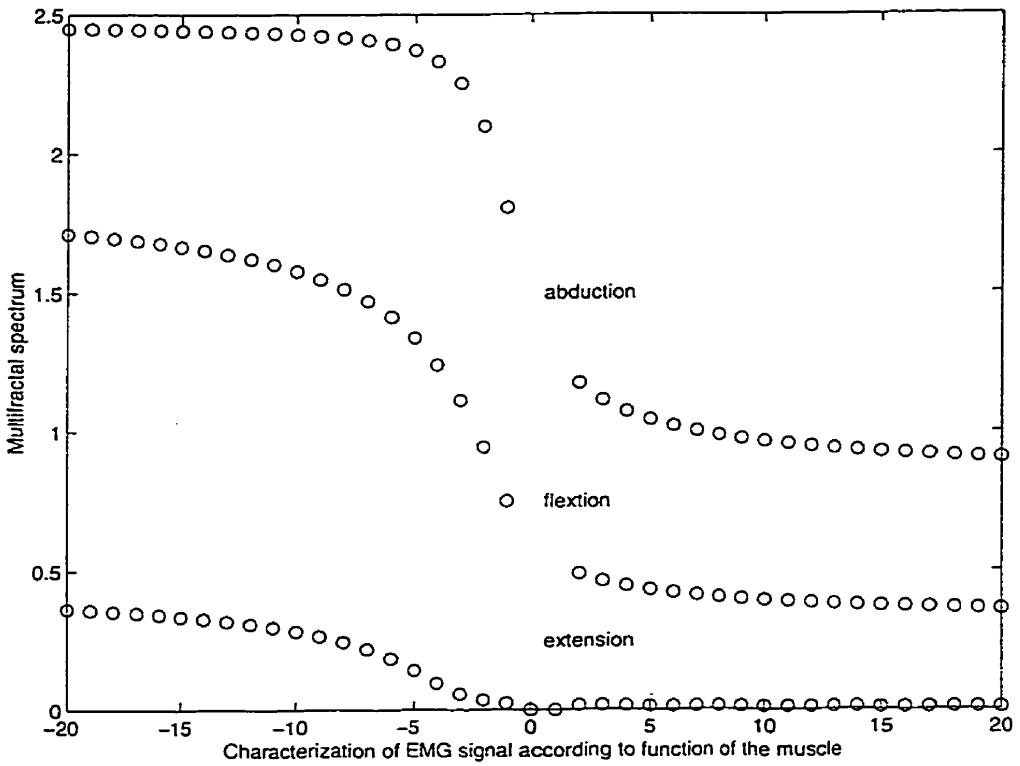
2.5
2
1.5
1
0.5
0
Multifractal spectrum
abduction
flextion
extension
−20
−15
−10
−5
0
5
10
15
20
Characterization of EMG signal according to function of the muscle

ABSTRACT

In this thesis, we present an approach to the characterization and feature extraction of the electromyogram (EMG) signals. This approach is based upon the chaotic behaviour of the EMG signals and the existence of the corresponding strange attractors with low embedding dimensions. The multifractal dimensions of the strange attractors underlying this chaotic behaviour provide alternative features for analyzing the EMG signals. The multifractal dimensions describe how the entropy of these strange attractors changes as the hypervolume scales used for calculating the entropy vary.

There are several considerations associated with the reconstruction of the strange attractors and the calculation of the multifractal dimensions from a single variable time series. We discuss how the length and the sampling rate of the time series effect the convergence of the multifractal dimensions. We also discuss the effect of high noise levels in increasing the minimum embedding dimension required for the reconstruction of the strange attractors.

The EMG signals under study have been obtained from the anterior, posterior, and middle portions of the deltoid and upper trapezius during isometric contractions, using surface electrodes. The mutlifractal dimensions of these EMG signals are between 0.5 to 1.5. The experimental results show that the positive moment orders of the multifractal dimensions of the EMG signals can be used for discriminating among three functions of deltoid, i.e. abduction, extension, and flexion. The multifractal dimensions of the EMG of the muscle as a prime mover, are 0.3 larger on average, comparing to the muscle as synergist.

ACKNOWLEDGEMENTS

I would like to thank my advisor, Dr. Kinsner for his encouragement and guidance during my studies and for his time and patience in the course of writing this thesis.

I would like to express my heartfelt thanks to Zahra Moussavi for all the support and motivation she gave me throughout my research work.

My special thanks to Richard Dansereau, Alexis Denis, and Luotao Sun for their inputs and suggestions for the preparation of this thesis.

TABLE OF CONTENTS

LIST OF FIGURES

LIST OF TABLES

LIST OF ABBREVIATIONS AND SYMBOLS

D_E Euclidean dimension

D_T Topological dimension

D_S Self-similarity dimension

D_B Box-counting dimension

D_H Hausdorff dimension

$H(\delta)$ Shanon entropy

D_C Correlation dimension

D_I Information dimension

D_q Rényi dimensions

Log Logarithm in base two.

SNR Signal to noise ratio

EMG Electromyography

RMS Root mean square value

CHAPTER I

INTRODUCTION

1.1 Motivation

Surface electromyography provides a non-invasive access to the physiological processes that cause a muscle to generate force and movement. Since 1950, researchers have used the elecromyogram (EMG) signals for various academic and clinical applications. The EMG signals can be used as indicators of muscle contraction, timing of muscle performance, force contributions of individual muscles and as a fatigue index, and are useful in studying both normal and abnormal muscle functions.

There are many clinical applications of electromyography. For example Wolf *et al.* [WoNK82] used EMG biofeedback techniques in the assessment and treatment of lower back pain. Budzynski *et al.*[BSAM73] used EMG feedback technique to treat muscle contraction headaches. Lewit [Lewi91] detected the occurrence of upper quarter myalgias and the reasons of their occurrence using EMG signals. More recently electromyography has also been used in the diagnosis and treatment of neurological disorders [HGRG96]. For example, studies of Stocchi *et al.* [SCIM97] and Chandirama *et al.* [ChPF97] shows the possibility of detection and evaluation of Parkinson's disease and multiple system atrophy using EMG signals. Michelangelo *et al.* [MiCR98] have studied the relation of early development of fatigue in hand muscles of patients with chronic heart failure using electromyography.

One of the most interesting applications of the electromyography is to use the EMG signals in order to activate an artificial limb. The desired scheme is to connect the control system of the artificial limb directly to the remaining portions of the nervous

system of the amputated limb [GrSZ85].

The field of surface electromyography suffers from some limitations which are inherent in the acquisition instruments and analysis methods used for studying EMG signals. The majority of the studies of the EMG signals are based upon the analysis of stochastic temporal characteristics and frequency domain power spectrum characteristics of the EMG signals.

The recent experimental results have shown that EMG signals are not white Gaussian noise but that they exhibit a chaotic behaviour and can be characterized as a chaotic phenomenon. This discovery opens up new possibilities in the study and quantitative analysis of EMG signals. Anmuth *et al.* [AnGM94] calculated the correlation dimension of electromyographic signals recorded from surface electrodes during isometric contractions. Their study has shown that the fractal correlation dimension is linearly correlated with muscle activation. Gilter and Czerniecki [GiCz95] have studied the correlation dimension of the electromyogram with varying force. They show that the correlation dimension of the EMG signals is highly correlated with force. Erfanian *et al.* [ErCH97] have studied the relation of the chaotic activity of electrically stimulated paralysed muscle and the relation of the correlation dimension with the development of fatigue in these muscles.

In this thesis we study the chaotic characteristics of the EMG signals and examine the capability of the multifractal measures for characterizing EMG signals. The chaotic behaviour of the EMG signals is associated with the existence of strange attractors with low embedding dimensions. These strange attractors bound the temporal trajectories of the EMG in the phase spaces reconstructed from these single variable signals. The

multifractal dimensions describe how the entropy of these strange attractors changes as the hypervolume scales used for calculating the entropy vary. Such multifractal techniques [Kins94] have proven to be successful in the examination of a wide range of noise-like but chaotic signals such as radio signals and speech signals [Shaw97][Grie96][Lang96].

1.2 Thesis Statement and Objectives

The objective of this thesis is to show the existence of strange attractors with low embedding dimensions in the phase spaces reconstructed from single variable temporal EMG signals, and to calculate the multifractal dimensions of these strange attractors.

Established methods such as generalized correlation integral [PaSc87] [AtSV88] [GrPr83a][GrPr83b], delay reconstruction of strange attractors [PCFS80], and minimum mutual information criterion [FrSw80], are used for the calculation of the multifractal dimension of the EMG signals.

The signals used in this thesis are recorded from isometric contractions of deltoid and trapezius muscles in three functionalities of shoulder abduction, extension, and flexion. We will determine how the multifractal dimensions can be used to quantify and capture the essence of the complexity of the motor unit recruitment patterns in the three different functions of deltoid and trapezius.

1.3 Thesis Organization

This thesis is organized in seven chapters. Chapter 2 gives a brief review on the anatomical and physiological aspects of the muscle contraction and EMG sources. Chapter 3 provides a general introduction to fractals, chaos, strange attractors, morphological and complexity measures, and multifractals. Chapter 4 contains the theoretical basis for reconstructing strange attractors from a single variable time series and

the calculation of the multifractal dimensions from the reconstructed attractor. In Chapter 5, we describe the experiments for acquiring and analyzing the EMG signals. These experiments deal with the problem of discriminating the EMG signals of one muscle according to the function of the muscle. In this chapter we will describe the physical set up of the signal acquisition, and the signal characterization and classification. In Chapter 6, the results of the characterization and classification are presented and we discuss the usefulness of the multifractal characterization of the EMG signals for the proposed experiment. Conclusions, recommendations and contributions are presented in Chapter 7.

CHAPTER II

BACKGROUND ON EMG AND MUSCLE CONTRACTION

The objective of this chapter is to give a brief study of muscle function. This provides a background for discussing the physiological and anatomical factors involved in the design of experiments and also the interpretation of the results of the experiments in the future chapters.

In this chapter we discuss the important factors influencing the shape of Electromyographic (EMG) signals recorded from a contracting muscle. The most important of these factors is the number of the recruited motor units and their firing rate. We explain how these factors vary in a sustained contraction. We also discuss how the placement of the electrodes in the surface recordings influence the shape of the EMG signals.

We finish this chapter by reviewing the known patterns of recruitment of the motor units in different muscle functionalities. This section provides the background for justification of the objective of the experiments presented in chapter V.

2.1 Overview

Muscles are the primary organ of the body, making 70% to 85% of the body weight [CrKa98]. The single smallest controllable muscular unit is called a motor unit. The motor unit consists of a single alpha-motoneuron, its neuromuscular junction and the muscle fibres it innervates. Alpha-motoneurons are located in the anterior horn of the spinal cord and through their relatively large diameter axon and terminal branches innervate a group of muscle fibres. The termination of the axon at the muscle fibre is

known as the endplate region or the neuromuscular junction and is usually located near the middle of muscle fibres. A muscle fibre is a very fine thread, with a length between few millimetres to 30 cm and a diameter of 10 to 100 μm [BaDe85].

There are two major sensory organs found within the muscle, the muscle spindle and the Golgi tendon organ. The muscle spindles which are stretch receptors are scattered among the muscle fibres in which they are hosted and they inform the nervous system about the instantaneous length and velocity of contraction of the muscle fibres. The spindle activity is at spinal level and is not projected to the cortex and thus not consciously perceived. The Golgi tendon organ is found in the muscle-tendon junctions and is sensitive to the tension placed on tendons and the effort given out by the muscle. The output of the Golgi tendon organ terminates at the lower centres of the brain and does not reach the cortex. Another source of information is found in joint receptors which are found in each joint and inform the nervous system about the joint angle and position.

In 1950, Hunt and Kuffer first observed that we have two sensorimotor systems, the alpha and gamma motor systems, each having their own muscles, motoneurons and principles of organization [CrKa98]. The gamma motor system primarily emerges from the lower centres of the brain while the alpha motor system originates from the cortex. The gamma motor system carries out the reflexes that have been selected and passed through generations and are fixed. The alpha motor system provides the opportunity to adapt to the surroundings.

2.2 Source of EMG Signals

When a nerve action potential travels down the axon, it reaches the neuromuscular synapse and releases acetylcholine, which causes the breakdown of the ionic barrier of the

muscle membrane and sends the signal throughout the muscle fibres via the transverse tubules which causes the muscle to contract. The movement of the ions during the depolarization generates an electromagnetic field which can be detected by electrodes. The variation of the voltage (potential) detected by the electrodes with respect to ground during the depolarization is called an action potential [Guyt71].

An impulse running through a motoneuron causes all the muscle fibres of the motor unit to contract almost simultaneously. A fixed delay is introduced between the activation time of the fibres due to the different length and diameter of the individual axon branches innervating them. The action potential from the muscle fibres of a motor unit separated spatially and temporally summate to form a motor unit action potential. The extracellular recording of the depolarization and repolarization running through the muscle fibres provide the basis for electromyography (EMG). With surface electrodes a population of motor units are actually recorded rather than a single motor unit, since the motor units tend to overlap their fibre territories spatially [BaDe85].

The amplitude of detected action potentials is dependent on the diameter of the muscle fibre, the distance between the active muscle fibre and the detection site, and the filtering properties of the electrode. The duration of the action potentials is inversely related to the conduction velocity of the muscle fibre and the nerve branch [BaDe85]. The time delay of the action potentials of different muscle fibres detected by an electrode is also a function of the differences in distances of the muscle fibre with respect to the electrode site. The shape and amplitude of the motor unit action potential is dependent on the geometric arrangement of the active muscle fibres with respect to the detection point. Since the muscle fibres of different motor units are scattered in a semi-random fashion

throughout the muscle, the information recorded by a surface electrode does not relate to a specific motor unit.

The time domain and frequency domain characteristics of the EMG signal can be used as a means for studying the muscle contractions. Several parameters of the EMG signal such as the root mean square (RMS) of the amplitude, median power frequency, mean power frequency, peak frequency are the ones often used for studying the behaviour of the EMG signal

2.3 Muscle Contraction

Each muscle contains muscle fibres. The individual fibres are broken down to myofibrils. Each myofibril consists of aggregates of myosin and actin filaments. The actin filament is a thin fiber with two negatively charged molecules that spiral around each other. The myosin filament, which is thicker and also negatively charged, is made up of molecules with globular heads. In the resting state the actin and myosin filaments lie next to each other, repelled by their negative charge. In 1950, Huxley proposed a model describing the act of contraction. The nerve action potential causes a release of acetylcholine at the neuromuscular junction. This sends a charge through the transverse tubules which causes a release of calcium into the space where the myosin and actin fibres are located. The calcium, having a strong positive charge, bonds with one of the proteins making up the actin filament. This causes a change in configuration of the actin filament which allows binding of myosin with actin. The movement of the myosin crossbridges that link actin and myosin, provide the force that pushes the thin actin filaments along the thick myosin filament. Each myosin head has two binding sites on it: one for an ATP molecule and one that binds to actin. Myosin is a motor protein that converts the chemical

bond energy of ATP into the mechanical energy of motion. The energy released by ATP changes the angle between the head of the myosin molecule and the long axis of the myosin filament. This rotation of the myosin head on its flexible neck creates the power stroke that is the basis for muscle contraction. During the power stroke, the movement of the myosin head, pushes the actin filaments to slide along the myosin filament. At the end of a power stroke, the myosin releases the actin, swings back and binds to a new actin molecule, ready to start another contractile cycle. This process repeats many times as a muscle fibre contracts [SiOG98].

There is an element of randomness in this phenomenon due to the random discharge of acetylcholine packets at the neuromuscular junction which ultimately controls the release of calcium within the muscle cell [BaDe85].

To sustain a contraction the motor unit must be repeatedly activated. Successive muscle twitches overlap in time, meaning that the first muscle twitch is not completely over by the time the second one begins, therefore since the muscle is already in a partially contracted state when the second twitch begins, the degree of muscle shortening is slightly greater than before. Consequently the summation of successive contractions become greater and greater until an optimum frequency is reached [Guyt71].

Furthermore the overlap of adjacent motor units also allows the separate motor units to contract in support of each other rather than act individually. The force of contraction increases progressively as the number of contracting motor units increases.

2.4 Muscle Functionality

Generally, it has been agreed that muscles controlling fine movements have the smallest number of muscle fibres per motor unit while large coarse-acting muscles have a

larger number of muscle fibres served by one axon [Guyt71]. This innervation ratio is not fixed for all the motor units in a single muscle. Within a muscle there are smaller motor units which are excited earlier during a contraction, than larger motor units which are activated at higher force levels [Mcco96]. The longer the muscle the more and the faster it can shorten and the thicker the muscle the more force it can develop.

The muscle fibres can be divided into the following three broad categories.

1) Type I: Slow-twitch fibres take more than 35 milliseconds to complete a depolarization/repolarization cycle. They are dark red in appearance. These fibres twitch less than 25 times per second, and are fatigue resistant.

2) Type II a: Fast-twitch, fatigue resistant fibres which are reddish and have a slow rate of fatigue due to their aerobic capacity. They are classified as Type II a fast-twitch fibres.

3) Type II b: Fast-twitch, fatiguable fibres take less than 35 milliseconds to twitch and are whitish in appearance. These fibres are not resistant to fatigue and have a high anaerobic capacity. These are categorized as Type II b fast-twitch fibres.

Small slow nerve fibres activate a slow-twitch muscle while large fast nerve fibres activate fast-twitch muscles. Most muscles contain a mixture of fast and slow twitch fibres [CrKa98].

One muscle can do work in different ways. One way of classifying the muscle activity is according to the changes of the length of the muscle. An *isometric* contraction is one during which the length of the contracting muscle remains constant. *Anisometric* is one during which the length of the contracting muscle may vary [BaDe85].

Another classification of the muscle activity is according to the contribution of the

muscle in a certain movement. *Agonist* muscles are the prime movers or the ones which initiate the contraction, *synergist* or helper muscles are ones which their activity provides an additive contribution. *Antagonist* muscle is one which actively provides a negative contribution to a particular contraction [CrKa98].

2.5 Patterns of Recruitment

Force can be generated by increasing the number of new motor units or by increasing the firing rate of the motor units. It is a common belief that at the beginning of a contraction, recruitment of new motor units is a dominant factor with the small motor units being recruited first while the increase of firing rate plays a secondary role. However, for force levels ranging from 30% to 75% of maximum voluntary contraction, the dominant factor is an increase in firing rate. The firing rate of motor units is also muscle dependent. In general the smaller the muscle the higher the firing rate [BaDe85].

During a constant force contraction, motor unit rotation takes place, that is the newly recruited motor units replace previously active ones [BaDe85]. If the contraction of a muscle is sustained with enough force for a long time, the conduction velocities of the action potentials along the muscle fibres begin to slow down and the muscles begin to twitch less frequently, which results a reduction of the median frequency of the muscle energy. The decrease in the firing rate of the motor units is more evident in fast-twitch fibres than in slow-twitch fibres [BaDe85].

The order of recruitment of the motor units during a contraction is reported to be a function of motoneuron size, size of motor units, fibre type, size of muscle and also the functional role of the muscles. Motor units with smaller axons are recruited first [FDWK73]. In a steady contraction, smaller motor units are recruited before the large

ones [Mcco96]. The Type I fibres are recruited first followed by Type II fibres. In sudden movements Type II fibres are recruited first [Mcco96]. Small muscles recruit all their motor units below 50% maximum voluntary contraction and larger muscles recruit motor units throughout the full range of voluntary force [BaDe85]. The order of motor unit recruitment is also a function of the functional role of the muscle. McComas cited Gilen and Denier Van Der Gon to state that "in the biceps the threshold of a motor unit depends on whether the muscle is being used to flex the elbow, supinate the forearm, or externally rotate humerus" [GiDe90][Mcco96].

The nervous system in fact controls pools of motoneurons rather than individual motoneurons, this is known as common drive. Further explanation of this process can be found in [BaDe85].

2.6 Summary

In this chapter, we gave an overview of the mechanism of muscle contraction and the important factors involved and we discussed the sources of the EMG signals. The time domain and frequency domain characteristics of the EMG signal are often used as a mean for studying the muscle contractions. Since we want to investigate the possibility of using the multifractal dimensions of the EMG signal as analysis criteria in this thesis the next chapter will provide a background on fractals, chaos and strange attractors.

CHAPTER III
BACKGROUND ON FRACTAL DIMENSIONS, CHAOS AND STRANGE ATTRACTORS

The objective of this chapter is to provide the reader with an introduction to fractal geometry and chaotic dynamics. Fractal geometry, which was popularized by Mandelbrot in 1960, provides us with a tool for describing objects which are difficult to describe by Euclidean geometry, such as trees, rivers, coastlines, and lightning [Kins94]. Chaotic dynamics are used for the study of the behaviour of nonlinear dynamic systems such as growth and decay of populations, oscillatory output of a nonlinear electrical circuit, and thermal convection . Under certain conditions, these deterministic systems can manifest an unpredictable and complex behaviour which can be confused with randomness. The theory of chaos provides a tool for differentiating between noise and the chaotic behaviour of deterministic systems.

In this chapter, we first give an introduction to fractal sets and their properties and discuss the basic concepts of Euclidean, topological, and morphological dimensions. The second section deals with chaotic strange attractors and how these systems are related with the concept of fractality and fractal dimensions. This discussion is followed by the presentation of several nonlinear dynamic systems with chaotic behaviour. In the last section, multifractals and the generalized Rényi dimensions are introduced.

3.1 Morphological Dimensions and Fractals

3.1.1 Euclidean and Topological Dimensions

The Euclidean dimension, D_E, is simply the number of coordinates required to

specify an object spatially.

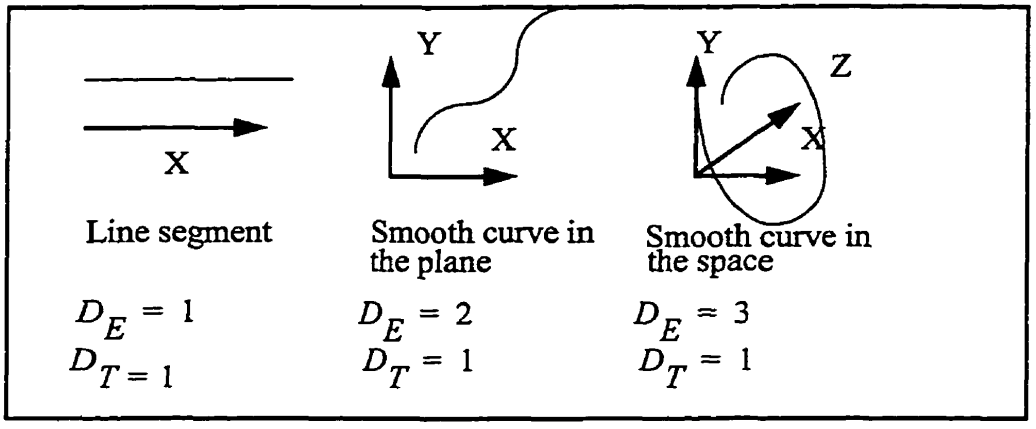

Fig. 3.1. The topological dimension of an object does not change under homeomorphic transformations.

The topological dimension on the other hand has its roots in a branch of mathematics known as topology which deals with those features of objects that are more qualitative and which do not change under proper transformations (homeomorphisms). Homeomorphisms are functions which are one to one, onto, continuous and also have a continuous inverse function. A hole in an object remains a hole regardless of proper transformations such as stretching or twisting. The topological dimension derives from the ability to cover the object with discs of small radius. A line segment may be covered using many discs intersecting many times with each other. However, it is possible to refine the covering using discs with only a single intersection between adjacent pairs of discs. When the line is transformed by a homeomorphism, one can still find discs sufficiently small to cover it with just having intersections at adjacent pairs of discs. If we try to cover a two dimensional surface with spheres of small radius, we cannot have a complete covering with only intersecting the pairs of adjacent spheres. A complete covering

requires groups of three spheres intersecting with one another. The covering of an object by elements of small radius requires intersections between a minimum of $D_T + 1$ groups of elements, where D_T is the topological dimension of the object. The *topological dimension*, D_T, of an object does not change under proper transformations [Addi97].

3.1.2 Strictly Self-Similar Objects and the Self-Similarity Dimension

A strictly self-similar object is an object which is constructed from exactly self-similar segments, under various degrees of magnification. That is to say each small part replicates the whole structure exactly.

The Cantor set [Cant83] is one of the most frequently quoted self-similar objects along with the Koch curve [Koch04] and the Mandelbrot set [Mand80]. The Cantor set consists of an infinite set of points on a unit interval, but it is not a continuous one dimensional line. Maybe the best way to describe a Cantor set is to explain the way it is constructed. One can generate the Cantor set through an iterative process starting from an initiator. The initiator of a Cantor set is a straight line. The generator is an algorithm describing the transformation from the initiator to the largest scale object. In the case of the Cantor set, the initiator is transformed to three line segments with equal lengths and then the middle segment is eliminated as shown in step 1 of Fig. 3.2. The second step is to begin from the results of the first step, and apply the generator to each of the remaining segments of step 1 [Kins97]. If this process is iterated infintely, what is left is a collection of infinitely small line segments whose individual and combined lengths approach zero. This set of "points", or infinite small line segments, is called the Cantor set or Cantor dust. The process of constructing a Cantor set is illustrated in Fig. 3.2 for the first three steps.

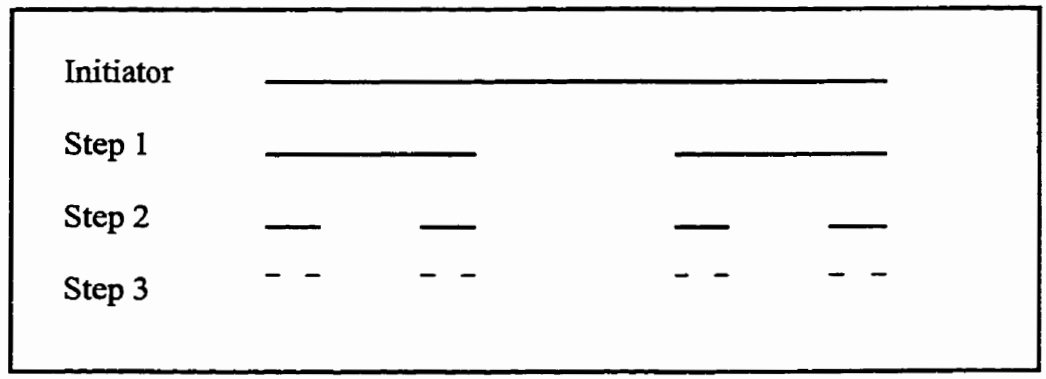

Fig. 3.2. Construction of Cantor set, the first three steps.

Variations of the Cantor set can be constructed by changing the remaining pieces in the process or choosing different lengths for the remaining pieces, but still the same object with a complex structure is produced. If we zoom in any section of the Cantor set we find a structure which resembles the whole object.

The Euclidean dimension of the Cantor set is obviously one as only one coordinate direction is required to specify all the points in the set. It can also be seen that it is possible to find single, non-intersecting discs of smaller and smaller radius to cover all the sub-elements thus the topological dimension is zero. The self-similar structure of the Cantor set and other self-similar objects motivated the introduction of the self-similarity dimension. The concept of self-similarity dimension is associated closely with the scaling properties of the object.

Consider a line, surface and a cube of length L, area A, and volume V, all equal to unity. If we divide the line to N smaller self-similar segments, each of length δ then

$$L = N\delta = 1 \tag{3.1}$$

If we divide the surface to N self-similar segments each with an area of δ^2 then

$$A = N\delta^2 = 1 \tag{3.2}$$

And finally applying the same logic to the unit volume we have

$$V = N\delta^3 = 1 \tag{3.3}$$

The exponent of δ at each case is a measure of the dimension of the object. In general, if the object is made of N self-similar, non-intersecting segments where each can be covered exactly by a hypercube of side δ, then the self-similarity dimension, D_S, is defined as

$$N\delta^{D_S} = 1 \tag{3.4}$$

where the hypercube has the same Euclidean dimension as the object [Mand83]. These hypercubes are also referred to as vels (volume elements) as proposed by Kinsner [Kins97]. N and δ are said to have a power law relationship. Taking logarithms of both sides gives

$$D_S = \frac{\log(N)}{\log(1/\delta)} \tag{3.5}$$

Applying this formula to the Cantor set constructed before, and observing that the left-hand third of the set contains an identical copy of the set, and so does the right-hand side third, for $\delta = 1/3$ the fractal contains $N = 2$ self-similar segments. So according to the equation above

$$D_S = \frac{\log(2)}{\log(1/(1/3))} = \frac{\log(2)}{\log(3)} = 0.6309 \tag{3.6}$$

The same D_S results for self-similar segments of size $\delta = 1/9$ or $\delta = 1/27$ or any $\delta = 1/3^n$ with positive nonzero integer n.

3.1.3 Randomly Self-Similar Objects

The Cantor set is an example of a strictly self-similar fractal, that is the smaller segments of the object contain exact copies of the whole structure, but there is another group of fractals known as statistically self-similar fractals or random fractals. This means the smaller segments have the same statistical properties of the bigger structure [Mand83].

An element of randomness can be introduced to the structure of Cantor set. For example if in each step, instead of always deleting a fixed portion of the line segments, we eliminate a section which is randomly chosen among the three possibilities, we will obtain a Cantor set which is quite irregular in comparison to the one constructed before but it has the same rich structure. An example of the random construction of a Cantor set is illustrated in Fig. 3.3.

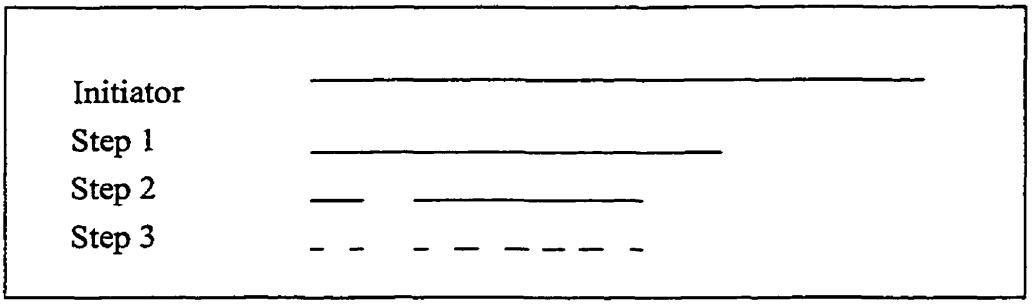

Fig. 3.3. The first three possible steps in random construction of a Cantor set.

The self-similarity dimension is not useful in the identification of random fractals since it depends on identifying the exactly similar segments of different scales. The concepts of Hausdorff and box-counting dimensions are used to classify random fractals.

3.1.4 Box-Counting Dimension

To examine an object for its box-counting dimension, the object is covered with hypercubes or "elements" of side length δ. The Euclidean dimension of the elements can be larger than or equal to the Euclidean dimension of the fractal object. If N is the minimum number of elements which are required for a complete covering, then the *box-counting dimension* is defined as

$$D_B = \frac{\log(N) - \log(V)}{\log(1/\delta)} \tag{3.7}$$

where V is the hypervolume of the elements with side length δ [Kins97]. We can rearrange the equation to the form

$$\log(N) = D_B \log(1/\delta) + \log(V) \tag{3.8}$$

This can be regarded as an equation for a line with $\log(1/\delta)$ as x-variable and $\log(N)$ as y-variable, then the gradient of the line, D_B, is the box-counting dimension.

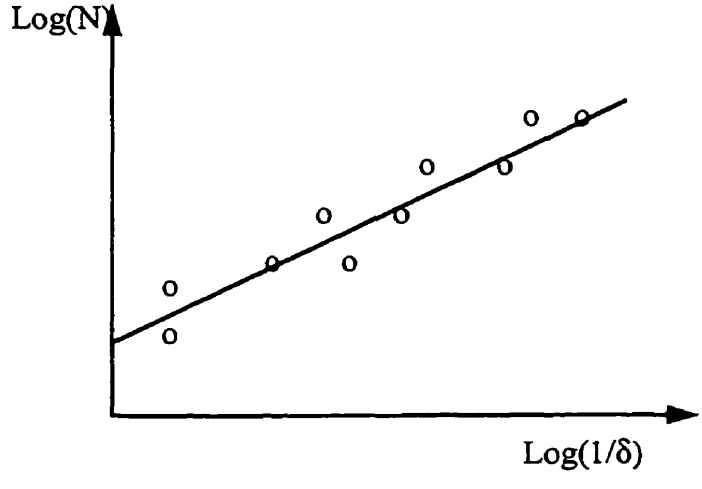

Fig. 3.3. Estimation of box-counting dimension of experimental data. Gradient of the line is the box-counting dimension.

Having several pairs of the x-y coordinates of this line, D_B can be estimated by a linear regression of these points.

3.1.5 Hausdorff Dimension

The calculation of the Hausdorff dimension of an object also deals with the complete covering of the object, but this time the dimension of the object is estimated by finding the proper dimension of the hypercubes which give an exact measurement of the object.

If we try to measure the length of a curved line by covering the curve with elements of side length δ and counting the number of elements needed for a complete covering, we get an approximation of

$$L_m = N\delta^1 \tag{3.9}$$

where N is the number of the elements and L_m tends to the true length L only when δ tends to zero. The important observation is that this result is valid only when the Euclidean dimension of the measuring element and the object are the same. Now generalizing this concept, if N hypercubes of side length δ are required to cover the object, the approximate hypervolume of the object is given as

$$V_m = N\delta^{D_H} \tag{3.10}$$

For a specific choice of D_H, when δ tends to zero, the measured hypervolume of the object tends to the actual value. If the chosen exponent is larger than that specific choice then the measured hypervolume tends to infinity and if the exponent is smaller than that the measured hypervolume tends to zero. The *Hausdorff dimension* of the object is

that critical exponent where the equation transits from zero limit to infinity limit. Non-integer exponents are allowed [Mand83].

The formal definition of a fractal was given by Mandelbrot as "a set for which the Hausdorff dimension strictly exceeds the topological dimension." [Mand83]. These objects are called fractals because of their non-integer fractional dimensions.

Since all dimensions mentioned in this chapter deal with the morphology of the objects, they are all classified as morphological dimensions. Other classes of dimensions are presented later in this chapter.

3.2 Chaos in Nonlinear Dynamic Systems

The majority of natural phenomena can only be modelled as nonlinear systems. Since nonlinear systems are very difficult to analyze mathematically, linear systems are usually preferred for modelling purposes. But only nonlinear systems are capable of exhibiting a chaotic behaviour which presents a more accurate model of the natural phenomena. Mathematical research in chaos can be traced to 1890, when Hénri Poincaré studied the stability of the solar system. He made the first discovery of chaos in the orbital motion of three celestial bodies which exerted gravitational forces upon each other [PeJS92]. Edward N. Lorenz encountered chaos in the numerical studies of the set of differential equations he used for testing weather prediction [Lore63]. David Ruelle and Floris Takens suggested in 1970 that turbulent flow might be an example of chaos [RuTa71].

In the following sections we first give the formal topological definitions of chaos and attractors and then proceed to make the connection between these topological defini-

tions and the solutions of nonlinear dynamical systems.

3.2.1 Chaos and Attractors in Topology

In this section, we give a formal definition of a chaotic behaviour of a transformation $f:J \to J$. We also discuss the topological properties required by a bounded subset of J to be a strange attractor of a chaotic transformation f.

In order to present the definitions of chaos and attractors clearly, we need to give several background definitions. The objective of this section is to make a clear and unified definition of concepts such as sensitivity to initial conditions and denseness of sets used in this thesis. $f:J \to J$ is a function in all the definitions.

Definition 1 : $f : J \to J$ is said to be topologically transitive if for any pair of open sets $U, V \subset J$ there exists $k > 0$ such that $f^k(U) \cap V \neq 0$, where $f^k(U)$ means the kth iteration of subset U under the transformation f.

Definition 2 : $f : J \to J$ has sensitive dependence on initial conditions if there exists $\varepsilon > 0$ such that, for any $x \in J$ and any neighborhood M of x, there exists $y \in M$ and $n \geq 0$ such that $|f^n(x) - f^n(y)| > \varepsilon$

Definition 3 : Let $S \subset R$ where S and R are arbitrary equations. A point $x \in R$ is a limit point of S if there is a sequence of points $x_n \in S$ converging to x. S is a closed set if it contains all of its limit points.

Definition 4 : The forward orbit of x is the set of points $x, f(x), f^2(x), \ldots$. If f is a homeomorphism, we define the full orbit of x, as $f^n(x)$, for natural n. If $f(x) = x$, x is a fixed point of f. The point x is a periodic point of period n_p if $f^{n_p}(x) = x$.

Definition 5 : A subset S of R is dense in R if closure of S (S and its limit points) equals to R.

Definition 6 : Let J be a set, $f: J \to J$ is said to be chaotic on J if

1. f has sensitive dependence on initial condition;

2. f is topologically transitive; and

3. Periodic points are dense in J.

A chaotic map has three ingredients: unpredictability, indecomposibility, and an element of regularity. A chaotic system is unpredictable because of the sensitive dependence on initial conditions. It cannot be broken down or decomposed into two subsystems which do not interact because of its topological transitivity. The element of regularity stems from the fact that the periodic points are dense. [Deva89].

Definition 7 : Let $f: J \to J$ be a given transformation. A bounded subset A of J is a chaotic and strange attractor for the tranformation f if there exists a set R with the following properties.

1. **Attractor.** R is a neighborhood of A, i.e., for each point x in A there is a small disk centred at x which is contained in R. This implies in particular that A is in R. R is a trapping region, i.e., each orbit started in R remains in R for all iterations. Moreover, the orbit becomes close to A and stays as close to it as we desire. Thus, A is an attractor.

2. **Sensitivity.** Orbits started in R exhibit sensitive dependence on initial conditions. This makes A a chaotic attractor.

3. **Fractal.** The attractor has a fractal structure and is therefore called a strange attractor.

4. **Mixing.** A cannot be split into two different attractors. There are initial points in R with orbits that get arbitrarily close to any point of the attractor A [PeJS92].

Furthur formal topological discussion on this subject can be found in [Deva89]. It should be noted that a final definition of an attractor is still not completely established since the four properties above have been proven to be dependent, for example mixing and sensitivity are interrelated.

3.2.2 Chaotic Dynamical Systems and their Attractors

To begin with, take a system of N first order ordinary differential equations

$$\frac{dx_1}{dt} = F_1\left(x_1, x_2, \ldots, x_N\right) \tag{3.11.a}$$

$$\frac{dx_2}{dt} = F_2\left(x_1, x_2, \ldots, x_N\right) \tag{3.11.b}$$

$$\vdots$$

$$\frac{dx_N}{dt} = F_3\left(x_1, x_2, \ldots, x_N\right) \tag{3.11.c}$$

This is an example of a dynamical system, because the system evolves in time. Time is a continuous variable in this system. Considering numerical methods such as Runge-Kutta for numerical solutions to this kind of systems, for any initial state of the system, the equations can be solved in principle to obtain the future states. The path followed by the system as it evolves with time is called an *orbit* or a *trajectory.* Plotting the evolution of two or more independent variables of the system versus each other will give the *phase spaces* or the *state spaces* of the system in finite time intervals. Now we

can ask this question: if we know in complete detail the past history of the process, can we predict what will happen to it in future? Is it possible to deduce the longterm or the asymptotic behaviour of the system? The concept of chaos arises with an attempt to answer this question and it is closely related to the definition of "complete detail" and precision.

The behaviour of a nonlinear dynamical system can fall into three classes: stable, unstable, and chaotic [JoSm87]. Stable behaviour means that after some transient period such systems settle in a periodic or a steady state motion. Unstable behaviour means that the trajectories are aperiodic and unbounded. But the dissipative systems of differential equations in two dimensions or more can have bounded trajectories whose behaviour does not converge to an equilibrium point nor to a periodic or quasiperiodic orbit. They can be attracted by an object of complicated structure which attracts the neighbour points but has some inherent instability along it. These attracting sets or *strange attractors* are not simple geometrical objects and cannot be well characterized as integer dimensional objects. Actually the strange attractors are fractals. One system of nonlinear differential equations can exhibit stable, unstable, or chaotic behaviour depending on the range of the parameters involved in the definition of the equation and the value of the initial conditions.

It is important to note that although the trajectories of chaotic dynamical systems are neither periodic nor quasi-periodic, and the Fourier transform of them yields a broad-band spectrum, these systems are still deterministic and not stochastic because their behaviour is governed by a set of equations [Addi97]. However, longterm prediction of the behaviour of chaotic dynamical systems is impossible because they are extremely

sensitive to the initial conditions. Exact initial conditions will always create the same trajectories but the numerical tools used for the calculations do not possess infinite resolution, therefore, any error in specifying the initial conditions or during the iterative calculation of the trajectories can give a result which is not be accurate for prediction purposes [PeJs92].

The study of trajectories of differential equations can be made simple by taking the intersection of the trajectories with a given hyperspace. Consider the autonomous system

$$\frac{dy}{dt} = X(x, y) \tag{3.12.a}$$

$$\frac{dy}{dt} = Y(x, y) \tag{3.12.b}$$

and its phase diagram in the x, y plane. Let Z be a curve or a cross section of the plane with the property that it cuts each phase space path transversely, that is, it is nowhere tangential to a phase path. Consider a point $A_0\,(x_0, y_0)$ on the cross section Z. If we follow the phase space path through A_0 in its direction of flow then it next cuts Z at $A_1\,(x_1, y_1)$. This point is the first return or *Poincaré map* of the point A_0. If such a point exists we called it the first return. We can continue in the same fashion obtaining the rest of the points of the mapping. This reduction of a continuous time system of dimension n to a discrete time system of dimension $n-1$ is called the Poincaré section technique [JoSm87]. We shall now continue with the examples of some well known attractors to investigate further the properties of these fractal objects.

3.2.3 The Hénon Attractor

The Hénon attractor is an example of an attractor of a discrete dynamical system.

This system evolves in time with discrete steps in contrast to a continuous time system. Both chaotic and periodic solutions can be found for Hénon set of equations depending on the value of parameters a and b. The equations are defined as

$$x_{n+1} = 1 - ax_n^2 + y_n \tag{3.13.a}$$

$$y_{n+1} = bx_n \tag{3.13.b}$$

The trajectories of both variables have been plotted in Figs. 3.4 and 3.5 for two sets of parameters. The first set which is $a = 0.9, b = 0.3$ leads to a periodic post transient behaviour. The second set of parameters, $a = 1.4, b = 0.3$, produces a chaotic behaviour, so the trajectory is aperiodic with a broad-band spectrum. The initial values are $x(0) = y(0) = 0.8$ for both experiments.

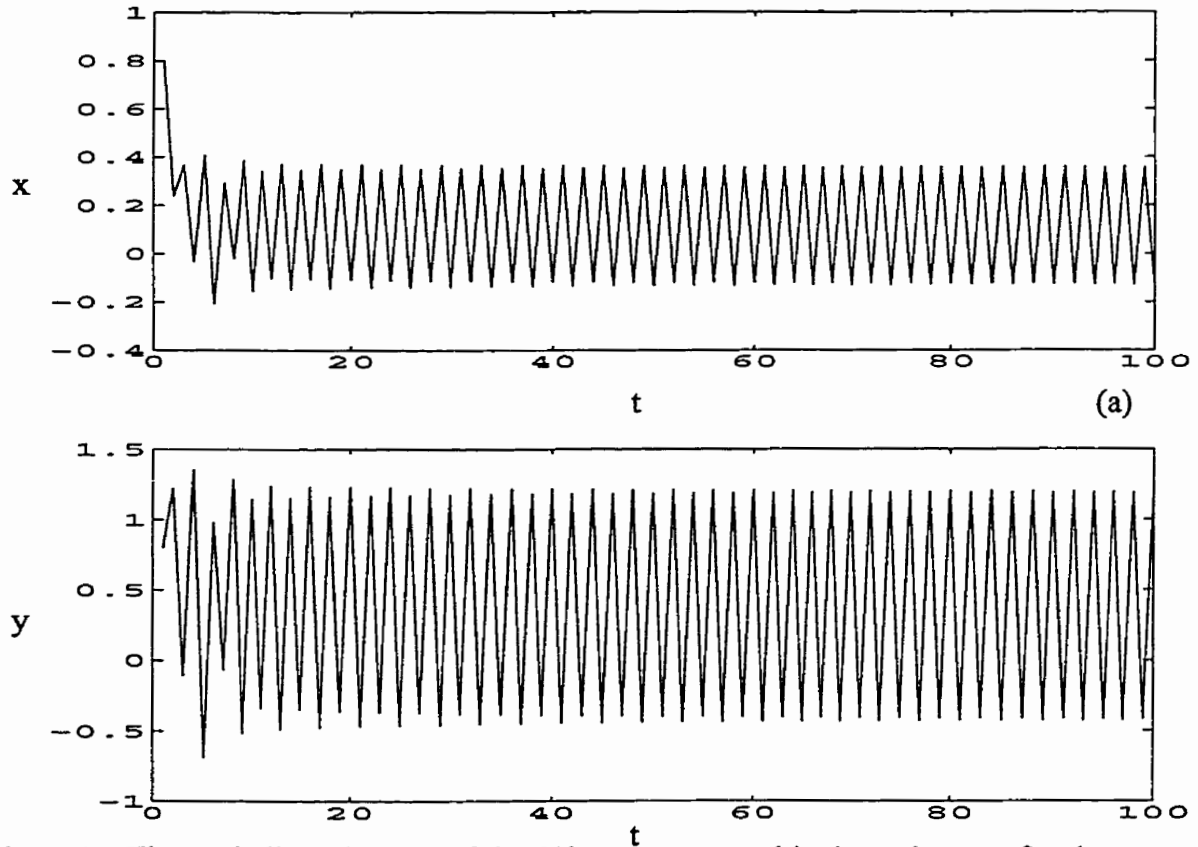

Fig. 3.4. The periodic trajectory of the Hénon attractor (a) The trajectory for the x-variable (b) The trajectory for the y-variable.

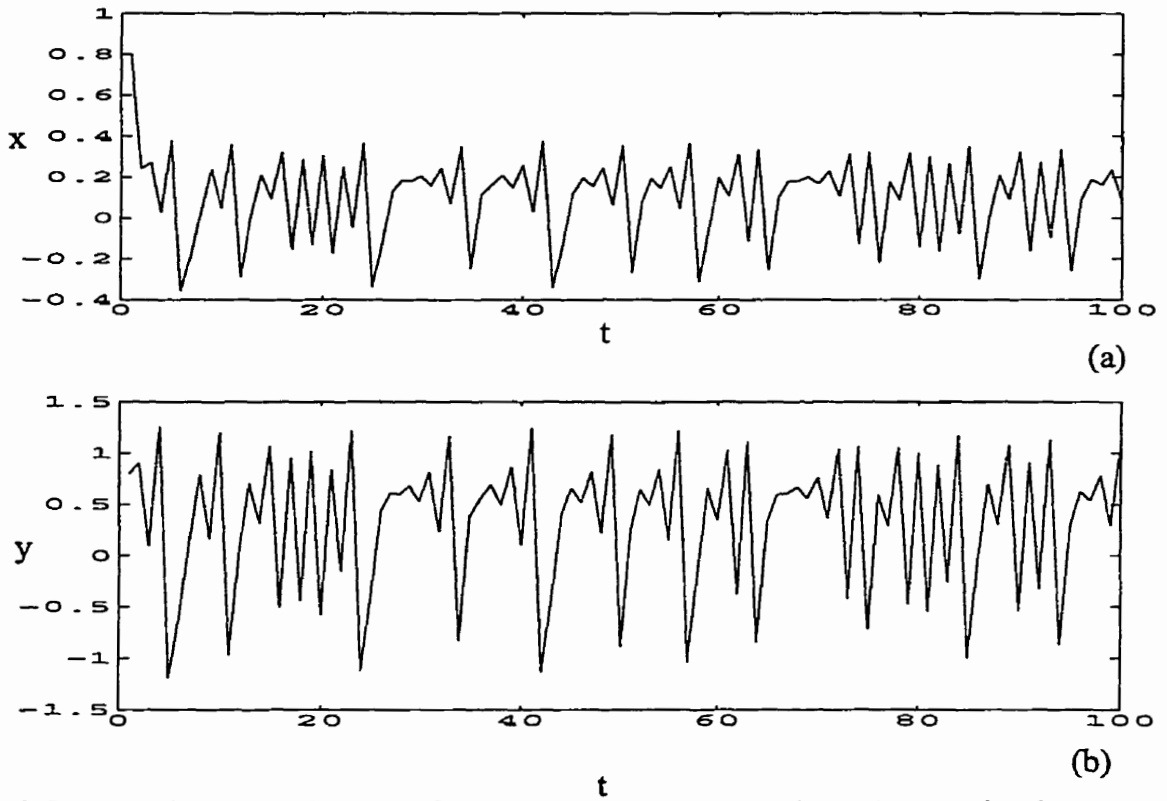

Fig. 3.5. The chaotic trajectory of the Hénon attractor (a) The trajectory for the x-variable. (b) The trajectory for the y-variable.

The phase space of the chaotic trajectory is plotted in Fig. 3.7. The periodic phase space shows that the initial values of the variables converge to two periodic points and oscillate between them. But the phase space of the chaotic solution reveals a completely different structure. In Fig. 3.7 we can see that the outline of the structure called the Hénon attractor. We can see that the converged trajectory lies in the boundaries of the attractor structure. The boundaries of the attractor structure contain the boundaries of the chaotic solutions. Any attractor has a basin of convergence for which all the initial values falling into this basin converge to the attractor. An initial value has a distinct trajectory on the attractor which never crosses itself since the trajectories are not periodic. A small

difference in initial values can lead to a completely different trajectory. The Hénon attractor is a fractal object.

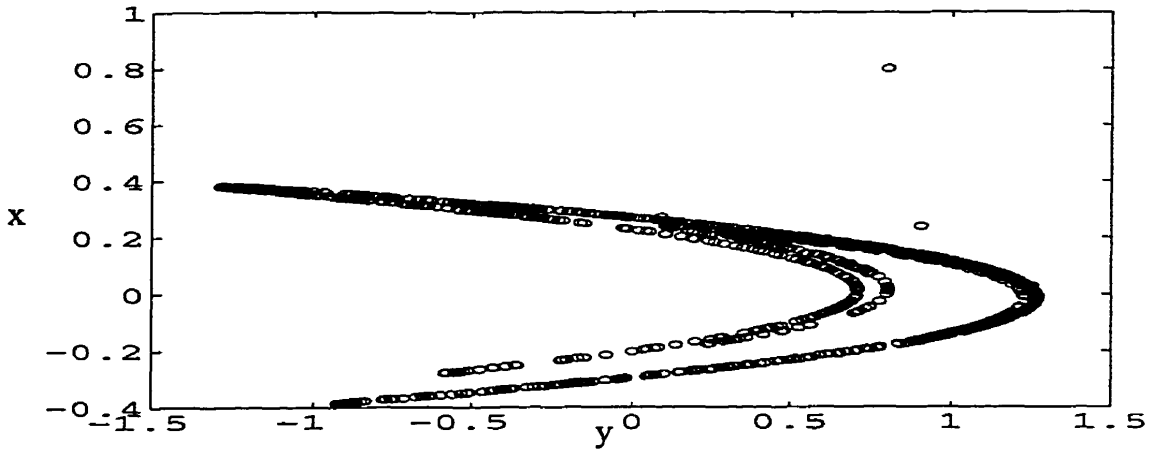

Fig. 3.6. The phase space of the chaotic solution of the Hénon attrcator for a=1.4, b=0.3.

To show more clearly what we mean by an attracting region we perform the following experiment. If we take a 100x100 matrix in the region $-1.0 \le x \le 1.0$ and $-0.1 < y \le 0.1$ and iterate every point several times through the Hénon equations we will see that the transformed plane will converge to the Hénon attractor [Héno76]. So, we can speak about a trapping region R from which no orbit can escape and any orbit will converge to some limit set. The Hénon trapping region calculated by Hénon is a quadrilateral with vertices (-1.33, 0.42) (1.32, 0.133) (1.245, -0.14) (-1.06, -0.5) [Héno76]. Having the trapping region R for the attractor we can define the attractor as the set

$$A = \bigcap_{k=0}^{\infty} H^k(R) \tag{3.14}$$

where H^k is the kth iteration of R through the Hénon transformation H. To obtain a picture of the attractor, it is sufficient to compute just a single orbit of an initial point picked at random somewhere in the trapping region. Selecting a different random initial point gives the same visual result. However, although two different orbits generate the same limit set, typically there is no correlation between them, even if they are very close. This is not a general rule because the second initial point might be a point on the trajectory of the first one. If we repeat the iterations for the region used in Fig. 3.8 we can see that as we approach infinity more and more curves will appear in the parabola shape. In fact, for $k = \infty$ the Hénon attractor consists of infinite number of parabola layers. A cross section of the Hénon attractor is a type of Cantor set [PeJS92].

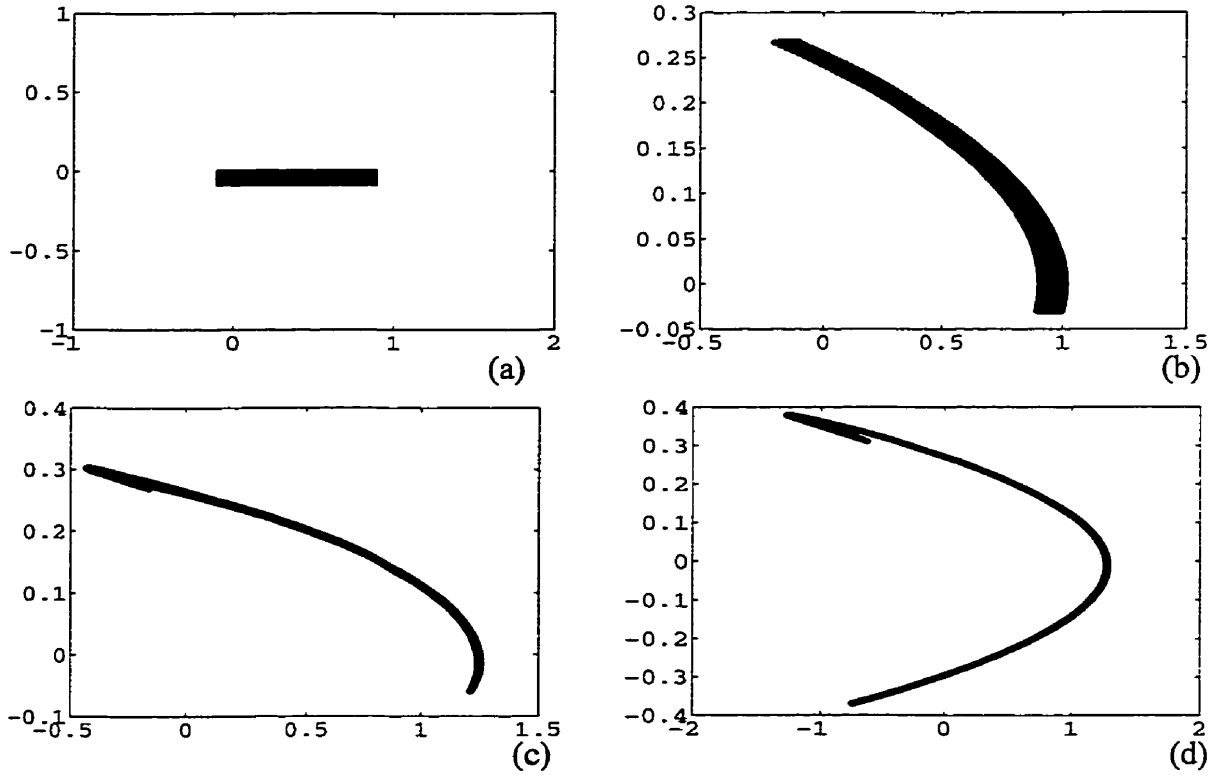

Fig. 3.7. The iteration of the points between $-1.0 \le x \le 1.0$ and $-0.1 < y \le 0.1$ with the Hénon equations: (a) The original matrix, (b) after the first iteration, (c) after the second iteration, and (d) after the third iteration.

3.2.4 The Lorenz Attractor

Lorenz equations are given as

$$\frac{dx}{dt} = -\sigma\,(x(t) - y(t)) \tag{3.15.a}$$

$$\frac{dy}{dt} = -x(t)\,z(t) + rx(t) - y(t) \tag{3.15.b}$$

$$\frac{dz}{dt} = -x(t)\,y(t) - \eta z(t) \tag{3.15.c}$$

The value of the parameter r is the critical value which determines the stability of the solutions. The critical range of r is between 27.74 and 100.5 between which the equation shows a chaotic behaviour. Figures 3.9 and 3.10 show three-dimensional phase spaces of a chaotic and a periodic solution of the equations and outlines the bounds of the Lorenz attractor. The parameters are $\sigma = 10$, $\eta = 2.67$ and $r = 16$ for the periodic solution and $r = 28$ for the chaotic solution. The initial values are $x(0) = y(0) = 12$ and $z(0)) = 34$.

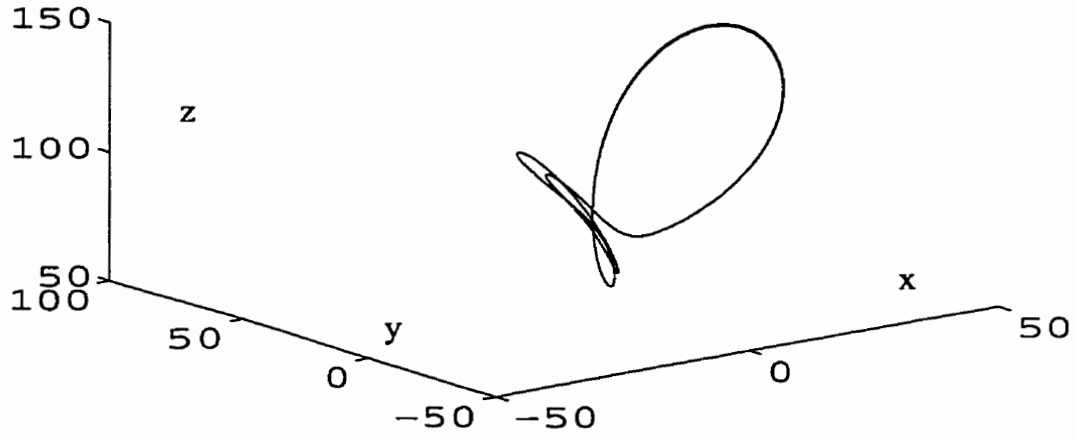

Fig. 3.8. The phase space of a periodic solution to the Lorenz equations.

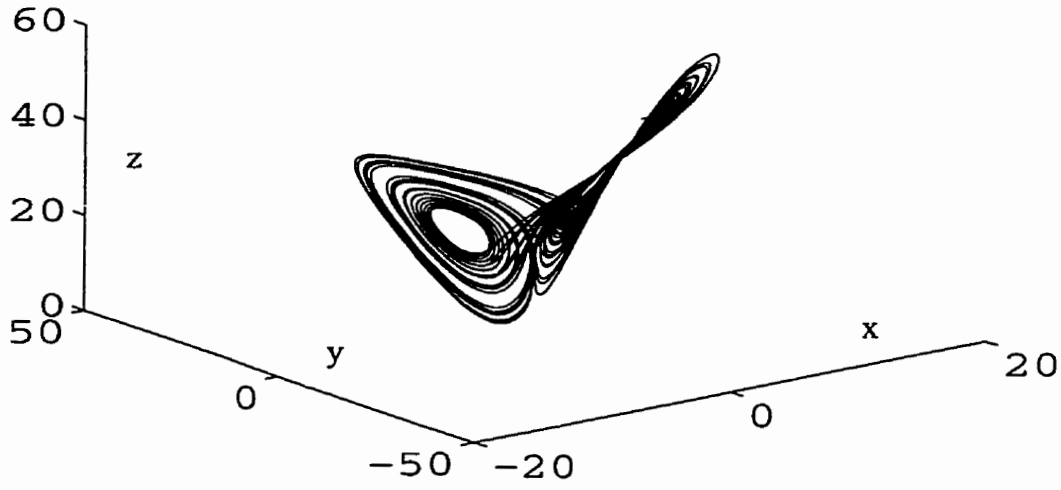

Fig. 3.9. The phase space of a chaotic solution to the Lorenz equations.

3.2.5 The Rössler Attractor

The Rössler attractor is given by the set of equations

$$\frac{dx}{dt} = -(y(t) - z(t)) \tag{3.16.a}$$

$$\frac{dy}{dt} = x(t) + \lambda y(t) \tag{3.16.b}$$

$$\frac{dz}{dt} = \beta + x(t)z(t) + \Upsilon z(t) \tag{3.16.c}$$

This system has only one nonlinear term. Setting the parameters to $\lambda = 0.2$ and $\beta = 0.2$ and varying the third parameter Υ, we can find a period doubling sequence to chaos.

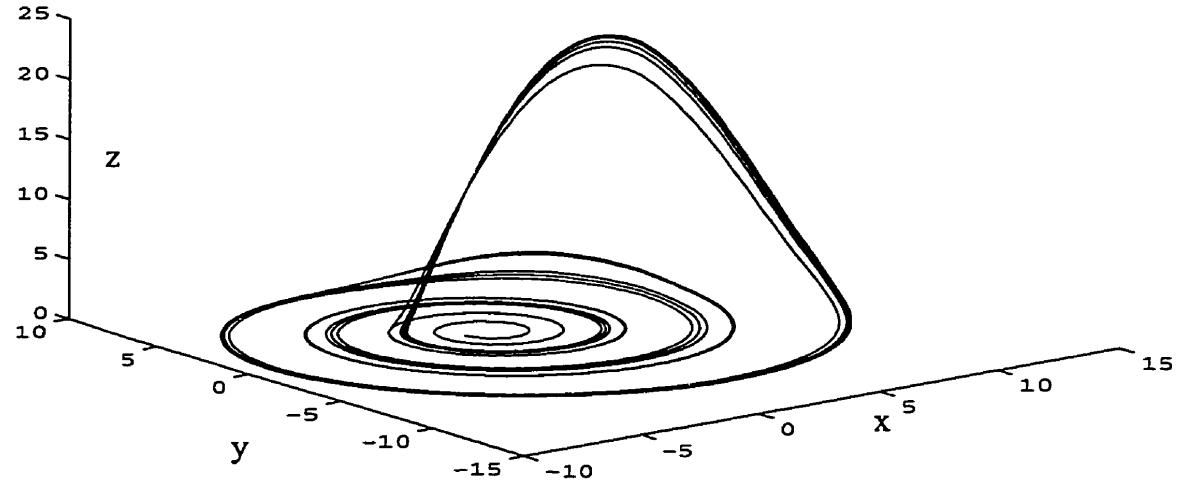

Fig. 3.10. The 3-dimensional solution of the Rössler equations for λ=0.2, β=0.2, Υ=5.7 the initial conditions are $x(0)$ =-1, $y(0)$ =0, $z(0)$ =0.

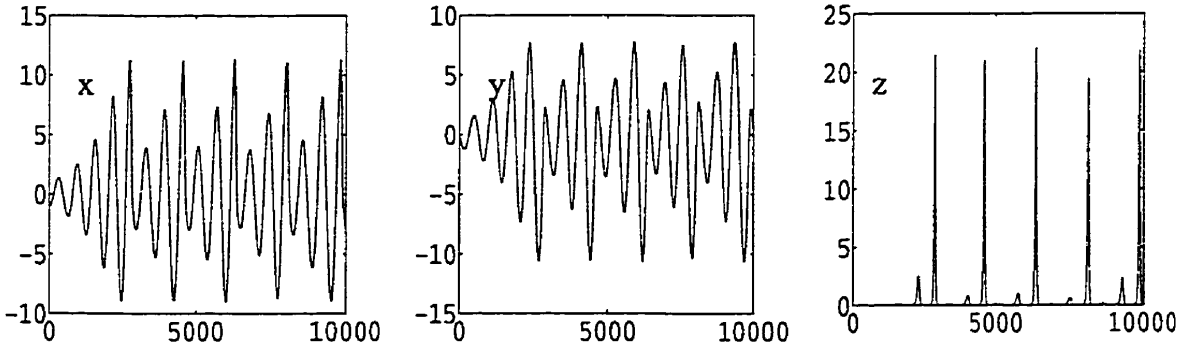

Fig. 3.11. The single dimensional trajectory of the chaotic solution of the Rössler equations for λ=0.2, β=0.2, Υ=5.7 with initial conditions are $x(0)$ =-1, $y(0)$ =0, $z(0)$ =0. The equations have been solved using the numerical method of fourth order Runge-Kutta and iterated 25000 times.

Four phase space portraits are shown for different values of Υ in Fig. 3.13.

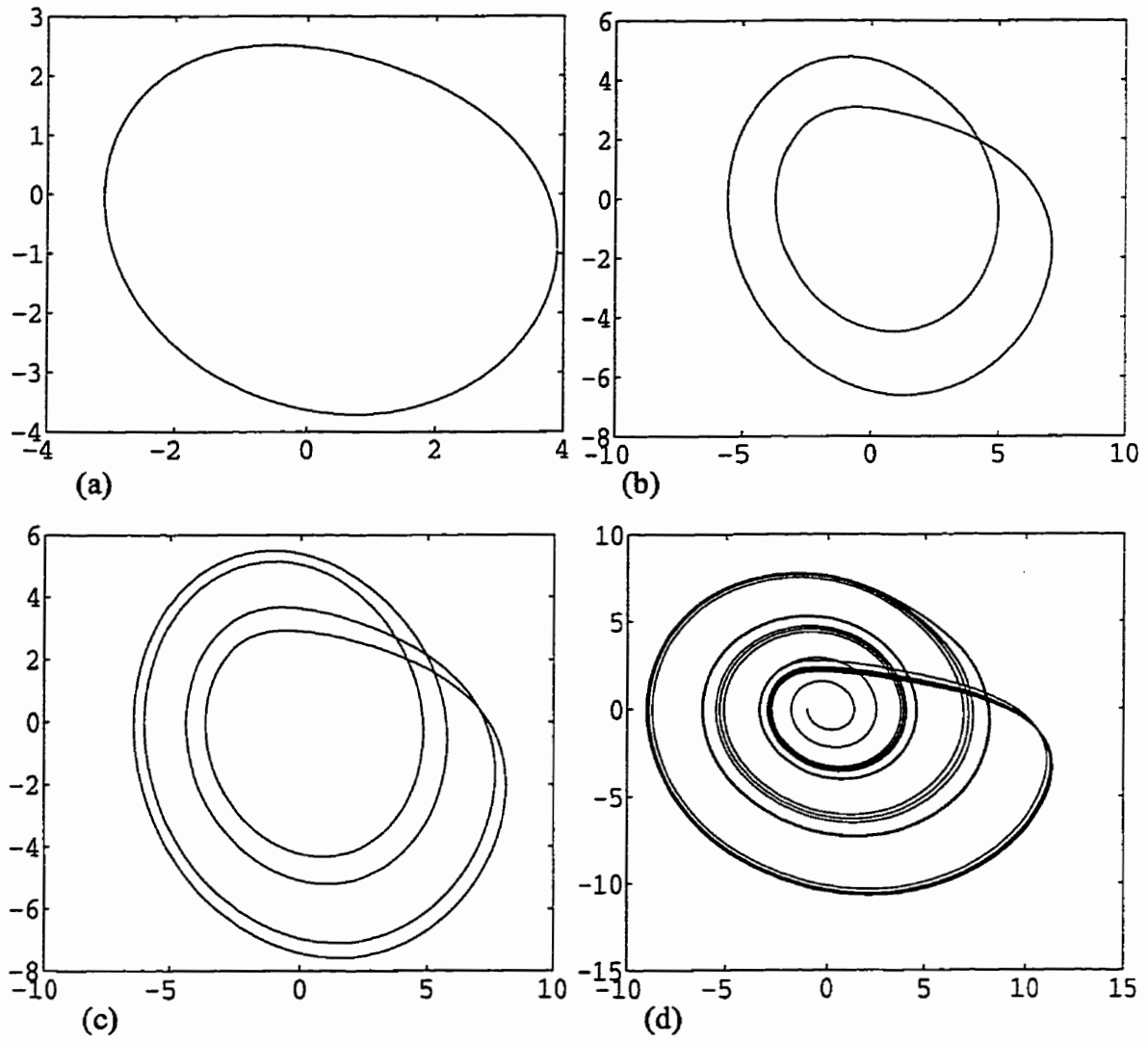

Fig. 3.12. The phase portraits for variables y and x with different values of parameter Υ and $\lambda=\beta=0.2$: (a) $\Upsilon=2.0$, (b) $\Upsilon=3.5$, (c) $\Upsilon=4.0$, and (d) $\Upsilon=5.7$.

The behaviour of the variable z is of particular interest. As shown in Figs. 3.11 and 3.12, we see the sudden firing of the z value which is the main cause of the exponential divergence of the nearby trajectories, and then the attractor is again folded over and the trajectories are reinjected back to the center of the attractor.

3.3 Complexity Measures and Multifractals

The morphological dimensions of an attractor are measures for its spatial scaling properties. We can apply the box-counting dimension, D_B, as defined before on the attractors. The dimension of the hypercubes should be chosen equal to the Euclidean dimension of the phase space, i.e., the number of degrees of freedom of the system. But the morphological dimensions are not capable of revealing the complexity of the fractal objects fully. In this section other measures are presented for a complete description of the complexity of the fractal objects. We also see how to use these measures for the study of the complexity of strange attractors.

3.3.1 Information Dimension

The information dimension, D_I, is a measure of the differences in the distribution density of the points covering the object. For the calculation of D_I, the object is covered with hypercubes of side length δ. But this time instead of only counting the number of cubes which contain part of the object, we calculate a probability P_i for each hypercube i of side length δ. P_i is the probability of part of the object occuring within the hypercube i. Then $H(\delta)$ is calculated as

$$H(\delta) = -\sum_{i=1}^{N} P_i \log (P_i) \tag{3.17}$$

where N is the number of covering hypercubes of side length δ.

The *information dimension* is estimated by repeating the above procedure for a diminishing range of δ as shown below [Kins94]

$$D_I = \lim_{\delta \to 0} \frac{H(\delta)}{\log(1/\delta)} \tag{3.18}$$

If an object is evenly distributed, an identical probability of $P_i = 1/N$ will reduce the information dimension to the box-counting dimension since $H(\delta) = \log(N)$. We see that in this dimension calculation each hypercube is weighed according to the probability of the object occuring in it.

$H(\delta)$ is in fact the Shannon entropy of the system, that means the quantity $H(\delta)$ specifies the amount of information necessary to specify a point of the fractal object to within an accuracy of δ. In other words, it is the information obtained in making a measurement that is uncertain by an amount δ.

3.3.2 Correlation Dimension

The correlation dimension is another improvement for characterizing the density distribution of a fractal. As usual, the fractal is covered with N hypercubes of side length δ. The probabilities, P_i, are calculated as explained for the information dimension. The *correlation dimension*, D_C, is calculated as [Kins94]

$$D_C = \lim_{\delta \to 0} \frac{\log \sum_{i=1}^{N} P_i^2}{\log(1/\delta)} \tag{3.19}$$

Similar to the self-similarity dimension, D_C can be obtained from the slope of a log-log plot of the variables $1/\delta$ and the corresponding probability ensembles.

We now explain the concept of pair correlation function, C_δ, and how it is related

to the correlation dimension. Suppose that in a real experiment $N_{T\delta}$ points of a fractal has been collected. The *pair correlation function* is defined as

$$C_\delta = \lim_{N_{T\delta}\to\infty} \frac{N_{P\delta}}{N_{T\delta}^2} \tag{3.20}$$

where $N_{P\delta}$ is the total number of pairs of points in the fractal such that their distances are smaller than δ. We can estimate D_C using the calculated C_δ as

$$D_C \approx \lim_{\delta\to 0} \frac{\log(C_\delta)}{\log(1/\delta)} \tag{3.21}$$

The Euclidean definition of distance is used in this thesis, although the concept of distance is general in the definition above. For showing why D_C can be estimated using C_δ, we consider an overlapping or a non-overlapping covering of the fractal. Considering the ith hypercube of side length δ, containing n_i points of the object, the number of the ordered pairs of points inside this hypercube which their distances are smaller than δ is $n_i \times (n_i - 1)$. Therefore, if the covering consists of N hypercubes then $N_{P\delta}$ can be estimated as follows [Kins97]

$$N_{P\delta} \approx \sum_{i=1}^{N} \left(n_i^2 - n_i \right) \tag{3.22}$$

Now we have

$$C_\delta \approx \lim_{N_{T\delta}\to\infty} \frac{1}{N_{T\delta}^2} \sum_{i=1}^{N} \left(n_i^2 - n_i \right) = \sum_{i=1}^{N} \left[\lim_{N_{T\delta}\to\infty} \frac{n_i^2}{N_{T\delta}^2} - \lim_{N_{T\delta}\to\infty} \frac{n_i}{N_{T\delta}^2} \right] \tag{3.23}$$

since the second limit of the last equation is obviously going to zero and since

$$\frac{n_i^2}{N_{T\delta}^2} = P_i^2 \tag{3.24}$$

then

$$C_\delta \approx \sum_{i=1}^{N} P_i^2 \tag{3.25}$$

Its important to note that we have only made an estimation of $N_{P\delta}$ in these calculations. If the covering of the fractal object is non-overlapping then using the pair correlation function will give an over-estimation of the probability ensemble, and if the covering is over-lapping then using the pair correlation function will give an under-estimation of the probability ensemble. The estimation of the D_C using the pair correlation function is commonly used in literature due to its fast and easy implementation . The pair correlation function is calculated by scanning all the points of the object one by one. If the object contains $N_{T\delta}$ points, for each given point $\bar{u}_i$, all the other points $\bar{u}_j$ are tested to see if they fall into a hypercube of side length δ centred at $\bar{u}_j$. According to [GaRa92]

$$C_\delta = \lim_{N_{T\delta}\to\infty}\left[\frac{1}{N_{T\delta}}\sum_{i=1}^{N_{T\delta}}\left[\frac{1}{N_{T\delta}}\sum_{j=1}^{N_{T\delta}}\theta\left(\delta - \|\bar{u}_i - \bar{u}_j\|\right)\right]\right] = \lim_{N_{T\delta}\to\infty}\frac{N_{P\delta}}{N_{T\delta}^2} \tag{3.26}$$

where θ is the Heaviside function.

3.3.3 Natural Measure, Multifractals, and Generalized Rényi Dimensions

Consider a subset B of a space X in which an attractor lies. Orbits that are typically observed in computational studies seem to eventually fill up the attractor densely. If all orbits which start in or near the attractor fill up the attractor densely, then the system is

called *ergodic*. We can count the number of times an orbit enters the subset B, and it is natural to assume that the percentage of all points which are in B stabilize as we perform more and more iterations. This percentage is called the *natural measure,* $\mu(B)$ for the system. The natural measure can be understood as a means of quantifying the mass of a portion of any object.

Now consider a point $\bar{u}$ on an object and hypercubes $B_\delta(\bar{u})$ of side length δ centred at $\bar{u}$. The probability or the mass contained in this hypercube is $\mu(B_\delta(\bar{u}))$. α is the exponent in the power law relationship which specifies how fast this mass decreases as δ decreases to zero.

$$\mu(B_\delta(\bar{u}))\,\alpha\delta^{\alpha} \tag{3.27}$$

$$\alpha = \lim_{\delta \to 0} \frac{\log\mu(B_\delta(\bar{u}))}{\log\delta} \tag{3.28}$$

The exponent α is also called the Holder exponent at point (x, y). If this scaling law holds for all points on the object with the same α, then the object is a homogeneous fractal. If α varies for different regions then the object is called an inhemogeneous fractal or a *multifractal* [Kins97].

It can be easily seen that for a uniformly distributed mass of points in an object we will have

$$D_C = D_I = D_B \tag{3.29}$$

While for an object with non-uniform distribution of mass we get

$$D_C \le D_I \le D_B \tag{3.30}$$

The values for D_C and D_I approach D_B as the object becomes more uniformly distributed. As we can see the relation of the three dimensions, i.e., their equality or their unequality can be a measure of uniformity or non-uniformity of the mass distribution of the object. One single dimension is inadequate for describing the distribution of different densities in the fractal set. In fact, if an object contains two or more merged fractals, the fractal with the larger dimension will mask the fractal with the lower dimension [Chen97]. One single value is not able to manifest the richness of the complexity of the object. Rényi generalized the idea of one dimension to introduce the spectrum of Rényi dimensions [GrPr84][Kins97]. Considering a covering of an object with N hypercubes of side length δ

$$H_q(\delta) = \frac{1}{1-q}\log \sum_{i=1}^{N} P_i^q \qquad -\infty < q < \infty \tag{3.31}$$

$$D_q = \lim_{\delta \to 0} \frac{H_q(\delta)}{\log(1/\delta)} \tag{3.32}$$

where P_i is the probability of the object occurring in the i th hypercube of side length δ. Note that $P_i = \mu(B_i)$. The D_q is monotonic and strictly decreasing for a multifractal object. q is a real value and D_q has an infinite number of values. When q approaches ∞ then the ensemble shows the contribution of the largest P_i. When q approaches $-\infty$ the ensemble shows the contribution of the smallest P_i. This can be proven as below

[Kins97] (3.33)

$$D_{\infty} = \lim_{q \to \infty} \lim_{\delta \to 0} \frac{1}{q-1} \left(\frac{\log \sum_{i=1}^{N} P_i^q}{\log(\delta)} \right) = \lim_{\delta \to 0} \frac{\log P_{max}}{\log(\delta)}$$

where P_{max} is the largest non-zero probability. Similarly

$$D_{-\infty} = \lim_{q \to -\infty} \lim_{\delta \to 0} \frac{1}{q-1} \left(\frac{\log \sum_{i=1}^{N} P_i^q}{\log(\delta)} \right) = \lim_{\delta \to 0} \frac{\log P_{min}}{\log(\delta)} \quad \text{[Kins97]} \qquad (3.34)$$

where P_{min} is the lowest non-zero probability. For $q = 0$ the Rényi dimension reduces to the D_S [Kins97]

$$D_0 = \lim_{\delta \to 0} \frac{1}{q-1} \left(\frac{\log \sum_{i=1}^{N} P_i^0}{\log(\delta)} \right) = \lim_{\delta \to 0} \frac{\log N_\delta}{\log(\delta)} = \lim_{\delta \to 0} \frac{\log N_\delta}{\log(1/\delta)} = D_S \qquad (3.35)$$

For $q = 1$ the Rényi dimension reduces to the D_I. Since $H_q(\delta)$ cannot be calculated directly we apply L'Hopitall's rule to get the limit

$$H_1(\delta) = \lim_{q \to 1} \frac{1}{1-q} \log \sum_{i=1}^{N} P_i^q = -\lim_{q \to 1} \left[\frac{1}{\sum_{i=1}^{N} P_i^q} \right] \left[\frac{d}{dq} \sum_{i=1}^{N} P_i^q \right] \log_2 e \qquad (3.36)$$

and since $\frac{dc^x}{dx} = c^x \ln c$

$$H_1(\delta) = -\lim_{q \to 1} \left[\frac{\sum_i P_i^q \ln P_i}{\sum_{i=1}^{N} P_i^q} \right] \left(\frac{1}{\ln 2} \right) = -\sum_{i=1}^{N} P_i \log (P_i)$$

[Rifa98] (3.37)

For $q = 2$ the Rényi dimension reduces to the D_C

$$D_2 = \lim_{\delta \to 0} \frac{1}{2-1} \left(\frac{\log \sum_{i=1}^{N} P_i^2}{\log (\delta)} \right) = \lim_{\delta \to 0} \frac{\log \sum_{i=1}^{N} P_i^2}{\log (\delta)} = D_C \text{ [kins97]} \qquad (3.38)$$

A comprehensive and unified presentation of the dimensions can be found in [Kins97]. The concept of a pair correlation function can be extended to a q-tuple correlation function, considering counting the q-tuples of different points having distances smaller than δ in the object. Therefore, we can obtain an estimation of D_q with calculating the q-tuple correlation function. The proof can be shown with a similar assumption and procedure as for pair correlation.

The works of Grassberger and Procaccia [GrPr83a][GrPr83b] for efficient computation of the pair correlation function has been expanded by Pawelzik and Schuster [PaSc87] and Atmanpacher [AtSV88] to show that higher order Rényi dimensions can be calculated efficiently for strange attractors using the pair correlation function. Consider a d-dimensional phase space of a system which is covered with hypercubes of side length δ . P_i is the probability that a trajectory on the attractor visits the hypercube i, and N is the number of non-empty hypercubes. Recall the definition of the D_q dimension

$$D_q = \lim_{\delta \to 0} \frac{H_q(\delta)}{\log(1/\delta)} \tag{3.39}$$

$$H_q(\delta) = \frac{1}{1-q} \log \sum_{i=1}^{N} P_i^q \tag{3.40}$$

Since the $\sum_{i=1}^{N} P_i^q$ can be written in terms of the natural probability measure $\mu(x)$ we can write

$$\sum_{i=1}^{N} P_i^q = \int d\mu(x)\, \mu(B_\delta(x))^{q-1} \tag{3.41}$$

where $B_\delta(x)$ stands for a hypercube of side length δ around the point x on the trajectory. By ergodicity of the trajectories of strange attractors we can write

$$\sum_{i=1}^{N} P_i^q = \frac{1}{N_T} \sum_{j=1}^{N_T} \tilde{P}_j^{q-1}(\delta) \tag{3.42}$$

where N_T is the total number of the points on the trajectory counted in the experiment. $\tilde{P}_j^{q-1}(\delta)$ is the probability to find a point of the trajectory within a hypercube of side length δ around the point j of the trajectory. The change from q to $q-1$ is due to the fact that we are switching from calculating the probability of finding the trajectory in one of the homogeneously distributed boxes covering the attractor to the probability to find the trajectory within a hypercube around one of the inhomogenously distributed points of the trajectory. Since

$$\tilde{P}_j(\delta) = \frac{1}{N_{T\delta}} \sum_{j=1}^{N_{T\delta}} \theta(\delta - \|\bar{u}_i - \bar{u}_j\|) \tag{3.43}$$

where θ is the Heaviside step function and $\bar{u}_i$ and $\bar{u}_j$ are the vector representations of the points on the trajectory, combining these equations with the definition of D_q we derive the final equations which are used through the rest of the thesis for calculating the Rényi dimensions of the strange attractors.

$$C_{\delta q} = \lim_{\delta \to 0} \left[\frac{1}{N_{T\delta}} \sum_{i=1}^{N_{T\delta}} \left[\frac{1}{N_{T\delta}} \sum_{j=1}^{N_{T\delta}} \theta \left(\delta - \left\| \bar{u}_i - \bar{u}_j \right\| \right) \right]^{q-1} \right]^{1/(q-1)} \tag{3.44}$$

$$D_q = \lim_{\delta \to 0} \frac{\log (C_{\delta q})}{\log (\delta)} \tag{3.45}$$

3.4 Summary

In this chapter, we reviewed the basic concepts involved in the study of fractal objects and their morphological and entropy dimensions. We also reviewed the concept of multifractality and the spectrum of Rényi dimensions. We saw that deterministic dynamical systems can behave in a complicated manner that is referred to as chaos and the phase portraits of these chaotic systems have a fractal structure. In the next chapter we will continue the study of strange chaotic attractors and we will review the methods for reconstruction of the attractors from experimental time series. We will also investigate further the correlation function method for the calculation of the Rényi dimensions for strange attractors.

CHAPTER IV

RECONSTRUCTION OF STRANGE ATTRACTORS

In this chapter the implementation of the correlation integral to calculate D_q is discussed. We explain how to determine the range of size of the hypercubes in the covering and how to calculate the dimensions by estimating the power law relationship of the q th order ensemble of probabilities with the sizes of hypercubes. The relationship between the number of points on the trajectory and the calculated dimensions are also discussed. The second section of this chapter discusses the problem of reconstructing the attractors using the trajectory of single variables and the difficulties involved in this process. We specifically discuss the techniques used for choosing the best lag and the best embedding dimensions for the reconstruction of the phase spaces. The third section presents techniques for distinguishing between chaotic and non chaotic data. The trajectory of the attractors implemented in Chapter 3 are used to investigate the techniques presented in this chapter.

4.1 Spectrum of Rényi Dimensions for Strange Attractors

4.1.1 Calculation of the Correlation Integral

The calculation of the Rényi dimensions of attractors can be implemented using the q th order correlation integral

$$C_{\delta q} = \lim_{\delta \to 0} \left[\frac{1}{N_{T\delta}} \sum_{i=1}^{N_{T\delta}} \left[\frac{1}{N_{T\delta}} \sum_{j=1}^{N_{T\delta}} \theta \left(\delta - \left\| \bar{u}_i - \bar{u}_j \right\| \right) \right]^{q-1} \right]^{1/(q-1)} \tag{4.1}$$

$$D_q = \lim_{\delta \to 0} \frac{\log (C_{\delta q})}{\log (\delta)} \tag{4.2}$$

First, the trajectory of each of the independent variables of the system is produced using the fourth order Runge-Kutta technique for numerical solution of dynamical differential systems. The ergodicity of the system implies that a single trajectory of the system fills the attractor densely, therefore, we can estimate the fractal dimension of the attractor using a single orbit. In order to calculate the correlation sum, $C_{\delta q}$, for a specific value of hyper-cube, δ, we have to visit every point in the trajectory and calculate the distance of the point to all the other points. This way, for each point $\bar{u}_i$ on the trajectory we can count the number of points that fall into a hypercube of size δ centred on $\bar{u}_i$. Dividing the number of points in each hypercube by the total number of the points in the trajectory, $N_{T\delta}$, gives the probabilities needed for calculating the ensemble. The next step is to raise each probability to the power of $q-1$ and add up all the results to obtain the final value of

$$\sum_{i=1}^{N_{T\delta}} \left[\frac{1}{N_{T\delta}} \sum_{j=1}^{N_{T\delta}} \theta \left(\delta - \left\| \bar{u}_i - \bar{u}_j \right\| \right) \right]^{q-1} \tag{4.3}$$

$C_{\delta q}$ is then calculated using this result.

Finally, the D_q can be estimated by repeating the same process for several values of δ and calculating the $C_{\delta q}$ corresponding to each of them. D_q is estimated by the power law relationship between δ and $C_{\delta q}$. Therefore, we use a log-log plot of these two variables to estimate D_q similar to the technique we used for the dimensions presented in Chapter 3. Now three questions have to be answered: How to choose the best ranges for the sizes of the hypercubes? How to distinguish the linear region of the log-log plots and how to approximate the slope of them?

In order to find the best range of sizes of the hypercubes we have to make sure that the chosen range includes the upper and lower saturation levels of the probabilities. We have to consider that in real computations we always have a limited number of points of the attractor. If the size of the hypercubes is larger than the size of the attractor, the whole attractor fills in the hypercubes and the value of the probabilities and consequently the value of $C_{\delta q}$ reaches a saturation point. We can see this effect in the log (δ) - log ($C_{\delta q}$) plots where the curve begins to taper off and becomes horizontal as further increases in the hypercube size do not increase $C_{\delta q}$. This can be seen in Fig. 4.1.

For small ranges of δ, the probabilities should not saturate theoretically because the attractor has a structure similar to the Cantor dust and as we zoom in, finer and finer structure should be revealed and we should be able to get arbitrarily close to each point. But due to the finite resolution of the computed attractor, we actually reach a lower range of δ where passing that range the number of points in each hypercube stays fixed. The lower range of δ depends on the number of points we generate for the attractor and the time step, Δt, that we use for solving the differential equations numerically. We can see the effect of the lower saturation level on the log (δ) - log ($C_{\delta q}$) curve as the line begins to fluctuate when the values of $C_{\delta q}$ are no longer accurate representatives of the structure.

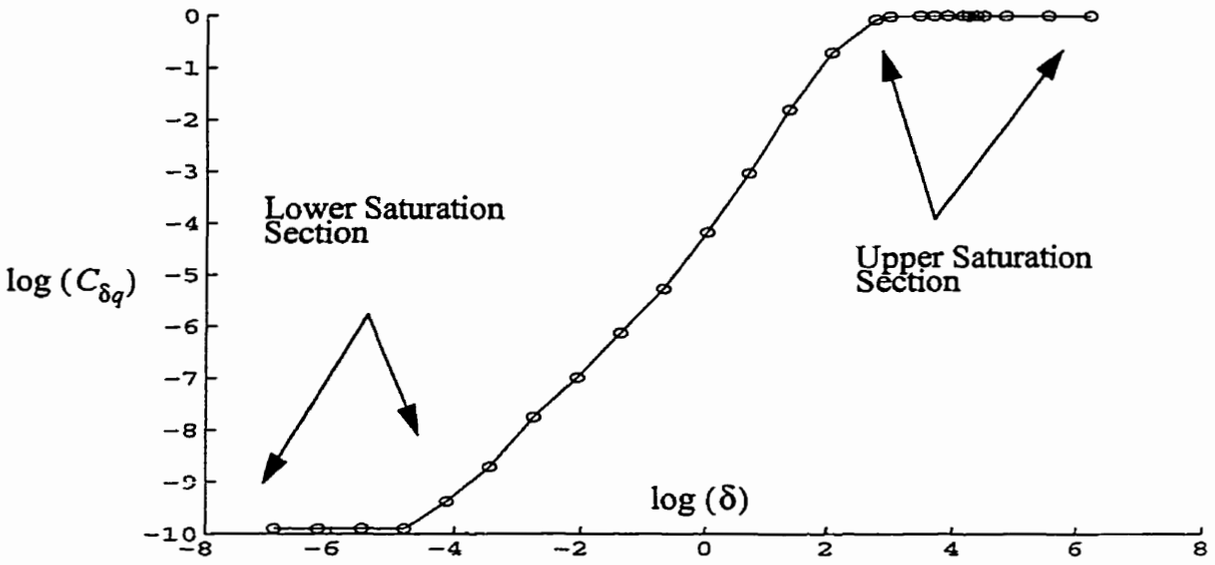

Fig. 4.1. The linear region in the log-log curve is situated between the upper saturation region and a curved section at the smaller values of δ resulted from the finite resolution of the attractor on the computers.

The range of sizes of the hypercubes is best chosen as a dyadic range. Since the approximation of the slope is performed on a logarithmic plot of base two, the values of the δ are best chosen as powers of two. The linear region of the log-log plot lies between the upper saturation region and the lower curved section. After determining the linear region, the dimension is approximated by calculating the slope of the line which best fits in the points on the linear region. The best fit is performed in this thesis using the mean squared error technique We should note that the upper saturation level is the same for the log-log curves of all values of q. For a smooth estimation of the D_q function we choose the linear region common among the log-log curves of all values of q. The biggest hypercube of the common linear region is determined by the common upper saturation point. The smallest hypercube of the common linear region is chosen in a way to exclude the fluctuations of all the curves.

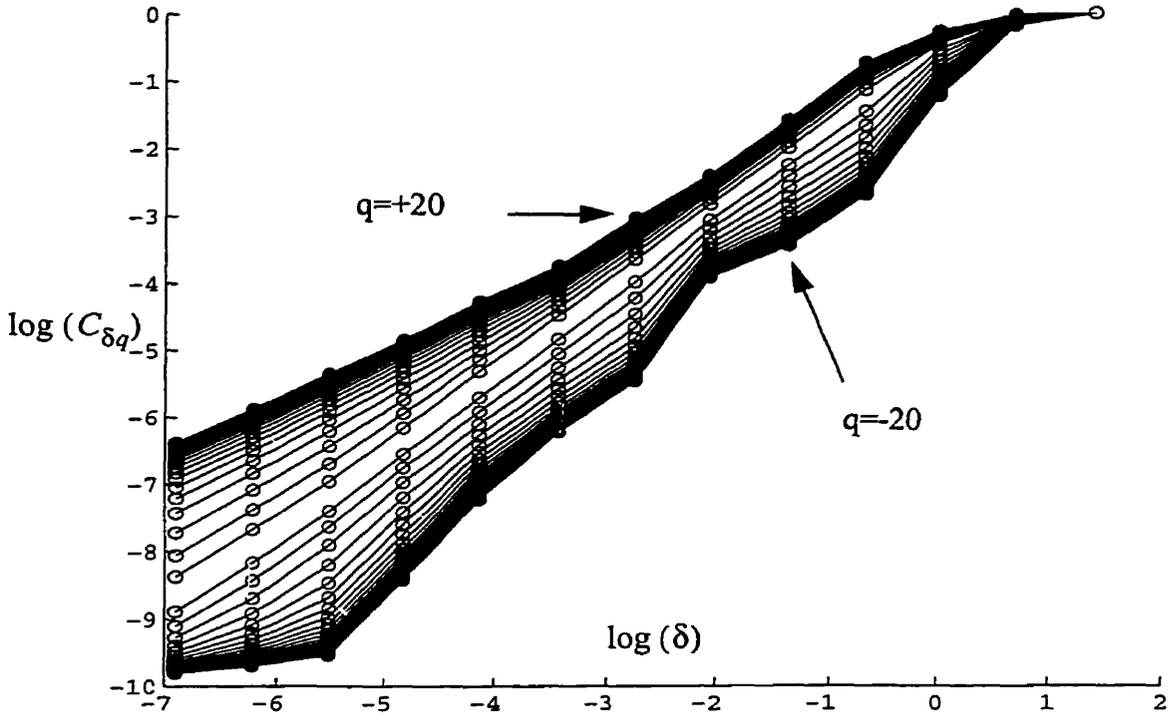

Fig. 4.2. The common linear region in this log-log plot lies between the third hypercube size and the tenth hypercube size, counting from left to right. Each of the curves in the plot correspond to a different value of q, which ranges from -20 to +20 (integer values).

Using the current approach for estimating the Rényi dimensions, one is faced with the issue of repeatability. Can one consistently locate the linear region for approximating the slope without a guide and a priori knowledge of the correct slope? We should note that distinguishing the linear region of the log-log plots is usually done visually. The computational technique used in the experiments in this thesis is based upon the successive differences of the $\log (C_{\delta q})$ coordinate of the $\log (C_{\delta q})$ -$\log (\delta)$ plot. The successive differences are compared with two tolerance ranges which pinpoint the onset of the linear range and the upper saturation level. The results of this computation is, however, always checked and sometimes modified, since the log-log plots are not always monotonically

increasing in the linear regions, especially for the negative values of q. It is important to note that small alterations in the choice of the linear region can effect the bounds and the shape of the S-shaped D_q curves. Since there is no uniform and standardized technique in the literature, in this thesis we will explicitly state the upper and lower range of the linear region for each experiment, to ensure the repeatibility of the experiments.

It is not possible to calculate the value of D_q at q=1 directly from the correlation integral. Therefore, based upon the monotonically decreasing shape of the S-curve, we non-linearly interpolate this value by calculating the correlation integral at real q very close to q=1. This can be compared to finding the value of D_1 as the limit of correlation integral for $q \rightarrow 1$.

Figure 4.3 shows the results of the calculation of the Rényi dimensions for the Hénon and Rössler attractors. The parameters of the system and the initial values for generating the trajectories stays the same for all the experiments to the end of this chapter so we will not repeat them later.

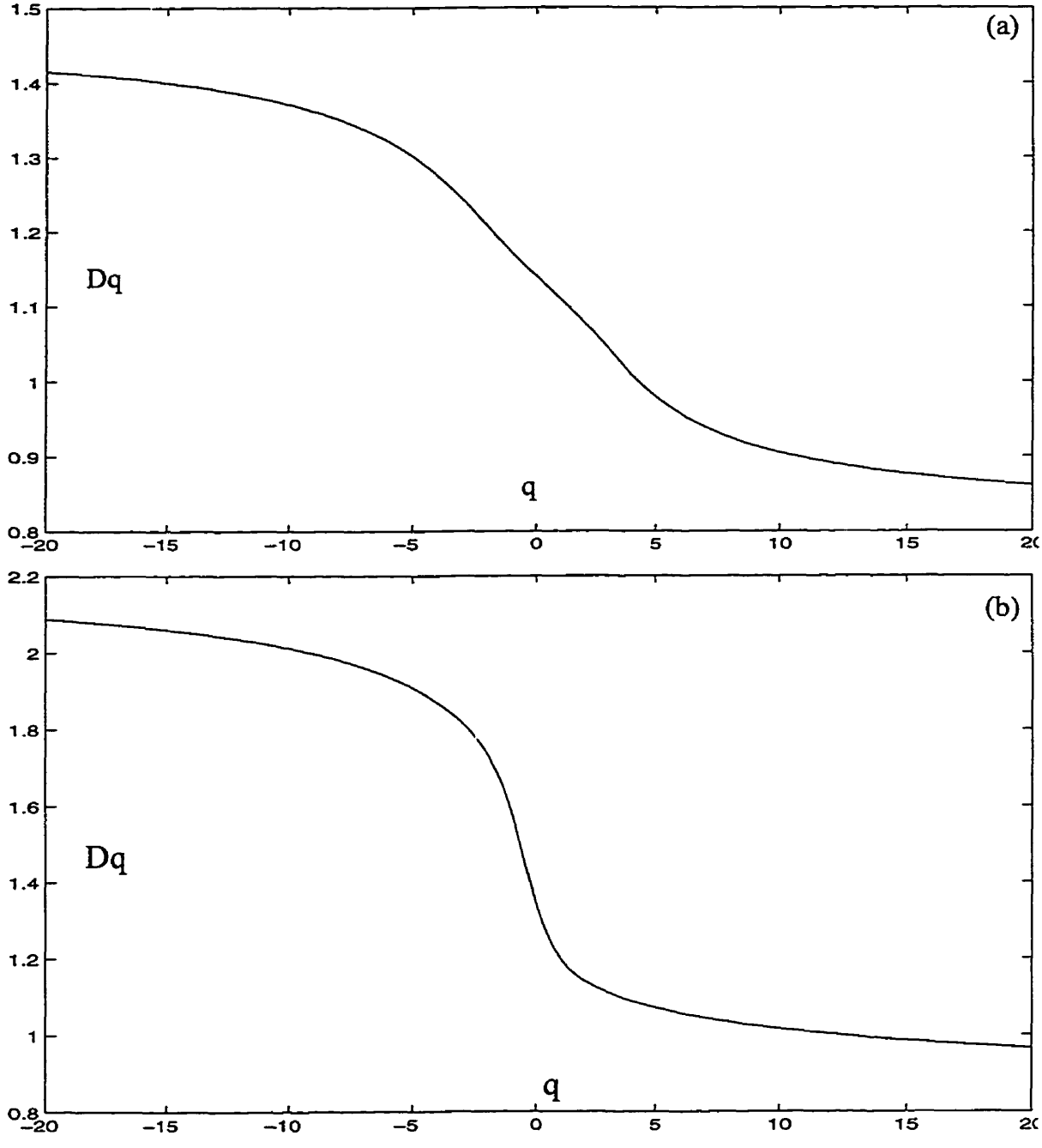

Fig. 4.3. (a) The Rényi dimensions of the Hénon attractor. Data size=20000 after discarding 10000 points of the trajectories. a=1.4, b=0.3, x(0)=y(0)=0.8, the hypercube sizes form 0.001 to 4.096 dyadic range. The linear region hypercubes range from 0.004 to 4.096. (b) The Rényi dimensions of the Rössler attractor. Data size=20000 after discarding 10000 points of the trajectories. $\lambda = \beta = 0.2$, $\Upsilon = 5.7$, x(0)=-1, y(0)=z(0)=0, hypercube ranges 0.001 to 512 with a dyadic range. The linear range of the hypercubes are 0.5 to 64.

4.1.2 Length of the Time Series

In this section we compare the performance of the correlation integral technique for trajectories of different lengths. The lengths of 2000 to 10000 points have been examined for estimation of the D_q curve using the time trajectories of the Hénon attractor. Theoretically, increasing the size of the time series fills the attractor more densely, therefore the estimation of the Rényi dimensions becomes more accurate.

The experiments confirm the theoretical expectation. Figures 4.4 and 4.5 show the convergence of the D_q curves with an increasing point count in the x and y trajectories. After 10000 points, the D_q curves converge to almost the same values within an error range of 0.001. Increasing the size of the trajectories can be implemented either by increasing the observation time or by decreasing the time step used for sampling the trajectories.

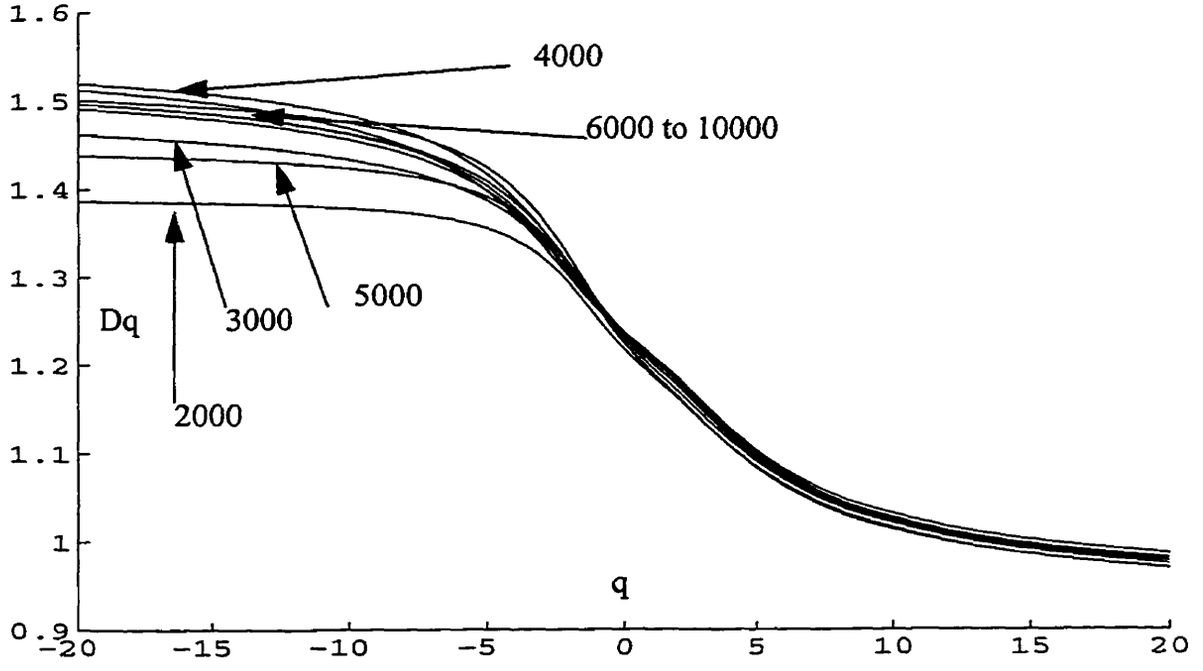

Fig. 4.4. The convergence of the Rényi dimensions of the Hénon attractor by increasing the length of the time series from 2000 points to 10000 points. The linear range of hypercubes are from 0.004 to 4.096.

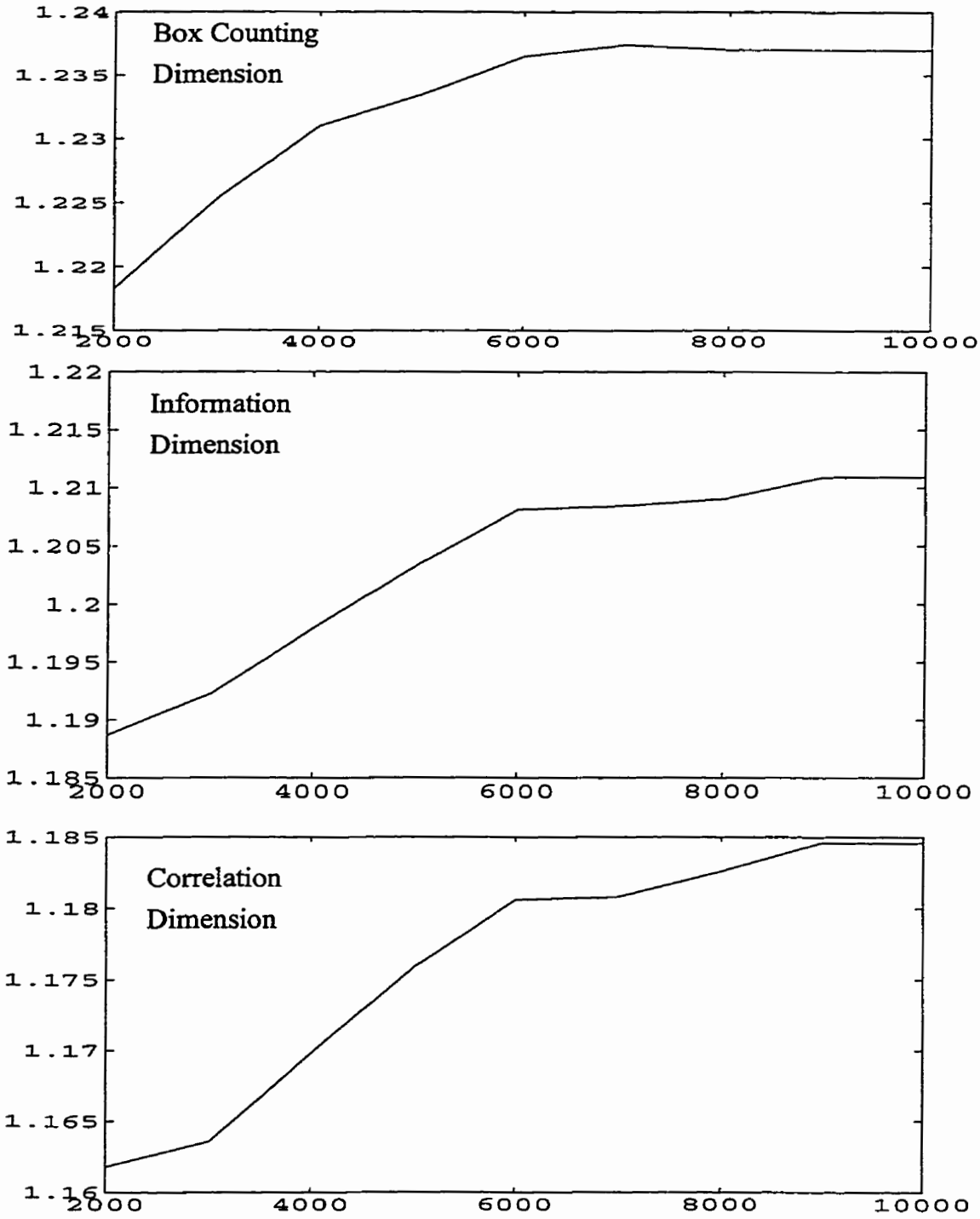

Fig. 4.5. The convergence of the box-counting, information, and the correlation dimension of the Hénon attractor by increasing the length of the time series from 2000 to 10000. The linear region hypercubes range from 0.004 to 4.096. After 9000 points the errors are within a range of ± 0.001 and after 10000 points the errors are within a range of ± 0.0001 .

4.1.3 Added Noise

In this section we investigate the effect of additive noise to the original data in the estimation of the D_q curve. This is accomplished by comparing the D_q curves of the original Rössler attractor with the curves estimated from a noisy Rössler attractor. The noisy attractor is generated by the superposition of white noise to the x, y and z trajectories of Rössler attractor. The white noise is generated by a random number generator of uniform distribution, and it is scaled by an appropriate factor in order to achieve a desired signal-to-noise ratio (SNR). The SNR is the ratio of the energy of the noise free signal to that of pure noise or the error of the signal and is calculated as

$$SNR = 10\log\left(\frac{E_s}{E_e}\right) \tag{4.4}$$

$$E_s = \sum_n s[n]^2 \tag{4.5}$$

$$E_e = \sum_n (s[n] - \hat{s}[n])^2 \tag{4.6}$$

where $s[n]$ is the original signal and $\hat{s}[n]$ is the noisy signal. Figure 4.6 contains the log-log plots of the signals with SNR of 5, 100 and 500. Comparing the plots together we can discern the fact that for lower signal to noise ratios the linear region of the log-log plot is shorter. For SNR=5 the lower end of the linear regions begin at hypercubes of larger size in comparison to SNR=500. This effect can be explained by the relationship of the size of the hypercubes and the noise levels. For hypercubes of sizes smaller than the noise levels the probabilities are affected by the random noise displacement of the points. For experimentation purposes it is always important to state the SNR of the signal and keep the probing hypercube sizes larger than the noise levels.

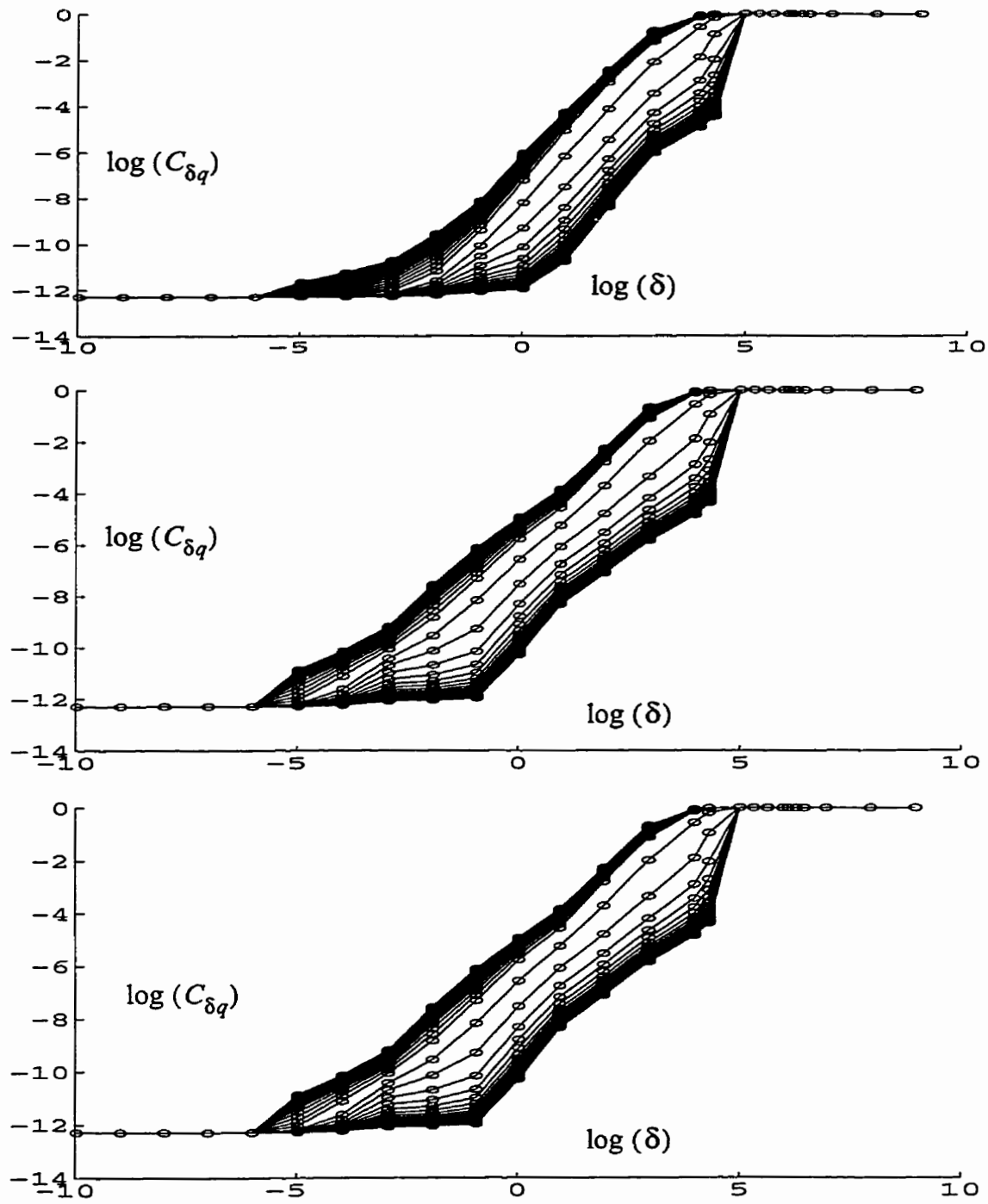

Fig. 4.6. The log-log plots of the Rössler attractor contaminated with noise. (a) SNR=5 (b) SNR=100 (c) SNR=500. The linear region of the signal with lower SNR is shorter due to the effect of the noise in probabilities of the probing hypercubes with sizes comparable to the noise levels. These fluctuations disappear at higher SNR.

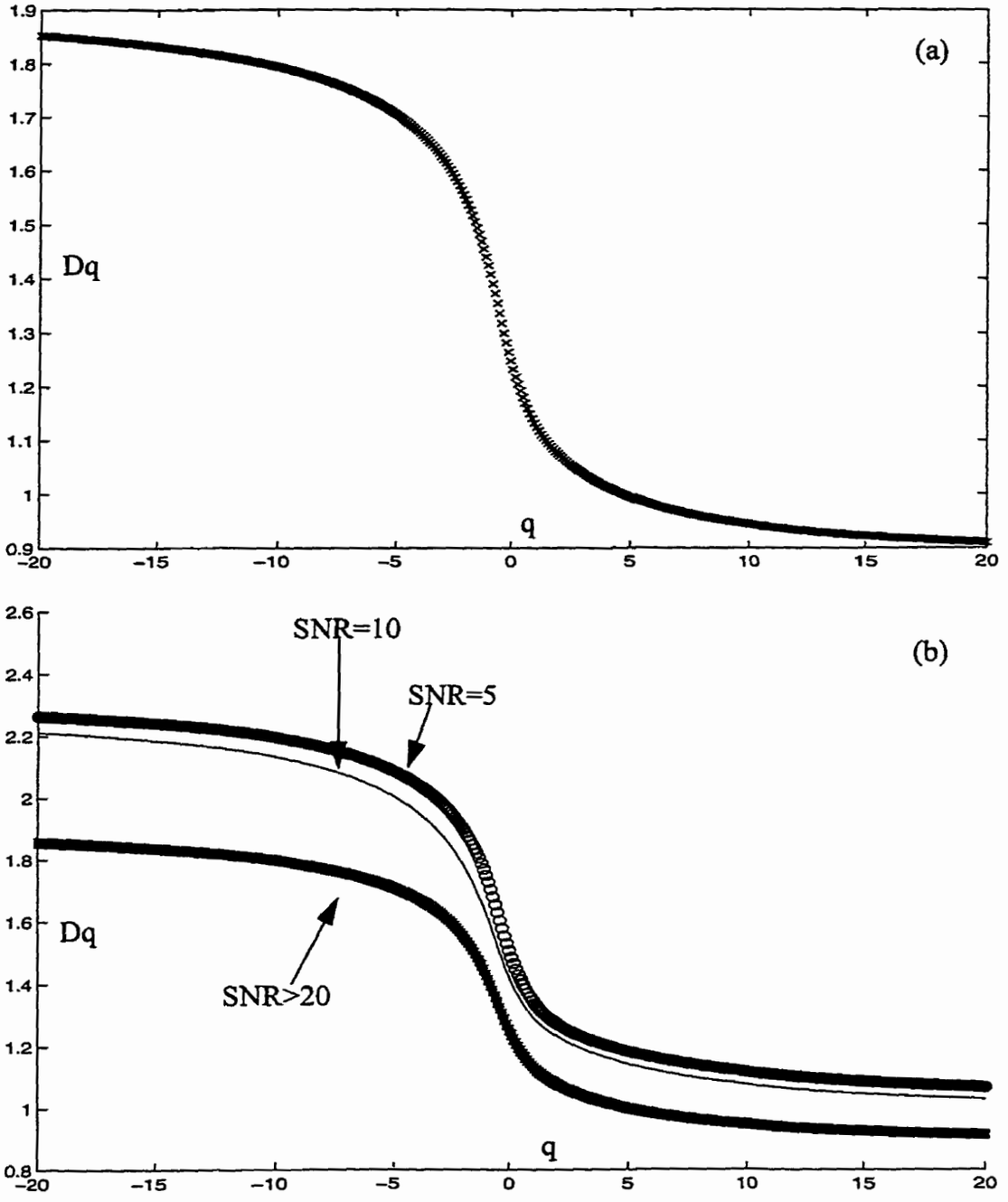

Fig. 4.7. The Dq curves calculated for (a) the original Rössler attractor, and (b) the Rössler attractor contaminated with noise. The curves for SNR=5, 10, 20, 30, 40, and 100 is plotted. For SNR larger than 20, the curves fall on each other and converge to the original attractor's dimensions. The original attractor is from a time series of length 5000 with a dyadic range of hypercubes from 0.001 to 512 and linear range is between 0.5 to 64.

The results of the experiments with the Rössler, and Hénon, and Lorenz attractors show that the D_q curve is stable with signal-to-noise ratios larger than 20, i.e. the S-curve converges to an error range of smaller than ± 0.001. It is important to mention that the adopted noise model represents a worst case because the white noise contaminates the signal across an infinite bandwidth.

4.2 The Reconstruction of Strange Attractors

In order to model a non-linear chaotic natural phenomenon, many experiments have to be conducted to determine the set of non-linear differential equations which govern the system. But if the existence of an underlying attractor is proved we can characterize the phenomenon using its multifractal features. It first has to be determined whether the underlying system is a deterministic system or a stochastic system, and whether the measured data is random noise or chaotic data. Then knowing the trajectories of all the independent variables of the system, the characterization can be done by calculating the spectrum of the Rényi dimensions of the strange attractor. But the problem is that we generally do not have enough information about all the variables and often we speculate the system using the trajectory of one measured variable.

Now the question is, are we able to estimate the Rényi dimensions of an attractor using only the trajectory of one measured variable? Are we able to reconstruct some meaningful picture of the attractor using the one available trajectory?

4.2.1 Reconstruction of the Phase Space

The question of reconstructing an attractor from the trajectory of one variable was first addressed by Packard *et al.* [PCFS80]. They found that having a time series obtained

by sampling a single coordinate, $x(t)$, of an attractor one can obtain a variety of m independent quantities which appear to yield a faithful phase space representation of the dynamics in the original space.

One possible set of these quantities are

$$x(t), x(t-\tau), x(t-2\tau), \ldots, x(t-m\tau)$$

The value τ is called the *lag* of the time series and m is the *embedding dimension* of the reconstructed attractor. Now the points on the attractor are given as vectors

$$(x(t_1), x(t_1-\tau), x(t_1-2\tau), \ldots, x(t_1-m\tau))$$

$$(x(t_2), x(t_2-\tau), x(t_2-2\tau), \ldots, x(t_2-m\tau))$$

$$\vdots$$

$$(x(t_N), x(t_N-\tau), x(t_N-2\tau), \ldots, x(t_N-m\tau))$$

where N is the size of the time series. Another set proposed by [PCFS80] is

$$x(t), \frac{dx}{dt}, \frac{d^2x}{dt}, \ldots, \frac{d^mx}{dt}$$

To obtain a heuristic understanding of the idea of the reconstruction of the attractors we attempt to reconstruct the Hénon and Rössler attractors using trajectories of single variables. In Fig. 4.8 and 4.9 for Hénon attractor, it can be seen that there is significant correlation between each point in the time series and its previous sample. The phase space of the reconstructed attractor for τ=1 resembles the shape of the original Hénon attractor. Apparently the structure contained in relationships of x, y variables are encapsulated in the x and $x-\tau$ variables. For τ=2 and τ=3 there is still some relationship which gives a structured appearance to the reconstructed phase space. For τ=10 all structure has van-

ished. The reconstruction has been repeated for both variables, x, and y producing the same results. The attractor can be reconstructed using either of the two independent variables. The embedding dimension of two has been used for the reconstruction of Hénon attractor in Figs. 4.8 and 4.9. The same experiment is performed on the Rössler attractor with different lags and an embedding dimension of three.

The important observation made by Packard *et al.* was formally proved by Floris Taken in 1981, known as the embedding theorem [take81][Mane81]. The embedding theorem establishes that when there is only a single measured quantity from a dynamical system, it is possible to reconstruct a state space that is equivalent to the original state space composed of all the dynamical variables. The embedding theorem states that if the system produces orbits in the original state space that lie on a geometric object of dimension n (which need not be an integer), then the object can be unambiguously seen without any spurious intersections of the orbit in another space of dimension $m > 2n$, comprised of coordinates that are arbitrary non-linear transformations of the original state space coordinates. The absence of intersections in the second space means that the orbit is resolved without ambiguity when m is large enough. Overlaps of the orbit may occur in lower dimensions and the ambiguity at the intersections destroys the possibility of predicting the evolution of the system. It is important to note that Taken's requirement for m is a sufficient but not necessary condition for dynamics reconstruction.

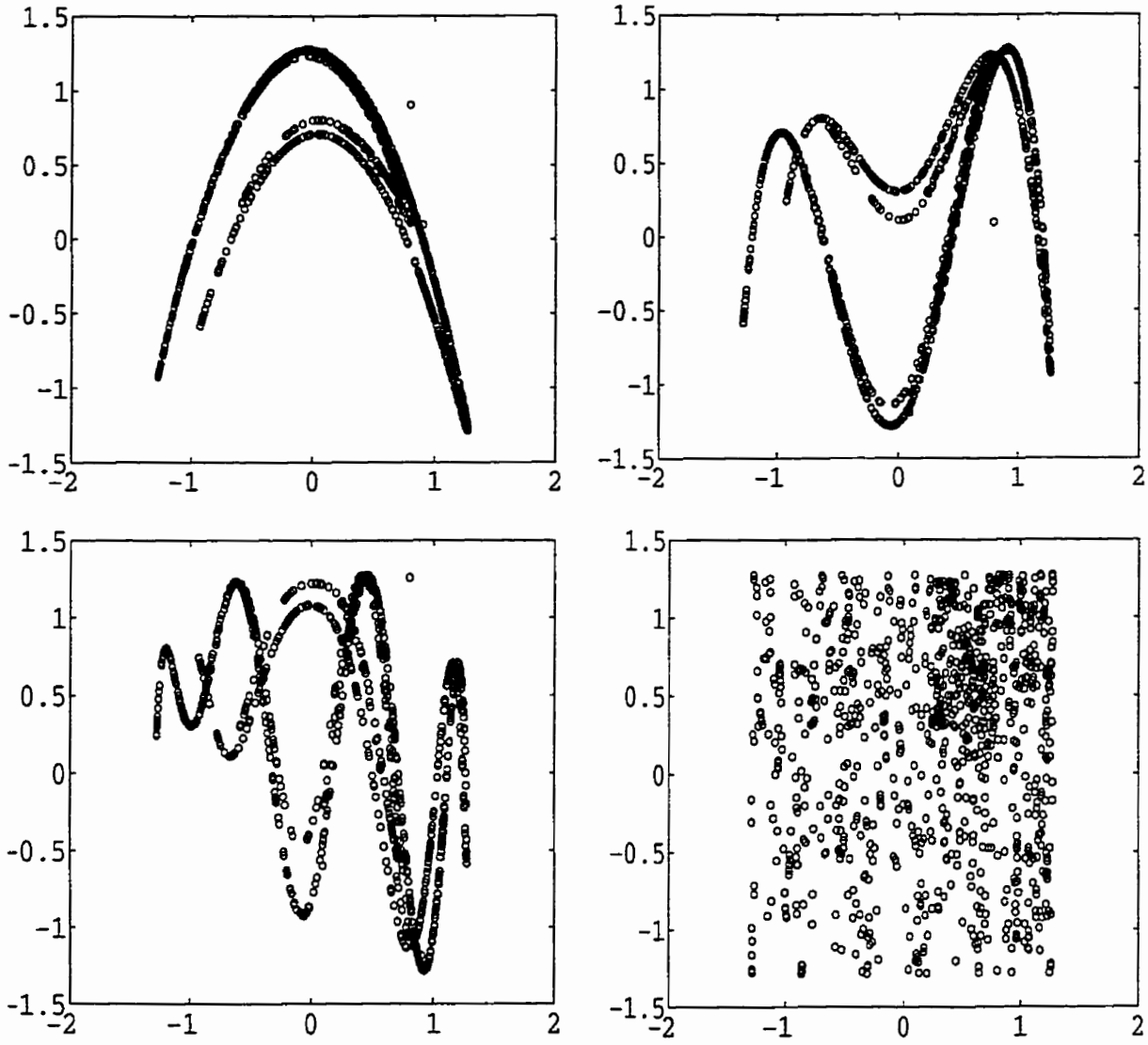

Fig. 4.8. Hénon attractor reconstructed from the values of the variable x, a=1.4, b=0.3, x(0)=y(0)=0.8, embedding dimension=2, and 100 points are used for the reconstruction. Different τ sizes have been used for the reconstruction: (a) τ=1, (b) τ=2, (c) τ=3, (d) and τ=10.

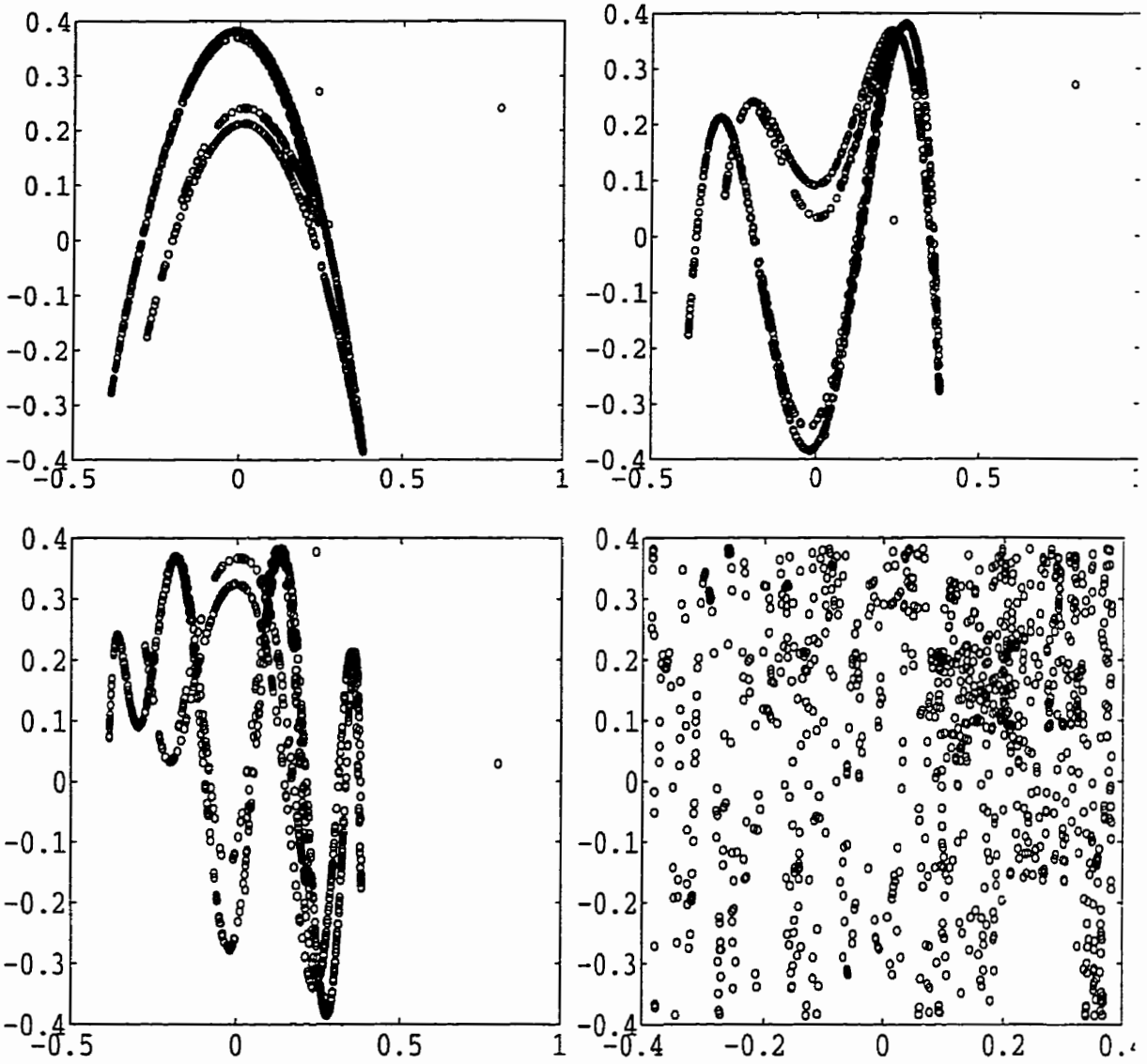

Fig. 4.9. Hénon attractor reconstructed from the values of the variable y, a=1.4, b=0.3, x(0)=y(0)=0.8, embedding dimension=2, and 100 points are used for the reconstruction. Different τ sizes have been used for the reconstruction. (a) τ=1, (b) τ=2, (c) τ=3, (d) and τ=10.

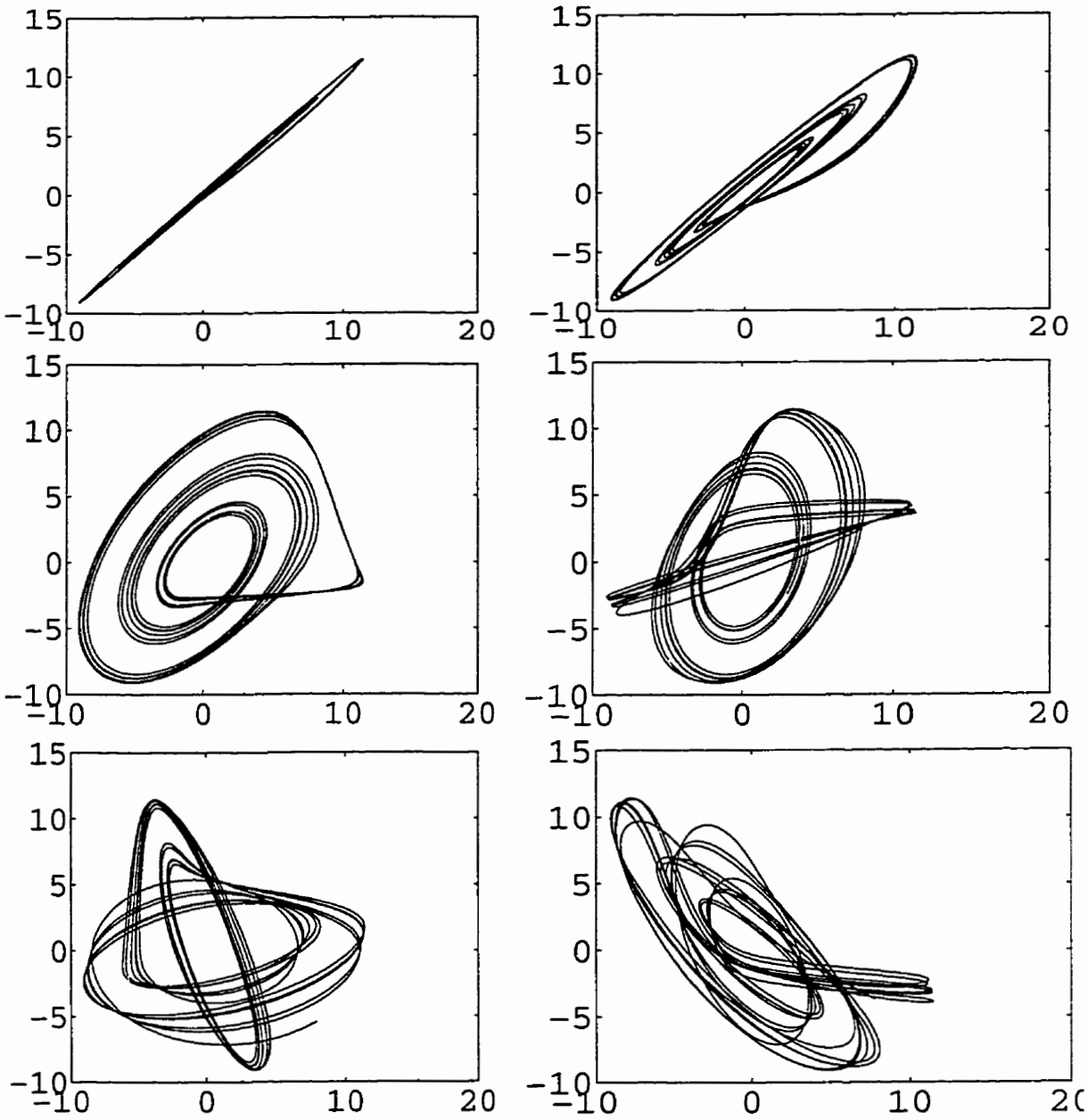

Fig. 4.10. Rössler attractor reconstructed from the values of the variable x, $\lambda = \beta = 0.2$, $\Upsilon = 5.7$, $y(0) = z(0) = 0$, $x(0) = -1$, embedding dimension=3, and 10000 points used for the reconstruction with $\Delta t = 0.01$, Different τ sizes have been used for the reconstruction. (a) $\tau = 3$, (b) $\tau = 17$, (c) $\tau = 100$, (d) $\tau = 500$, (e) $\tau = 1000$, (f) and $\tau = 2000$. For $\tau = 100$ the structure is completely unfolded. For $\tau = 500$ and higher lags the attractor starts to lose its structure.

The embedding theorem does not say anything about the choice of the lag. In fact, it permits us to use any lag so long as the time series is infinitely long. In practice we work with finite length time series therefore we have to take a proper prescription for choosing the lag.

In 1982, Doyne Farmer showed that the reconstruction of strange attractors can be interpreted as a change of coordinates, or in better words unfolding the attractor from its projection onto the observation axis of measurement. Choosing the embedding dimension of $2n + 1$ guarantees that the embedding space is large enough for an injective reconstruction [Farm82]. This means that each point in the reconstructed attractor corresponds to one and only one point in the original attractor. Therefore no part of the attractor will collapse on top of another part because of projection. An injective reconstruction does not effect the fractal dimensions of the attractor.

Formally, an autonomous system producing orbits $\bar{x}(t)$ through the dynamics is

$$\frac{d}{dt}\bar{x}(t) = F(\bar{x}(t)) \tag{4.11}$$

and the output is

$$s(t) = h(\bar{x}(t)) \tag{4.12}$$

$\bar{x}$ is an n-dimensional vector, and $s(t)$ is typically a one-dimensional output signal. The embedding theorem states that any independent set of quantities related to $s(t)$ can serve as the coordinate for a state space of the system.

Time derivatives of $s(t)$ are the natural set of independent coordinates. But when the signal is sampled in discrete time, the derivatives act as high pass filters and emphasize noise in the measurements. But as Packard *et al* had suggested there is another natural set

of coordinates for the state space. The signal $s(t)$ and its time delays are the ingredients in the approximation of the time derivatives of $s(t)$. The time delay values of $s(t)$ are new information that enters the approximation of each derivative. This set of coordinates is realized by forming the vectors

$$(s(t), s(t-\tau), s(t-2\tau), \ldots, s(t-m\tau))$$

where m is the embedding dimension larger than $2n$ and τ is the lag.

If τ is too small, the points of the trajectory will have components which are strongly correlated and very close, therefore the reconstructed attractor will be very close to the diagonal of the space. On the other hand, if τ is too large there is little correlation and the trajectories appear to wander all around the phase space [PaSc87].

Another problem with experimental data is that we may not know the degrees of freedom of the underlying dynamical system or the dimension of the underlying attractor. In this case a practical technique used for finding the best embedding dimension is to calculate the spectrum of the Rényi dimensions for a number of successively increasing embedding dimensions starting from a low dimension of two or three. In the beginning, all the values of the S-curve will increase as we increase the embedding dimension, reaching a limiting value when the embedding space is large enough for the attractor to untangle itself. Further increases should not increase the values of the curve from the converged level [Addi97].

It is important to pay attention to the fact that a dense trajectory in lower dimensions fills an embedding space of much higher dimension sparsely, where the calculation of the S-curve will be inaccurate. Therefore, the size of the time series must be chosen in a way to fill the embedding dimension of largest dimension densely. This can be found by

trial and error, i.e. by experimenting with different sizes in each embedding dimension and studying the convergence of the S-curve for different sizes.

To examine this idea we perform an experiment with the Rössler attractor. We reconstruct the Rössler attractor using its x-variable time trajectory using lag=20. This lag was chosen according to the visual inspection of the reconstructed two-dimensional phase space for different lags. Then we calculate the spectrum of the Rényi dimensions for the embedding dimensions of 3,4,5,6,7 and 8. According to Taken's theorem, an embedding dimension of eight and higher should reach the converging level and give an appropriate reconstruction, therefore the Rényi dimensions for the reconstructed attractor for embedding dimension of eight and higher converges to the Rényi dimensions of the original attractor. The results of this experiment are shown in Fig. 4.11. The reconstruction of the Rössler attractor by embedding dimension of eight and time length of 5000 is still not completely matched with that of the original attractor. But with increasing the number of the points used for reconstruction, this discrepancy disappears. For embedding dimension of eight and time length of 20000 points, the Rényi dimensions match with a precision of ± 0.001 . We can observe that we need more data points for a reconstructed attractor to reach the same dimensions that the original attractor gives with less points.

4.2.2 False Nearest Neighbourhood Method for the Best Embedding Dimension

The method of the false nearest neighbourhoods proposed by Kennel *et al.* also deals with determining the best embedding dimension of an experimental series [KeBA92]. This method directly addresses the topological issue of the embedding process.

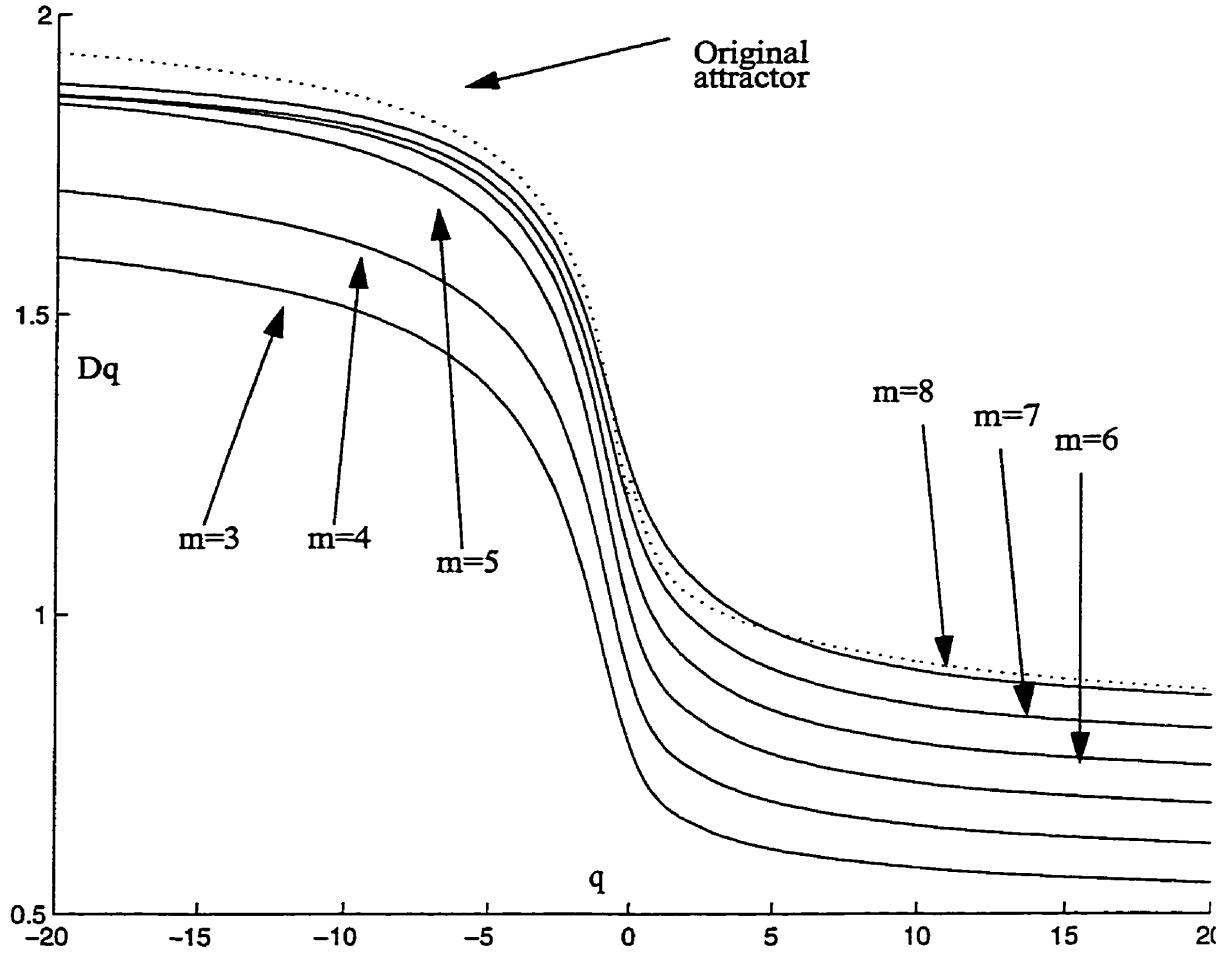

Fig. 4.11. The convergence of the reconstruction of the Rössler attractor with increasing embedding dimension. The dot-curve shows the Rényi dimensions of the original attractor. The Rényi dimensions are calculated using 5000 points of the attractor trajectory with lag=20 and hypercube sizes of 0.001 to 512 and the linear region is between hypercubes of size 0.5 to 64.

This procedure identifies the number of false nearest neighbours, i.e. the points that appear to be the nearest neighbours because the embedding space is too small. When the number of false nearest neighbours drop to zero we have an unfolded or embedded attractor in an m-dimensional Euclidean space.

The basic idea is that in the passage from dimension n to $n+1$ one can differentiate between points on the orbit that are true neighbours and points that are false neighbours. A false neighbour is a point in a data set that is a neighbour solely because we are viewing the orbit in too small an embedding space. When we have achieved a large enough embedding space all neighbours of every orbit pointed in the multivariate phase space will be true neighbours. In an embedding dimension that is too small to unfold the attractor, not all points that lie close to one another will be neighbours because of the dynamics. Some will actually be far from each other and simply appear as neighbours because the geometric structure of the attractor has been projected down onto a smaller space.

If we are in n-dimensions, working with points of an attractor reconstructed from time series x and the rth nearest neighbour of each point $\bar{y}_i$ of the reconstructed attractor is denoted by $\bar{y}_i^{(r)}$ then

$$R_n^2(i,r) = \sum_{k=0}^{n-1} \left[x(i+k\tau) - x^{(r)}(i+k\tau)\right]^2 \tag{4.9}$$

is the square of the Euclidean distance between point $\bar{y}_i$ and this neighbour and τ is the lag.

In going from dimension n to $n+1$ we just add a $n+1$ coordinate to the summation

$$R_{n+1}^2(i,r) = R_n^2(i,r) + \left[x(i+n\tau) - x^{(r)}(i+n\tau)\right]^2 \tag{4.10}$$

A natural criterion for false neighbours is that the increase in distance between $\bar{y}_i$ and $\bar{y}_i^{(r)}$ is large when going from n to $n+1$. The criterion is defined as

$$\left[\frac{R_{n+1}^2(i,r)-R_n^2(i,r)}{R_n^2(i,r)}\right]^{0.5} = \frac{\left|\left[x(i+n\tau)-x^{(r)}(i+n\tau)\right]\right|}{R_n^2(i,r)} > R_{tol} \tag{4.11}$$

where R_{tol} is a threshold. R_{tol} is found by numerical experimentation, that is by fixing the embedding dimension and testing the sensitivity of different values of R_{tol}. It is sufficient to consider only nearest neighbours $r = 1$ and interrogate every point on the attractor to establish how many of the nearest neighbours are false.

But this criterion by itself is not sufficient since the experiments show that even though $\bar{y}_i^{(1)}$ is the nearest neighbour of $\bar{y}_i$ it is not necessarily close to $\bar{y}_i$, therefore an additional criterion is proposed by Kennel *et al.* as

$$\frac{R_{n+1}(i,1)}{R_A} > A_{tol} \tag{4.12}$$

where they suggest

$$R_A^2 = \frac{1}{N}\sum_{i=1}^{N}[x_i-\bar{x}]^2 \tag{4.13}$$

$\bar{x}$ being the mean of the series. This criterion discards those nearest neighbours which lie in the extremities of the attractor. This happens when we try to uniformly populate an object in n dimensions with a fixed number of points, since the fixed number of points move further and further as n increases. Now a nearest neighbour which fails either of the tests is declared false.

Figure 4.12 shows the result of calculation of the percentage of false nearest neighbours for the Hénon attractor with R_A=2, A_{tol}=2 and R_{tol} from 1 to 20. For R_{tol}=18 the percentage of nearest neighbours falls below 0.5% for embedding dimensions greater than

four. The disadvantage of the false nearest neighbourhood method is the lack of a precise way of determining the embedding dimension and its dependency on the value of R_{tol}. But this method is able to identify between chaos and random noise. In this thesis we use this method for determining the existence of low dimensional attractors. Figure 4.13 shows the calculation of the false nearest neighbourhoods percentage for white noise generated by a random number generator with uniform distribution.

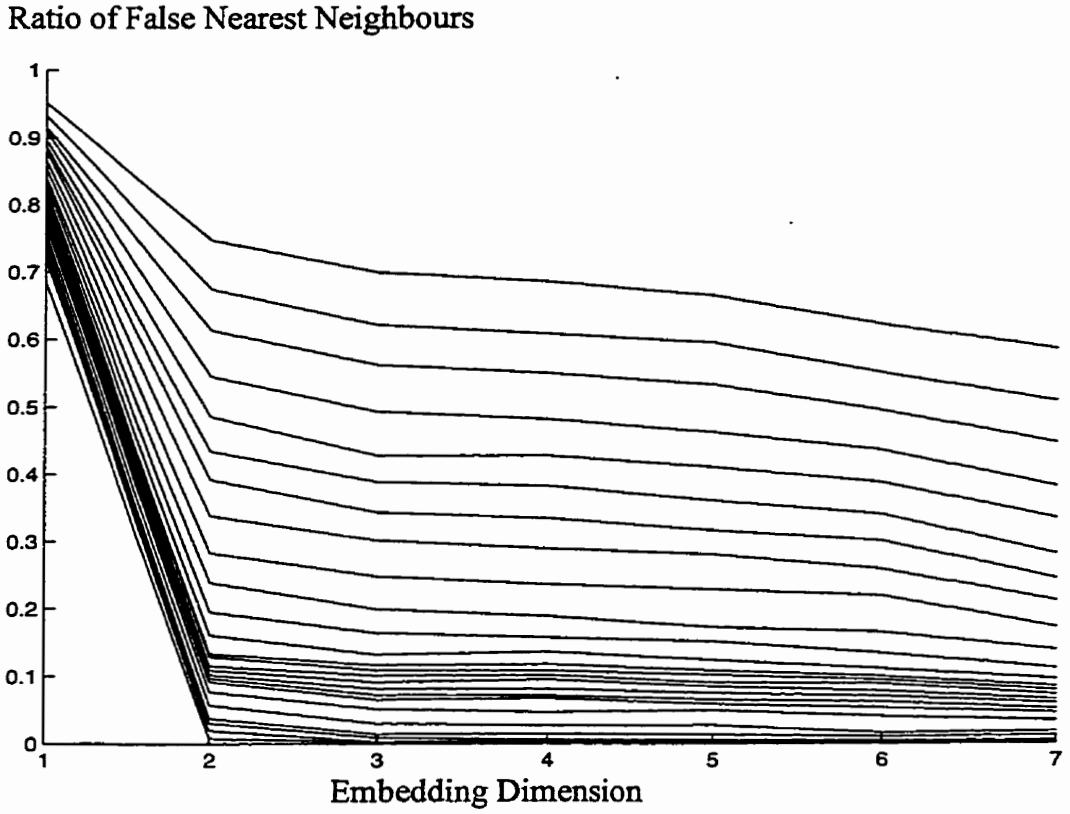

Fig. 4.12. Ratio of false nearest neighbourhoods for the Hénon attractor for embedding dimensions one to seven.

We see that for the embedding dimension of one to seven that there is no decrease in the percentage of false nearest neighbours for white noise. An experimental range of R_{tol} is chosen considering the maximum and minimum increases in the distances between the

nearest neighbour points. The result of the experiment with white noise shows that for embedding dimensions in the range of one to seven, no stable structure emerges for white noise.

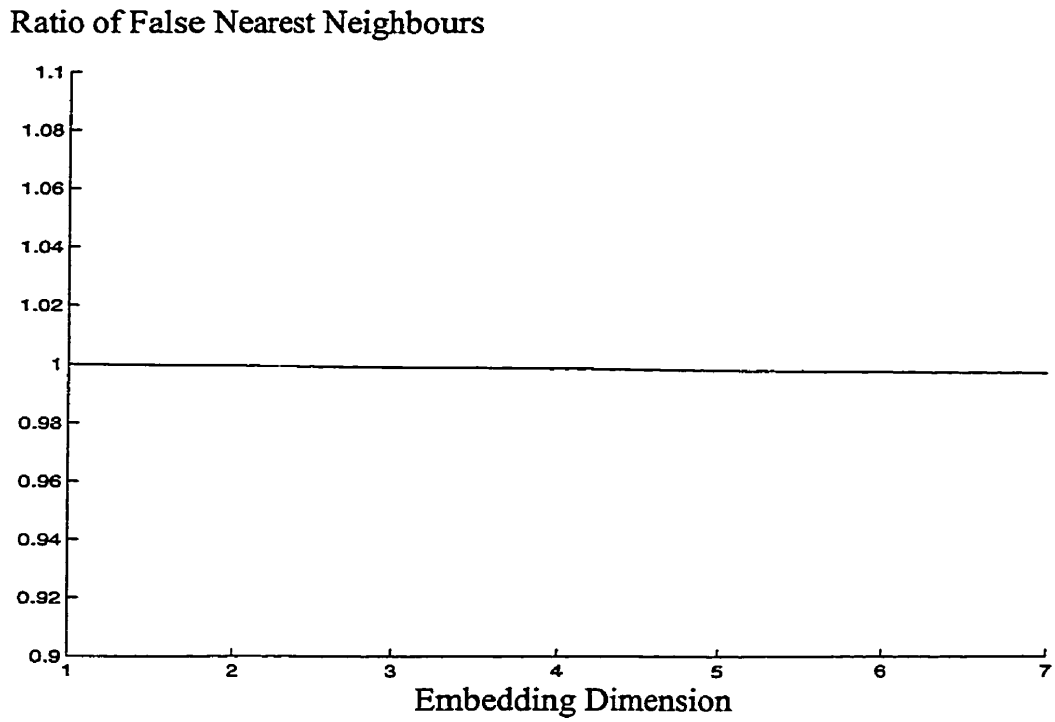

Fig. 4.13. The ratio of false nearest neighbours do not reduce with higher embedding dimensions for white noise.

4.2.3 Methods for Choosing the Best Lag for the Reconstruction of the Attractors

Different methods have been reported in the literature for calculation of the best lag for the reconstruction of the attractors. In the past section we chose the lag by simply considering the successively larger values of the lag, τ, and then visually inspecting the phase portrait of the resulting attractor. This method will only produce reasonable results for systems of relatively simple structures. In this section we will present the two methods

which are mostly used in the literature. The autocorrelation function method looks into the linear dependence of two variables while the minimum mutual information criterion looks into the general dependence of two variables. The following methods are used in the following chapters for the estimation of the best lag in the reconstructions.

4.2.3.1 The Autocorrelation Function

The covariance function, C, compares two data points in the time series separated by the lag τ and for a time series of length N is calculated as

$$C = \frac{\sum_{i=1}^{N-\tau} (x'_i)\,(x'_{i+\tau})}{\sum_{i=1}^{N-\tau} (x'_i)^2} \tag{4.14}$$

$$x'_i = x_i - \bar{x}_i \tag{4.15}$$

where $\bar{x}_i$ is the mean of the temporal signal. The lag of the reconstruction is then taken as a specific ratio of C. Among the most popular of these thresholds are: the value of τ which first gives C equal to one half, the value of τ which first gives the C equal to zero, and the value of τ which first drops below $1 - \frac{1}{e}$ of the first value of C. It is important to point out the values calculated by these methods are not consistent for reconstructions by different variables of a system [RoCD93][Addi97].

4.2.3.2 The Minimum Mutual Information Criterion

The mutual information of the attractor reconstruction coordinates is defined as

$$M = \sum_{i=1}^{N-\tau(m-1)} P(x_i, x_{i+\tau}, x_{i+2\tau} \cdots x_{i+\tau(m-1)}) \log\left(\frac{P(x_i, x_{i+\tau}, x_{i+2\tau} \cdots x_{i+\tau(m-1)})}{P(x_i) P(x_{i+\tau}) P(x_{i+2\tau}) \cdots P(x_{i+\tau(m-1)})} \right) \tag{4.16}$$

where $P(x_i)$ is the probability of the occurrence of the time series variable x_i, $P(x_i, x_{i+\tau}, x_{i+2\tau} \cdots x_{i+\tau(m-1)})$ is the joint probability of occurrence of the attractor coordinates $X_i = (x_i, x_{i+\tau}, x_{i+2\tau} \cdots x_{i+\tau(m-1)})$,and m is the embedding dimension. M is a measure of the statistical dependence of the reconstruction variables on each other. If the coordinates are statistically independent then

$$P(x_i, x_{i+\tau}, x_{i+2\tau} \cdots x_{i+\tau(m-1)}) = P(x_i) P(x_{i+\tau}) P(x_{i+2\tau}) \cdots P(x_{i+\tau(m-1)}) \tag{4.17}$$

and so, M=0. M is zero for completely random processes, such as white noise. The mutual information is a measure of general independence of two or more variables, therefore, it provides a better criterion for the choice of lag in comparison to the autocorrelation function, which is only a measure of linear dependence of the variables [FrSw86][Fras89]. In this thesis, we use the first local minimum of the mutual information of a two dimensional attractor reconstruction for determining a suitable delay for higher dimension reconstructions. For practical implementation of the minimum mutual information criterion a two-dimensional reconstruction of an attractor in x_i and $x_{i+\tau}$ plane is considered. The plane is then partitioned into N_c columns and N_r rows. The

mutual information is calculated as

$$M_2 = \sum_{k=1}^{N_c} \sum_{l=1}^{N_r} P(k, l) \log\left[\frac{P(k, l)}{P(k) P(l)}\right] \tag{4.18}$$

where $P(k)$ and $P(l)$ are the probability of the occurrence of the attractor in column k and row l respectively. $P(k, l)$ is the joint probability of the attractor lying in the column k and row l grid box. The function $M_2(\tau)$ is plotted and the best lag is chosen as the first minimum of this function. $M_2(\tau)$ shows that for a certain lag τ, how much information does a measurement of point x_i give about a measurement of $x_{i+\tau}$, or in other words it evaluates how redundant is the $x_{i+\tau}$ axis of the phase portrait [FrSw86][Fras89].

The drawback of this method is the dependency of the estimate on the grid boxes. For a fixed number of data, larger boxes have more points, hence the estimate of the average probability is more accurate, but, on the other hand, estimates of $P(k, l)$ are too flat. Smaller boxes allow the fluctuations due to noise to be interpreted as small scale structure [FrSw85]. Figure 4.14 shows the results of calculation of autocorrelation function and mutual information for the Lorenz attractor.

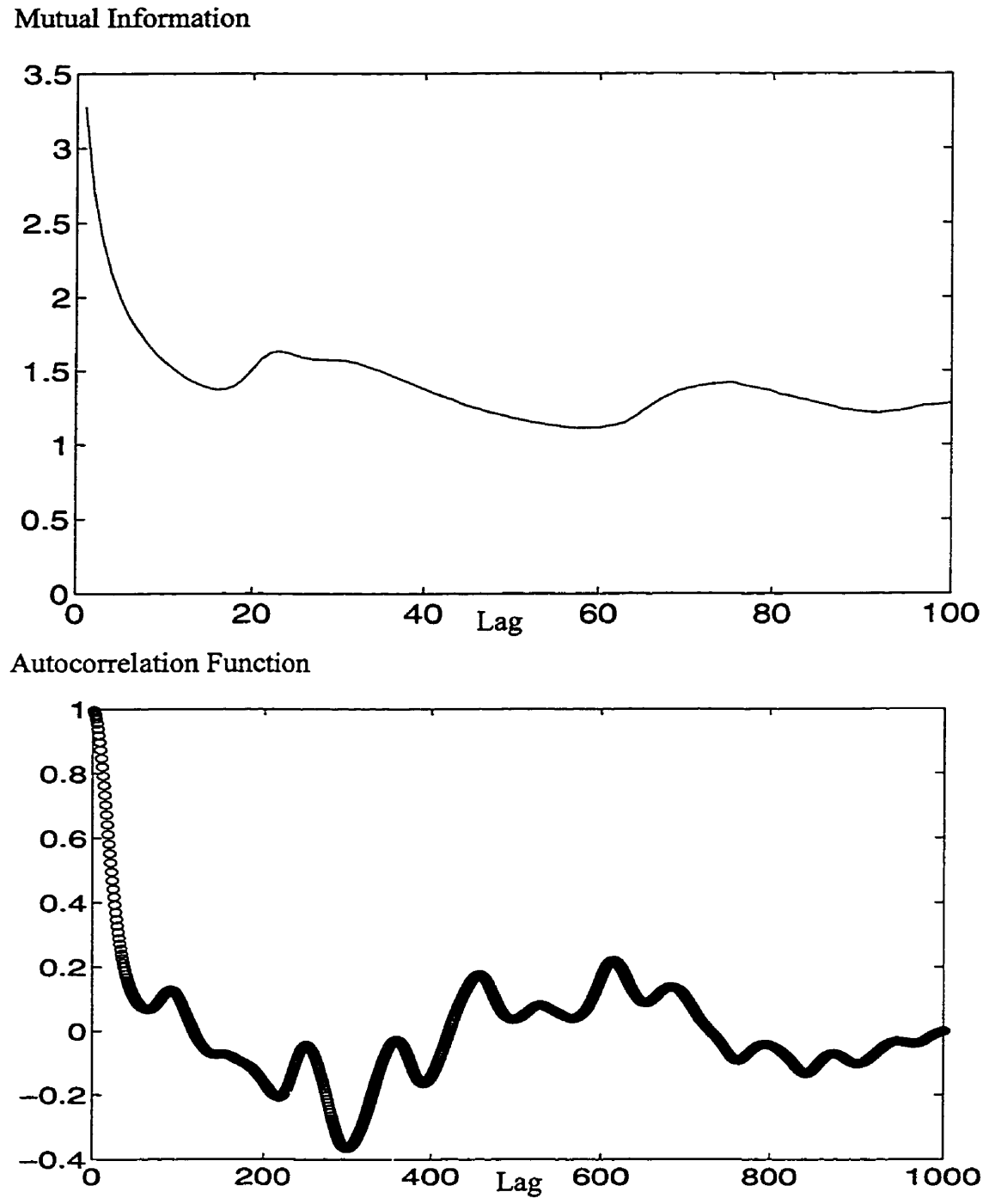

Fig. 4.14. The mutual information function and the autocorrelation function of the Lorenz attractor. The first local minima of the mutual information function suggests a smaller lag in comparison to the zero crossing of the autocorrelation function.

4.3 Distinguishing Non-Chaotic Series

Distinguishing deterministic chaos from noise is an important problem. Effective algorithms for detecting chaos must accurately characterize both chaotic and non-chaotic systems. In this section we further establish the utility of our approach by examining its performance with the following non-chaotic signals: a quasi-periodic deterministic system created by superposition of two sinusoidals with two different frequencies

$$x(i) = \sin(2\pi F_1 i\Delta t) + \sin(2\pi F_2 i\Delta t) \tag{4.15}$$

where $F_1 = \sqrt{3}Hz$, $F_2 = \sqrt{5}Hz$, and $\Delta t = 0{:}01$ sec.

The second signal is white noise generated by a random number generator with uniform distribution. Each system was treated as the output of a blackbox system.

The best lag for reconstruction of the attractor assumed for the sinusoidal is chosen as τ=8 where the two dimensional orbit opens up. Then the attractor was reconstructed in a two dimensional embedding space. The result of the log-log plot and the D_q curve of the sinusoidal is shown in Fig. 4.15. The D_q curve of a sinusoidal is a flat curve of dimension one. Increasing the embedding dimension to three or four yields the same results. Since the deterministic system is not a chaotic one, all the fractal dimensions are equal to the Euclidean dimension of the sine curve.

The best lag for reconstruction of the attractor assumed for the white noise was chosen as τ=1 since for no increase in the value of τ, the two dimensional phase space appears to form any structure in the distribution of the points in the space (Fig. 4.16). The attractor was reconstructed in embedding spaces of 3, 4, 5, 7,15, and 20 dimensions. The result of the D_q curves always yield an S-curved shape if enough points are generated to

fill the higher dimensional spaces, but no convergence is apparent up to the embedding dimension of 20. This is shown in Fig. 4.17. The finite dimensional system exhibit a convergence once the embedding dimension is large enough to accommodate the dynamics, whereas the stochastic systems fail to show a convergence because they appear to be more ordered in higher and higher embedding spaces. Strictly speaking, we can only distinguish high dimensional systems from low dimensional ones, although in most applications a high dimensional system may be considered random, i.e., infinite dimensional [RoCD93].

The calculation of dimensions gives an estimate of the system complexity and entropies and the distinction of chaos from randomness through the calculation of dimensions is in fact based upon the comparison of the low dimensional fractal structure of strange attractors arising from a chaotic system with high dimensional semi-structures arising from random noise.

In Section 4.2.2, we also saw that the false nearest neighbours method can distinguish between random noise and chaos. This method in fact recognizes the stable structures of the strange attractors from the non-stable structures of noise.

It is important to note that another path exists for achieving the same purpose and that is the calculation of the Lyapunov exponents of the experimental data and estimating the level of chaos or sensitivity to initial conditions in the dynamical system. A detailed study of this method is found in [WSSV85]EKRC86][RoCD93].

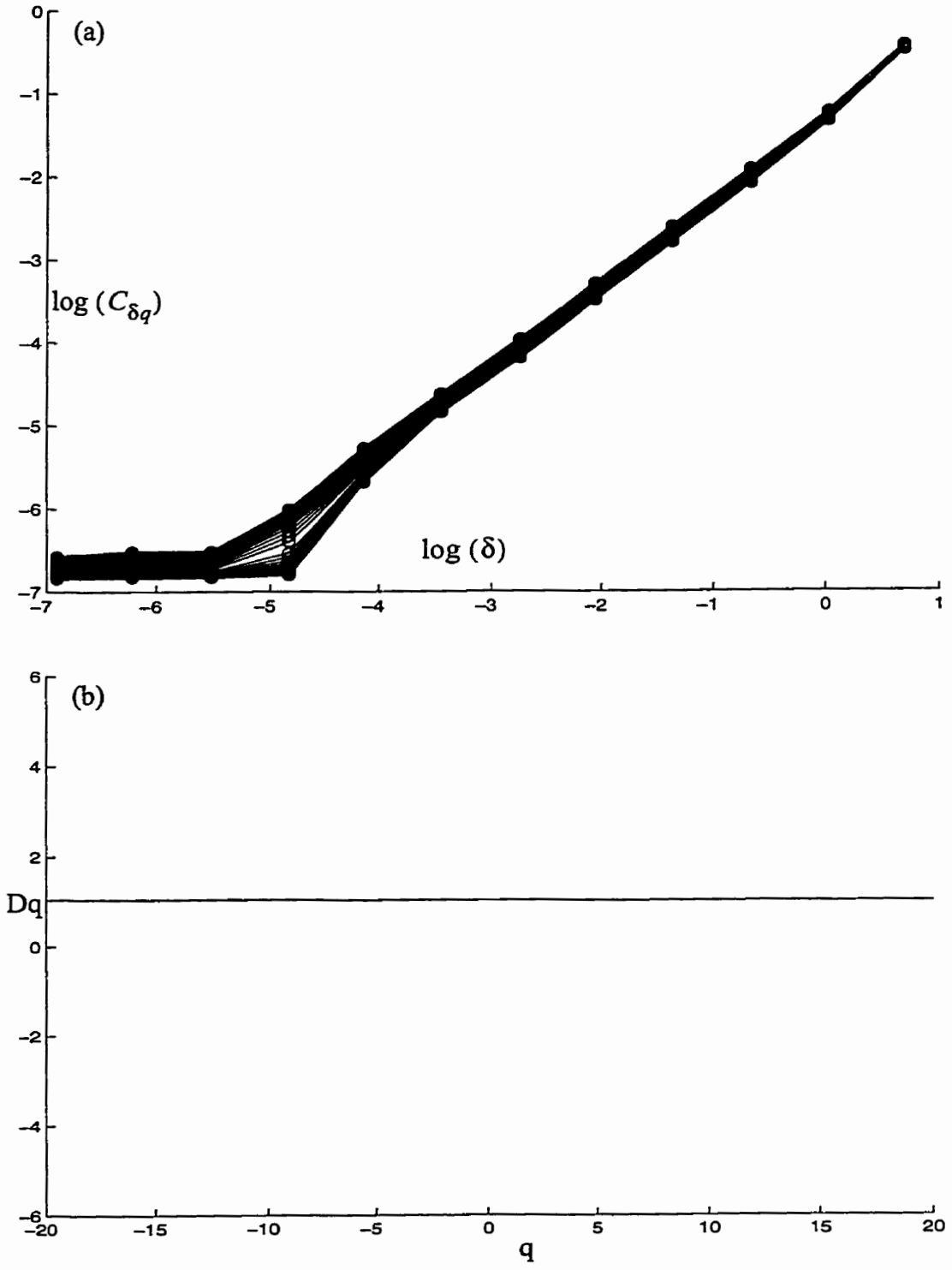

Fig. 4.15. (a) The log-log plot of a two-periodic sinusoidal. (b) The Dq curve of the sinusoidal.

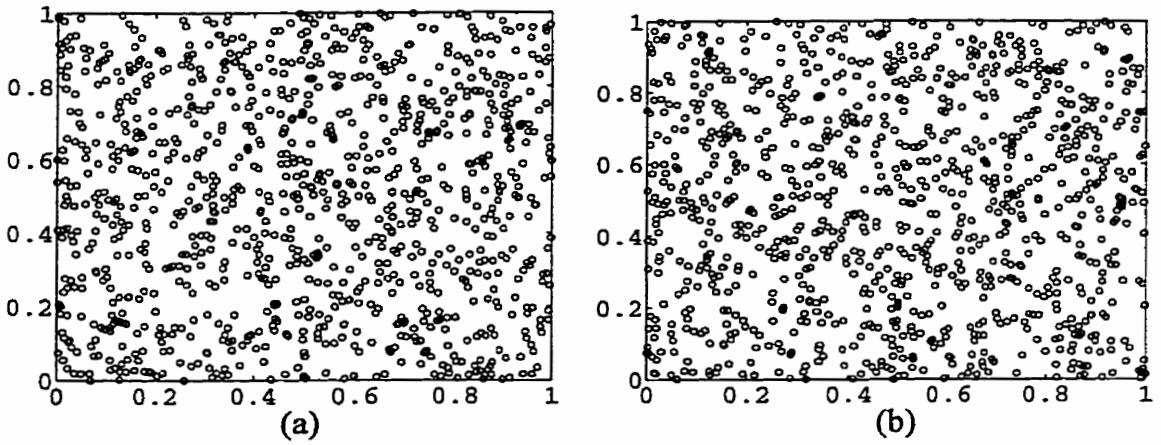

Fig. 4.16. White noise generated by a random number generator. The time series is delayed against itself with $\tau=1$ in (a) and with $\tau=10$ for (b).

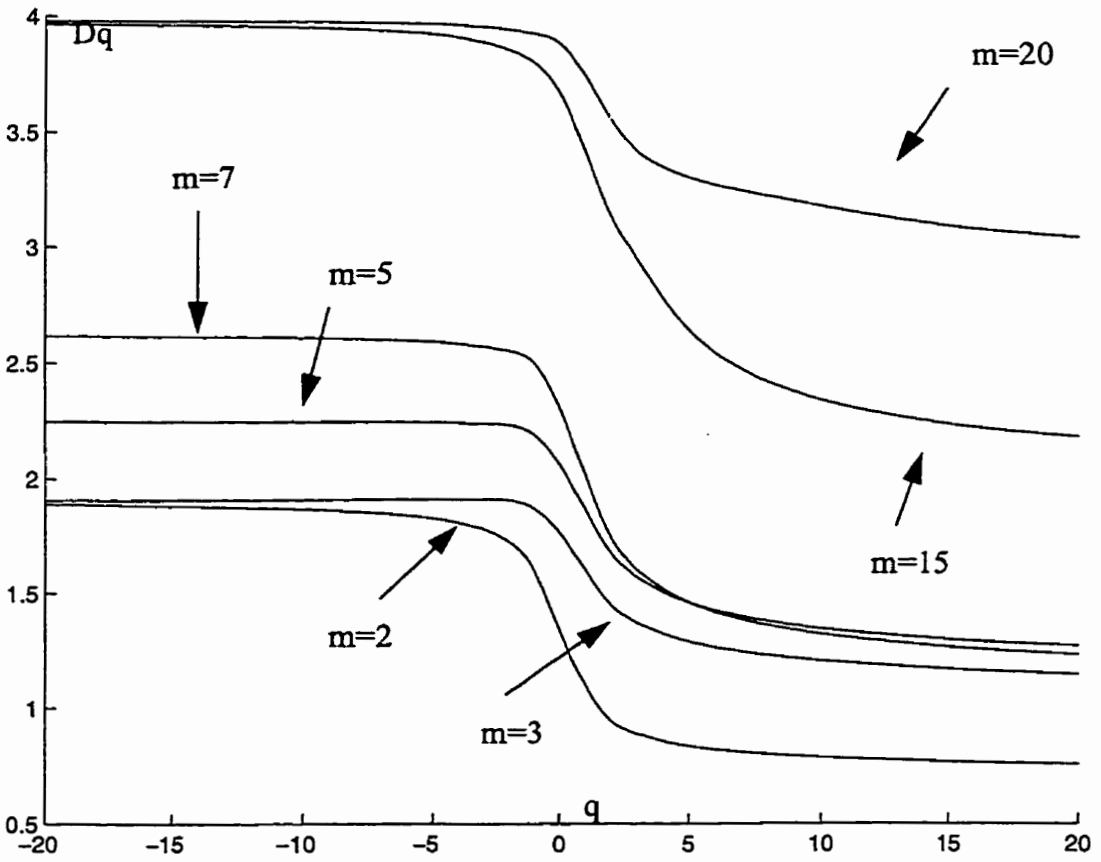

Fig. 4.17. The Dq curves of the white noise do not converge with increasing embedding dimension.The embedding dimension, m, of each curve is stated.

In this method, the trajectories of nearby initial conditions on an attractor is studied. If the dynamics are chaotic then the trajectories diverge, on average, at an exponential rate characterized by the largest Lyapunov exponent. The largest Lyapunov exponent is also estimated as the mean rate of separation of the nearest neighbours. Divergence and convergence of the attractor in all orthogonal directions of the phase space is characterized by a spectrum of Lyapunov exponents. A chaotic attractor has at least one finite, positive Lyapunov exponent. Random data has an infinite, positive Lyapunov exponent, while periodic attractors have only zero and negative exponents.

4.4 Summary

In this chapter, we presented the embedding theorem for the reconstruction of strange attractors. We described the methods for distinguishing between random noise and chaos in experimental time series, reviewed the methods for determining the best embedding dimension and the best lag for reconstruction of the attractors, and explained further the method of correlation integral for calculation of the Rényi dimensions of an attractor. In the next chapter, we will report on the implementation of the methods presented in this chapter on EMG signals and the experiments designed for evaluation of the fractal characterization of EMG signals.

CHAPTER V

MULTIFRACTAL ANALYSIS OF THE EMG SIGNALS

In this chapter, we want to use the results of the discussions in the previous chapters, and attempt to perform a multifractal characterization of the EMG signals. Our primary goal is to examine the EMG for chaos. We shall see that EMG is indeed arising from a low dimensional strange attractor. The reconstruction of this strange attractor requires a thorough analysis of the embedding dimension and the best lag of reconstruction. The implementation of the correlation integral and calculation of the Rényi dimensions follows.

Although the primary focus in this thesis is on the correct and meaningful calculation of the multifractal characterization of the EMG signals, we need to reach this objective in the context of a specific experiment. For this purpose, we attack one of the problems in electromyography which has been dealt with since the fifties and has not been completely solved yet. Is it possible to characterize the EMG signals recorded from a single muscle in different functionalities? In other words, is it possible to identify the functionality of a single muscle by the EMG characteristics?

In this chapter, we propose an experiment to study this problem and investigate the capability of the Rényi dimensions of the signals to perform this identification. In the first section we explain this experiment and its objective. In the second section we examine the signals acquired in this experiment for the presence of a low dimensional attractor in the reconstructed phase spaces. The false nearest neighbourhood is used for this purpose. The results of the minimum mutual information criterion are used to estimate the best lag for the reconstruction. We perform the multifractal dimension characterization of the

attractors using the generalized correlation integral. The best embedding dimension is chosen by studying the convergence of the multifractal dimensions. The convergence rate of the multifractal dimensions with the chosen time length and sampling rate of the experimental EMG signals is examined. The effect of the noise levels in the different stages of these calculations is also discussed.

5.1 Objectives of the Experiments

In the last section of Chapter 2, we talked about the different factors influencing the order of the motor unit recruitment. The results of experiments of several researchers show that recruitment order can vary if the same muscle is used for different purposes. Schmidt & Thomas [ScTh81] have reported that in the *extensor digitorum communis*, the recruitment order will depend on which of the four fingers is to be extended. Gielen and Denier van der Gon [GiDe90] have reported that in biceps brachii, the threshold of a motor unit depends on whether the muscle is being used to flex the elbow, supinate the forearm, or externally rotate humerus. Hennemen *et al.* [HeSY76] have stated that when the same motor task is undertaken in exactly the same way, the order in which the motor units are recruited remains fixed. In this thesis we present an experiment in which we attempt to discriminate among the EMG signals recorded from deltoid and trapezius muscles, in three different functionalities of shoulder abduction, flexion, and extension. We use the multifractal characteristics of the signals for classification. If the order of the motor unit recruitment follows unique patterns for each of the three movements, there should be certain characteristics of the EMG signal which fingerprint them. In these experiments the objective is to find out if the multifractal dimensions of the EMG signals are capable of recognizing three different functionalities of deltoid and trapezius muscles.

It is important to note that the idea of using the signature of EMG signals for discriminating between several limb functions was proposed in the early sixties with the motivation of using the discriminatory methods for the control of artificial limbs. The dominant approach used for discrimination of signals in artificial limbs proposed by Graupe *et al.* [GrSZ85] uses a time series identification process, i.e. a time domain autoregressive signature model. Graupe's approach is specifically designed for an optimal performance of an artificial limb and is based upon using electrode sites with heavy cross talk from several muscles involved in a certain function. Therefore, the results of discrimination in Graup's approach are not comparable with the approach presented in this thesis.

The experimental goal is to find unique signatures for EMG signals recorded from certain muscle functionalities. But it is desired to prove that the discrimination is in fact due to a real difference in the underlying physiological phenomenon in different functionalities of a single muscle, therefore special care is taken to eliminate other possible factors such as cross talk between muscles.

The most important factors influencing the shape of the EMG signal recorded by a surface electrode, with fixed area and shape of electrode surfaces and a fixed distance between the electrodes, are listed below:

1. The number of detected active motor units in the detection volume;
2. The firing rate of the motor units in the detection volume;
3. The fibre type composition of the active detected fibres;
4. The fibre diameters of the active detected fibres;
5. The depth and location of active detected fibres;

6. The conduction velocity of the active detected muscle fibres;

7. The amount of cross talk at the detection volume; and

8. The amount of fatty tissue between the active detected fibres and the electrodes.

The first six factors can be varied by a relative movement of the electrode location and the active fibres, which may bring a new set of active fibres within the detection range and removing some from it. This may be caused because of the fixation of the electrodes to the skin surface which does not change length in concert with the contracting muscle fibres. These factors can also be caused by the rotation of active motor units in the detection volume, rather than the change of the detection volume.

In this experiment, one must show that the discrimination is not influenced by the change in the location of the electrodes; i.e. the change of the detection volume. Therefore, the electrode location is fixed when recording from one muscle in three different shoulder movements of abduction, extension, and flexion. But furthermore, it is necessary to show that the discrimination is not due to the movement of the sensors because of the contraction of the muscle in different directions which also causes the variation of the muscle/fat layer between the electrode and the active fibres.

The movement of the electrodes occurring due to the different directions of contractions are in a range of a few millimetres. In order to prove that the result is independent of this slight movement, the recordings were obtained from electrode positions which differed in a few millimetres. If a slight dislocation of the electrode has a strong influence in the value of the Rényi dimensions, then the data obtained from these experiments are not classified correctly, because the samples recorded for each class (from each function of a muscle) are a mixture of data from different electrode positions. If the

classification is still possible it can be concluded that the very slight changes of the detection volume due to the slight movements of the electrodes are not the cause of the differences among the Rényi dimensions calculated for the three different muscle functionalities. It consequently follows that the variation of the spatial filtering due to the movement of the electrodes is not also the cause of the discrimination. One can, therefore, examine if the distinctions in the levels of the complexity measures of the EMG signals in the three different functionalities stem from the physiological phenomenon or not.

The cross talk has been minimized using differential amplifyiers. The large size of the deltoid and trapezius muscles also reduces the effects of cross talk. The last concern with this experiment is the problem of the initiation and cessation time of the EMG signals recorded. How can the timing of the signals recorded in independent experiments be regulated? In our experiments, the recording of the signals is started not later than 20 seconds after the arm is held in the desired position. This delay is usually required so the signal settles down in the physical recording equipment after some disruptions due to the movement of the wires and electrodes. The length of the recorded signals is not longer than one second. There is a resting period of two minutes between each recording. According to the results of Moussavi [Mous97], this timing process eliminates the effects of fatigue in the recordings.

The objectives of the proposed experiments is summarized as follows

1. Examine the EMG signal to determine if it is a chaotic signal;
2. Establish the procedure for the multifractal characterization of EMG;
3. Examine the possibility that multifractal features of the EMG signals can discriminate the different functions of a single muscle;

4. Examine the effect of electrode dislocation in the discrimination results; and

5. Examine the effect of cross talk in the discrimination results.

5.2 Data Acquisition

For EMG recording, a multi channel bank of amplifiers with high- and low-pass filters was used with a multi channel A/D National Instrument device connected to a 586 IBM compatible computer.

The muscles under study are the middle, posterior, and anterior portions of the deltoid (MD, PD, and AD respectively) and upper part of the trapezius (UT). Since these muscles are all surface muscles, self-adhesive silver-silver chloride surface electrodes were used to record EMG signals. The skin is prepared by rubbing alcohol to reduce skin resistance and electrodes are placed on the muscle according to the electrode positioning for MD, PD, AD, and UT presented in [CrKa98] and shown in Fig. 5.1. Reference electrodes are not shown here.

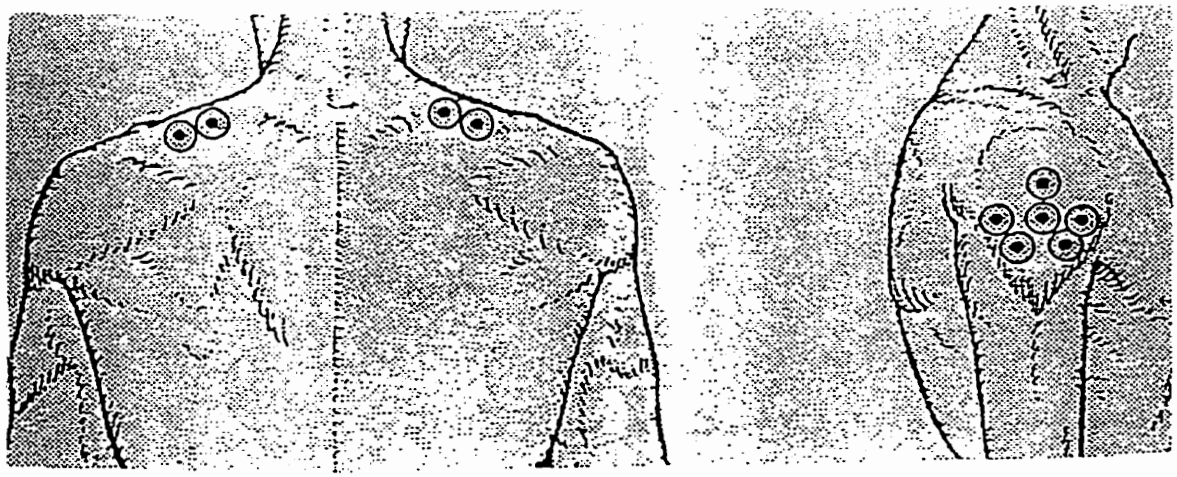

Fig. 5.1. The electrode positions in the recordings from deltoid and trapezius (from [Mous97]).

The EMG electrodes are used in a bipolar configuration. The EMG signal is amplified differentially to prevent artifacts and is filtered by a bandpass filter with 10 Hz and 1 kHz cut off frequencies. The signals are digitized at 8000 samples per second.

The following three test positions are designed for the EMG acquisition:

Position A: The subject is asked to hold her (left/right) upper limb in 60 degree shoulder abduction, 0 degree elbow flexion, 90 degree forearm pronation, and wrist neutral.

Position B: The subject is asked to hold her (left/right) upper limb in 60 degree shoulder extension, 0 degree elbow flexion, and 90 degree forearm pronation, and wrist neutral.

Position C: The subject is asked to hold her (left/right) upper limb in 60 degree shoulder flexion, 0 degree elbow flexion, and 90 degree forearm pronation, and wrist neutral.

For each muscle under study, the electrodes are fixed on the muscle and then the subject is asked to perform each of the three test positions sequentially. The signal is amplified and recorded at each position. Then a two minute resting period is given and the location of the electrodes are moved within a range of a few millimeters. This sequence is repeated for each muscle 20 times. The amplification of the signals change from one subject to another, and also from one muscle to another. But the amplification remains the same for the recordings of one muscle in the three different test positions.

The length of the recordings is one second. The EMG signal of an isometric contraction recorded for one second can be considered as stationary [Mous97]. Four subjects of the ages between 20 to 30 years participated in the experiments. None of the subjects had any detected abnormality in the muscle.

5.3 Characterization of the EMG Signals with the Rényi Dimensions

Having explained the different test positions and the physical recording set up of the experiments, we now proceed to discuss the characterization of the signals. The data is organized in four sets, one set for each subject under study. Each individual's set contains four groups of data corresponding to the recordings made from middle deltoid, posterior deltoid, anterior deltoid, and trapezius. Each of these groups contain three classes of data samples for abduction, extension, and flexion. Under each class there are 12 data samples which are the one-second length time signals recorded independently. The classification takes place on each group of the data, with the aim of discriminating among the three classes of abduction, extension, and flexion.

In this section the characterization method for a sample data, a one second EMG signal recorded from the middle deltoid of one of the subjects during abduction is discussed. The characterization procedure explained is the same for all data samples. The general comparison of the results is given in the next chapter.

5.3.1 Normalization of the Data

The multifractal dimension calculation is performed on unnormalized data. In the last section it was mentioned that the amplification of the signal does not vary for the recordings made from the three functionalities of each muscle. Therefore, in the classification stage, the data samples of three classes in each group are amplified equally. For this reason, there is no normalization required for the signals in each classification experiment. Furthermore, there is no normalization required for the Rényi dimension calculations.

5.3.2 Choosing the Best Lag

Both the autocorrelation and the minimum mutual information method are used to find the best lag for the reconstruction of the strange attractors of EMG signals. Fig. 5.2, shows the result of the autocorrelation calculation on the sample EMG signal.

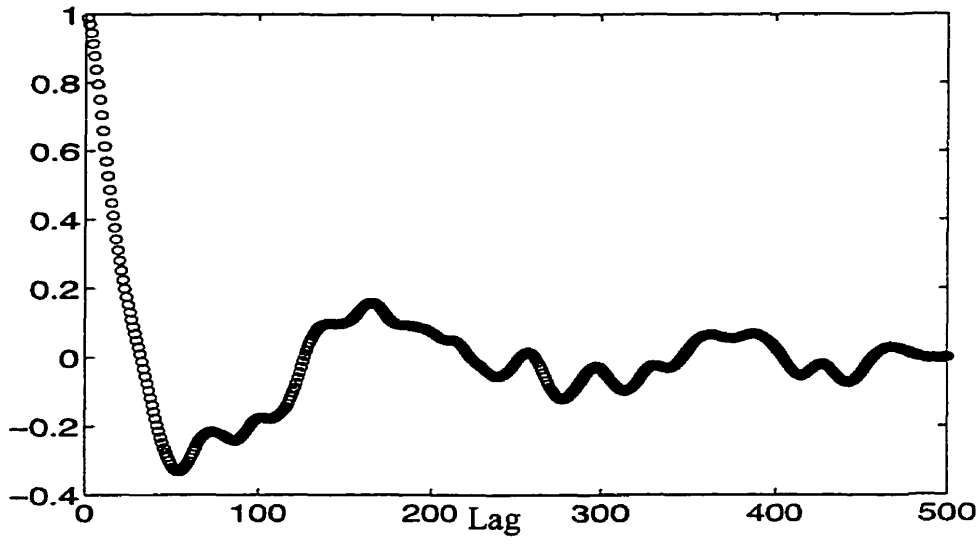

Fig. 5.2. Autocorrelation function of a sample EMG signal.

In this experiment, the autocorrelation function dropped to $1-\frac{1}{e}$ of its first value at the lag=11, and the first zero crossing happens at the lag=33. The result of the minimum mutual information calculation is shown in Fig. 5.3 for the sample EMG signal. As we explained in Section 4.2.3.2, the calculation of the minimum mutual information is dependent on the grid size used for covering the two dimensional phase space. We have performed the calculations of the minimum mutual information criterion for grid boxes 4, 8, 16, 32, and 64.

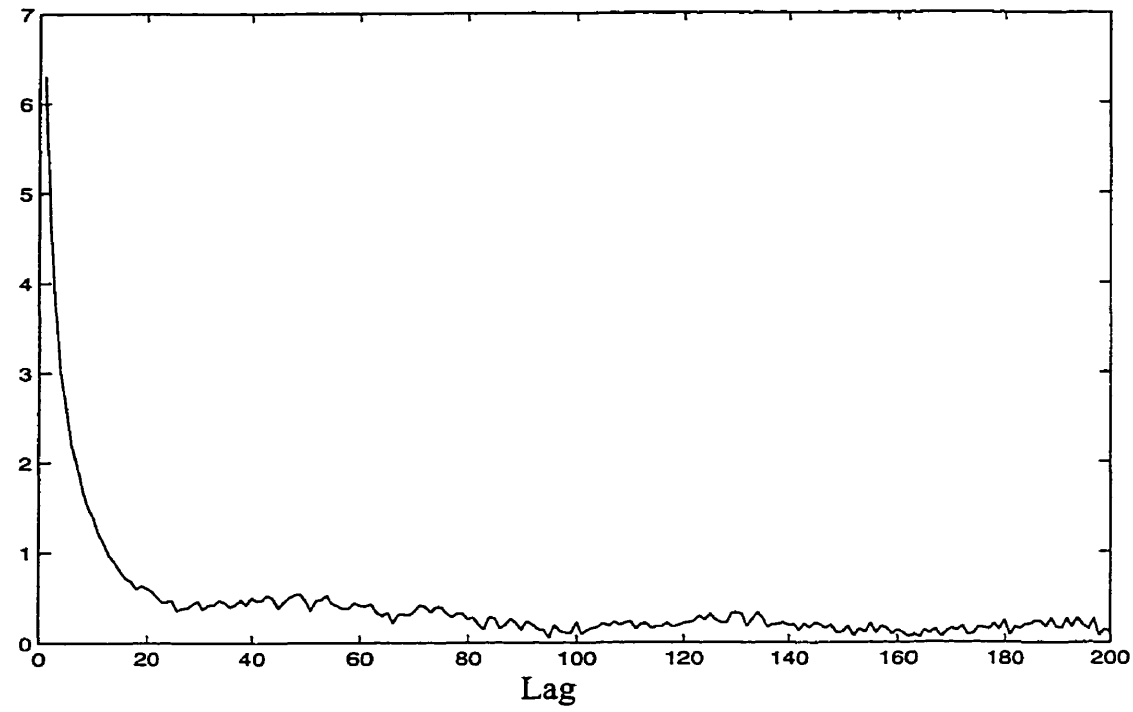

Fig. 5.3. The minimum mutual information criterion for the sample EMG signal.

The results of the experiments show that the change in the grid sizes in the calculation of the minimum mutual information criterion of the EMG signals does not effect the value of the lag where the first local minimum occurs.

The first local minimum occurs at the lag=18 for the sample signal. In all experiments, the result of the minimum mutual information criterion stays lower than the lag for which the first zero crossing of the autocorrelation function occurs. In the reconstruction of the phase spaces the result from the minimum mutual information criterion is used.

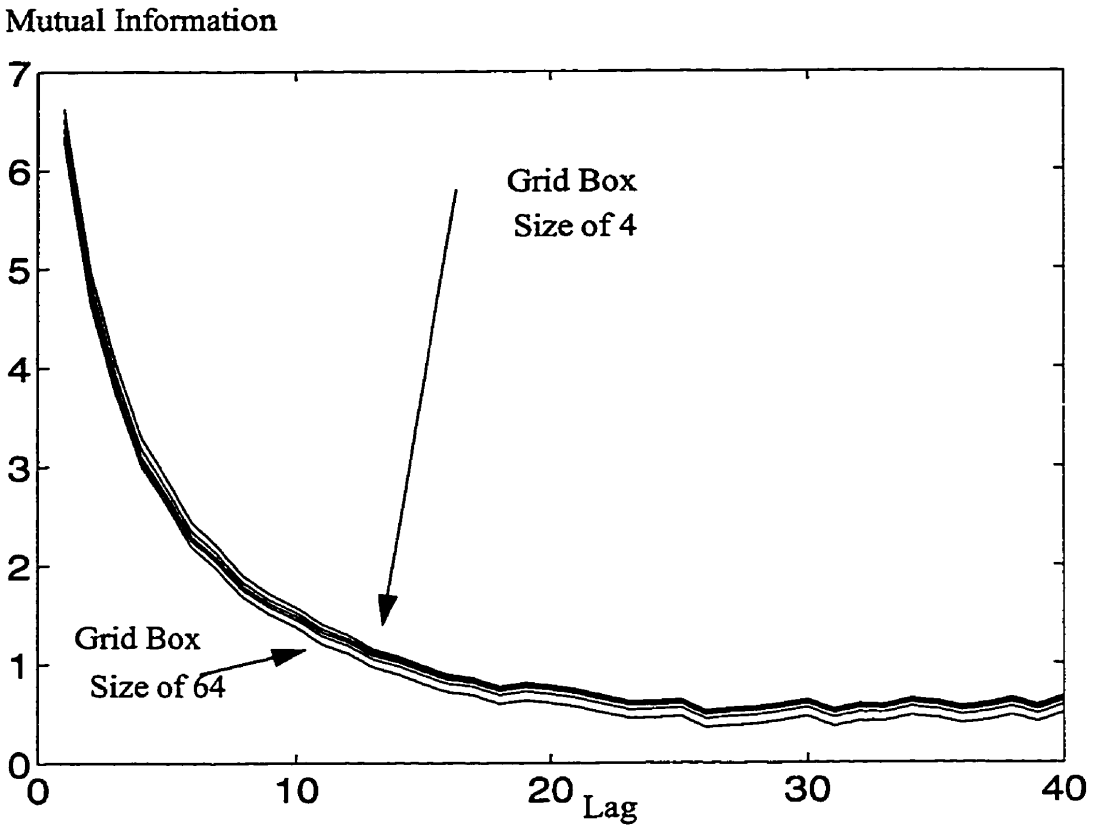

Fig. 5.4. The minimum mutual information criterion for different grid box sizes. The grid box sizes are 4, 8, 16, 32, and 64.

5.3.3 Examining the Existence of a Low Dimensional Strange Attractor

Recalling the discussion in Chapter 4 the false nearest neighbourhood method can distinguish between high dimensional noise and low dimensional strange attractors. The calculation of the percentage of the false nearest neighbours is performed on the data as explained in Chapter 4. The increase in the distances of the nearest neighbours are calculated for successively increasing embedding dimensions of 2 to 20. The parameter R_A is calculated according to Eqs. 4.12 and 4.13 with A_{tol}=2. The range of 0.5, 1, 5, 10, 15 is tested for the R_{tol} in the calculations.

The results of the calculation are plotted in Fig. 5.5 for the sample signal. The results show that for very small levels of R_{tol}, almost all of the points are classified as false nearest neighbours, but as R_{tol} approaches 10 and 15 a low embedding dimension appears. This means that there are some neighbouring points which their distances do not increase larger than a threshold set by R_{tol}. This set of nearest neighbours represent the unfolded trajectory of the strange attractor. The parameter R_A discards those neighbours which lie on the extremeties of the phase space and is neccesary for distinguishing white noise from chaos. The experiments show that the EMG signal does in fact arise from a low dimensional strange attractor. But the exact calculation of the embedding dimension using the false nearest neighbourhood is not possible since there is no standard way of choosing the best R_{tol}. The convergence of the Rényi dimensions for is used to choose the best embedding dimension.

A very important result of the calculation of the false nearest neighbours of the experimental signals was the observation that for certain classes of signals this algorithm does not yield a low embedding dimension. These results appeared for signals with SNR values lower than 10. In fact, we could see in Chapter 4 that no low embedding dimension exists for pure noise. Therefore, it is acceptable that the effective embedding dimension degrade as the SNR ratio decreases. This happens for the signals recorded from muscles which are not highly active in the test position under study. These classes of signals are discarded from the experiments since the SNR ratio is too low, the signal is too contaminated by noise, and a low dimensional attractor is not conceivable for them.

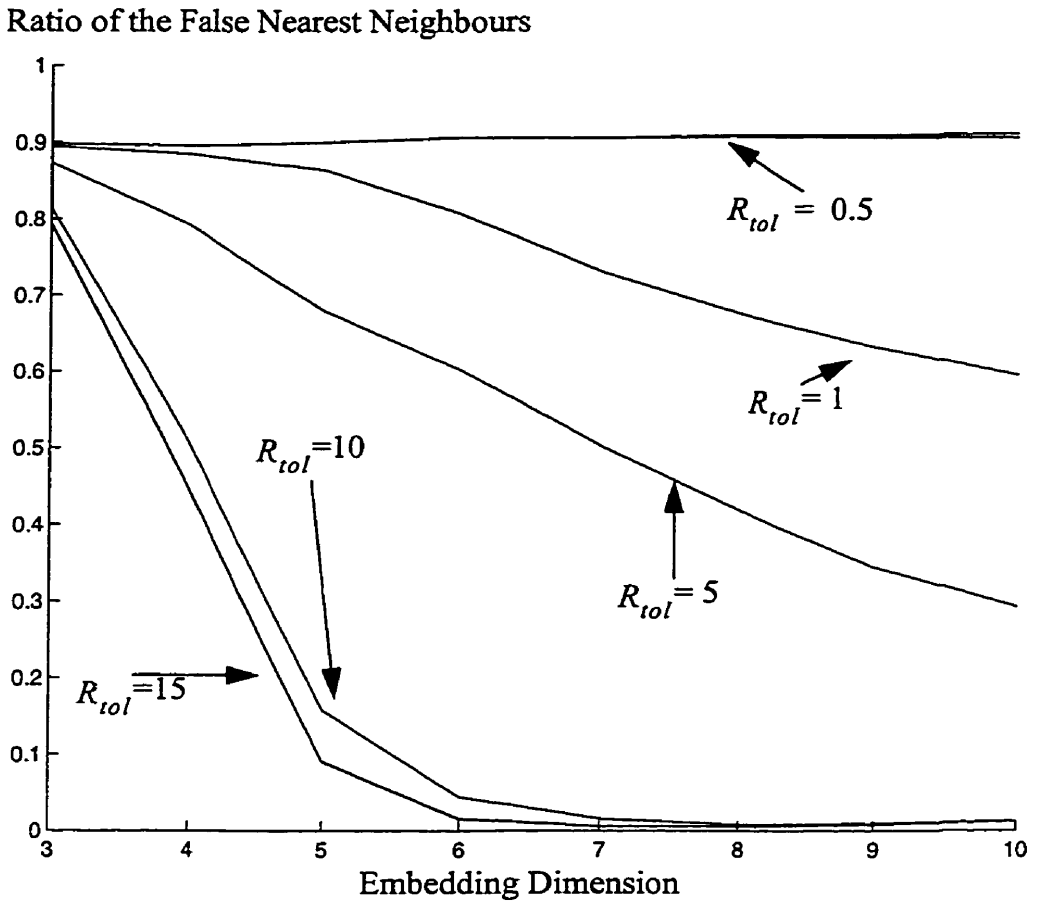

Fig. 5.5. The percentage of the false nearest neighbours in successive embedding dimensions for the sample signal. R_A=56, A_{tol}=2.

SNR	Abduction	Extension	Flexion
Middle Deltoid	28	25	12
Posterior Deltoid	20	28	4
Anterior Deltoid	20	6	26
Upper Trapezius	20	15	14

Table 5.1. The average SNR ratios for EMG signals.

The average SNR ratio for the different classes is given in Table 5.1. The averaging is among the signals recorded from all the subjects in each class. Low dimensional attractors do not appear in the range of embedding dimensions between 2 to 20 for the posterior deltoid in flexion and anterior deltoid in extension.

5.3.4 Calculation of the Rényi Dimensions and the Best Embedding Dimension

We now proceed to reconstruct the phase spaces, and calculate the spectrum of Rényi dimensions, as explained in Chapter 4, for successively increasing embedding dimensions from 2 to 10. An increasing dyadic range of hypercube sizes from 2 to 512 is used for probing the strange attractors of EMG signals produced by deltoid and trapezius muscles. This range is chosen by examining the minimum and maximum distances between the points in the reconstructed attractors. In Chapter 4, it was stated that the experiments with known strange attractors show that for SNR higher than 20 the effect of noise in the values of the Rényi dimensions, drops to a level of ± 0.001 . There are several classes in the experiments with SNR ratios between 10 and 20. These groups were not discarded from the classification, but, one needs to take this fact in consideration that the precision of the calculation of their Rényi dimensions are degraded by the effect of high noise levels.

Examining the levels of the recording channel noise, amplified with the highest gain used in the experiments, shows that the smallest valid hypercube size for estimation of the linear regressions is the hypercube size of eight. Performing the linear regression on hypercubes larger than eight minimizes the effect of noise in the calculations. The log-log plot of a sample EMG signal is shown in Fig. 5.7. It is seen that the higher saturation level occurs at approximately $\delta = 64$. Linear regression is performed on the lines between $\delta = 8$

to δ=64, since the probability estimates for hypercube sizes smaller than eight are affected by the noise levels.

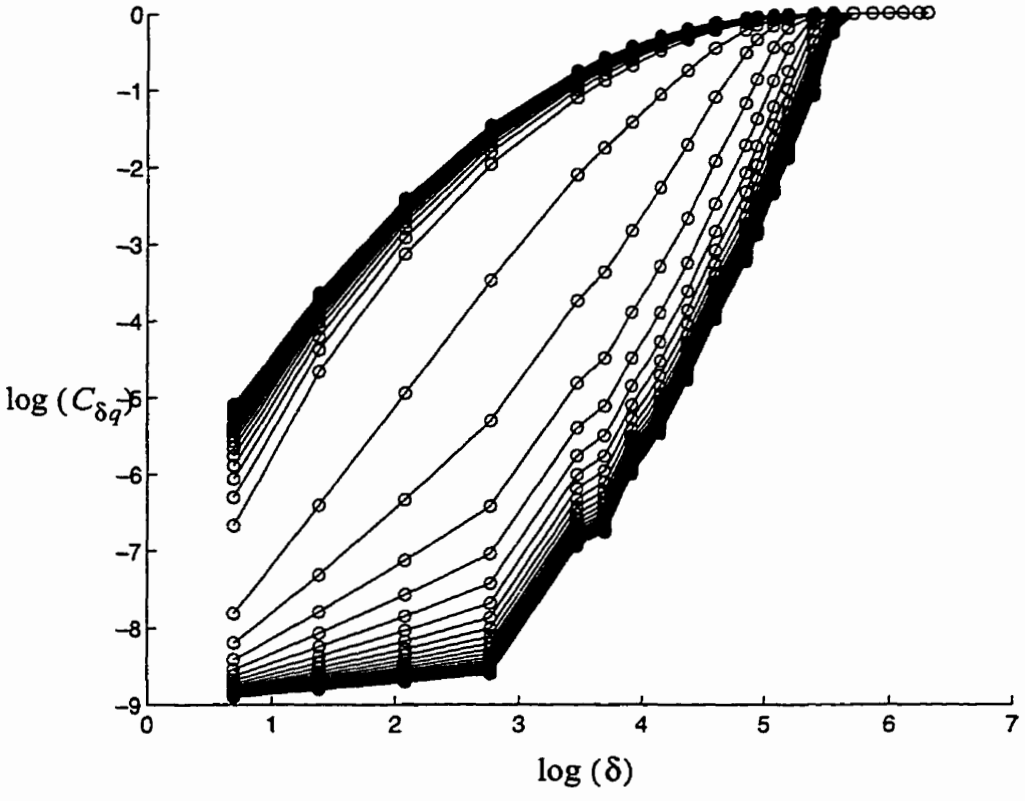

Fig. 5.7. The log-log plot of a sample EMG signal for hypercube ranges of 2 to 512. The hypercube of δ=8 is the smallest valid hypercube for linear regression due to noise levels.

The best embedding dimension is now determined by the convergence of the spectrum of Rényi dimensions. The best embedding dimension is chosen to be the dimension where the successive values of Rényi dimensions converge with a precision of ± 0.01 . The convergence of the Rényi dimensions is shown in Fig. 5.8 for the sample EMG signal.

One should realize that going to high embedding dimensions may result in a sparse

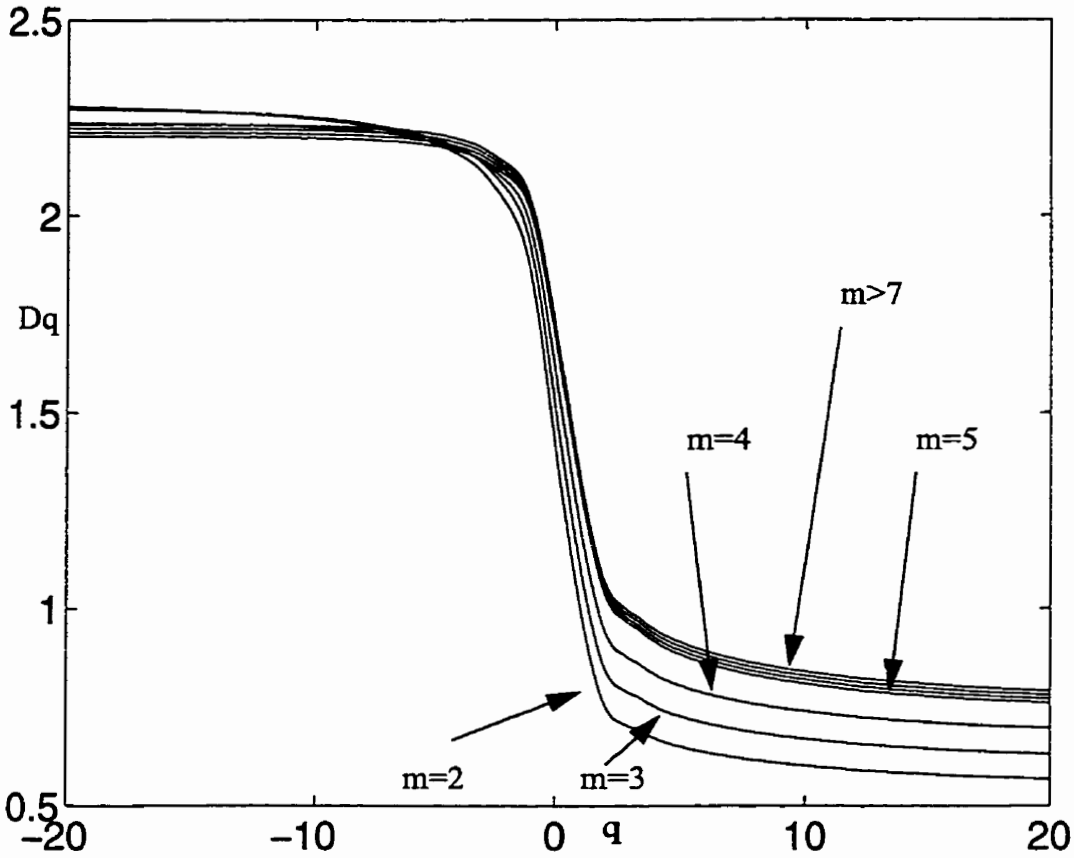

Fig. 5.8. The convergence of the Rényi dimensions for a sample EMG signal. The embedding dimension of seven and greater results in a convergence of values with a precision of ±0.01 .

phase space where the points of the trajectory are far from each other and the calculation of the multifractal dimensions is not valid. The experiments show that 8000 samples per second of the signal create enough points to result in a convergence of the multifractal values.

The multifractal dimensions for signals with fewer points were examined. The EMG signal is recorded with a fixed electrode location and with sampling rates of 1000, 2000, 3000, 4000, 5000, 6000, 7000, and 8000 samples per second, from each of the

signal classes. The multifractal dimensions are plotted. Figure 5.9 shows the results for a sample EMG signal. The positive order multifractal dimensions converge to an error range of ± 0.001, while the negative dimensions have not yet converged. The negative orders of multifractal dimensions are a representative of the smaller values of probabilities, of the attractor occurring in all the covering hypercubes. The number of points for reconstructing the attractor is limited and therefore the hypercubes corresponding to small probability values do not represent a saturated portion of the structure. Therefore, the increase in the number of points affects these probabilities more than it affects the hypercubes with bigger probabilities. This result forces the classification process to be confined to positive order multifractals calculated for the EMG signal.

5.4. Classification Method

In this thesis the distance weighted *k*-nearest-neighbour rule for classification is used. The nearest-neighbour method is a simple non-parametric classification method appropriate for problems where underlying probability distributions of the classes are not known. The algorithm is based upon the scheme proposed by Dudani [Duda76].

This decision rule assumes that observations which are close together (according to Euclidean distance metric) will have the same classification. This is also a weighting function which varies with the distance between the sample and the considered neighbour in such a manner that the value decreases with increasing sample to neighbour distance.

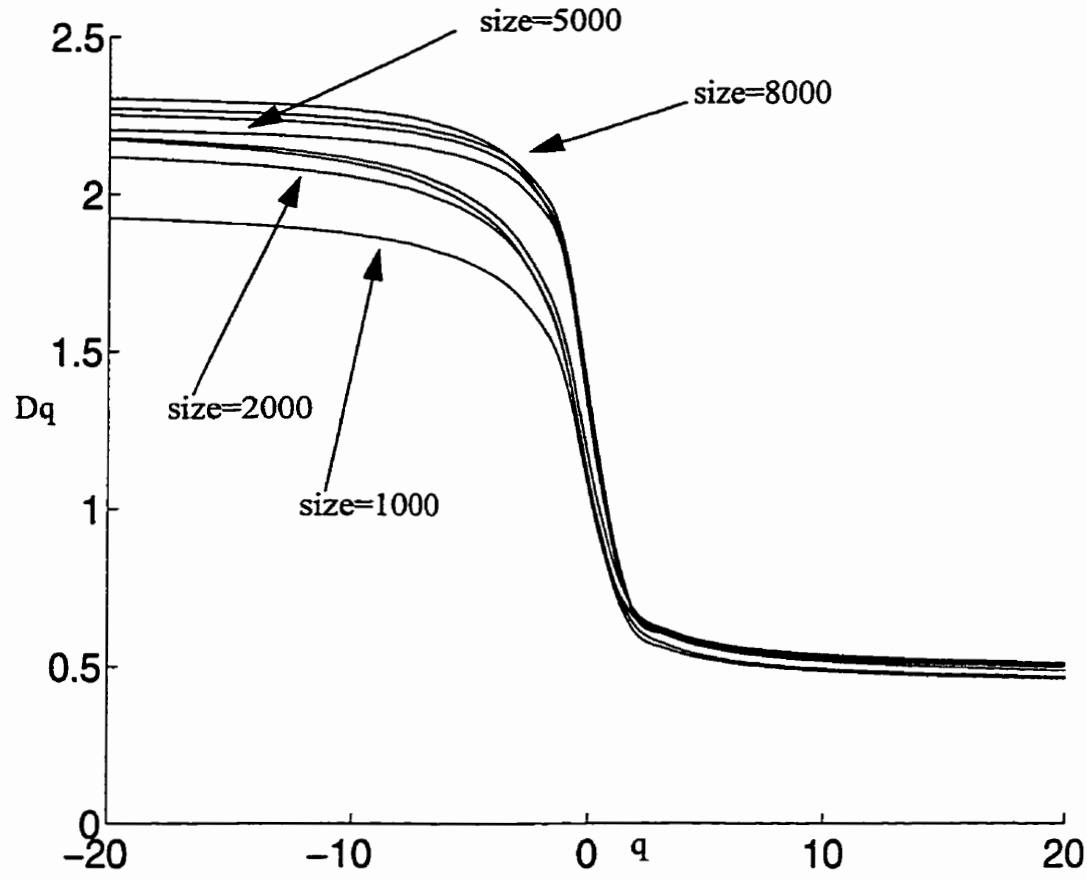

Fig. 5.9. The convergence of the positive orders of the multifractal dimensions for a sample EMG signal.

Let each pattern ρ_i in the training set be associated with a category number η_i, where $\eta_i \in \{1, 2, \ldots, N\}$. When an unknown pattern ρ' is to be classified, the *k*-nearest-neighbours of ρ' are found among the given samples constituting the training set. Let these *k*-nearest-neighbours of ρ', with their associated category number, be given by (ρ'_j, η_j) $j = 1 \ldots k$. The neighbours (ρ'_j, η_j) $j = 1 \ldots k$ are ordered so that ρ'_1 is the nearest and ρ'_k is the farthest from the unknown sample ρ'. Let the corresponding distances of these neighbours from the unknown pattern ρ' be given by d_j $j = 1 \ldots k$

The weight w_j attributed to the jth nearest neighbour can be defined as

$$w_j = \begin{cases} \dfrac{d_k - d_j}{d_k - d_1} & d_k \neq d_1 \\ 1 & d_k = d_1 \end{cases} \tag{5.1}$$

It should be noted that the value of w_j varies from a maximum of one for a nearest neighbour down to a minimum of zero for the most distant of the kth neighbour. The k-nearest-neighbour rule assigns the unknown pattern ρ' to the class for which the weights of the representatives among the k-nearest-neighbours sum to the greatest value.

Dudani shows that the result of weighted k-nearest-neighbours rule is comparable to simple k-nearest-neighbours rule for large training sets but for small training sets the weighted k-nearest-neighbours rule yields smaller probabilities of error.

In our classification experiments, the training set consists of ten samples of each class, six other samples of each class are used for classification. A 7-nearest-neighbour algorithm is used for the results discussed and presented in the later chapters. The samples are 20 dimensional vectors, since we take the first 20 positive orders of the multifractal dimensions as the feature set.

5.5. Summary

This chapter, discussed an experiment with the EMG signals recorded from different functionalities of deltoid and trapezius muscles. The goal of this experiment is to fingerprint the EMG signals according to their functionalities. Multifractal dimensions of the signals are used for characterization. The calculation of the multifractal dimensions was explained, emphasizing the effects of noise and length of time series. The next chapter presents the results of the characterization and classification.

CHAPTER VI

EXPERIMENTAL RESULTS AND DISCUSSION

This chapter presents the results of characterization and classification of the EMG signals acquired in the physical experiments. This is followed by an analysis of the results.

6.1 Experimental Results

The results of the multifractal characterization of the signals are presented in Figs. 6.1 to 6.4. The multifractal dimensions of the signals from abduction, extension, and flexion of middle deltoid muscle form three clusters with an average distance of 0.3 between the centroids of the clusters, the fractal dimensions of abduction being the largest dimensions and the fractal dimensions of flexion being the lowest. The average distance between the points in each cluster is 0.05. The multifractal dimensions of the signals from flexion and abduction of the anterior deltoid form two clusters with centroids, being 0.2 apart on the average, with the fractal dimensions of flexion being larger than the dimensions of abduction. The multifractal dimensions of the signals from extension and abduction of the posterior deltoid form two clusters with centroids being 0.4 apart on average, with the fractal dimensions of the extension being larger than the fractal dimensions of abduction. The results for the upper trapezius does not yield an acceptable classification, with the centroids of the clusters of abduction, extension, and flexion being only 0.02 apart on average and the average distance of samples from the centroids being 0.04. The tables of the classification results of the signals using nearest neighbourhood method also shows that the classification between the different functionalities of anterior, posterior, and middle deltoid are successful, while there is no acceptable classification possible for the upper

trapezius. The results of characterization and classification are in accord with the anatomical description of the function of these muscles. The anterior deltoid is active in forward flexion and abduction of the arm. The largest recruitment of anterior deltoid is seen during the flexion of arm. It also contributes during abduction. Simultaneous activation of the anterior, middle, and posterior deltoid abducts the arm. Abduction is the primary function of the middle deltoid, and this muscle is also active during flexion and extension. The posterior deltoid has its largest recruitment during extension but it also contributes to abduction. The results for the trapezius muscle might be explained by the fact that although trapezius is active in these three functions, the form of contribution to the three movements is similar, i.e. a passive supporting function.

The successful discrimination of the functionalities of deltoid muscle also proves that the slight dislocation of the electrodes, corporated into the experiments, is not a highly influential factor in the fractal dimension values of the EMG signals. Therefore, it is concluded that the fractal characteristics of the EMG signals are not distorted by slight movements of electrodes due to the movement of the skin over the muscle. The timing scheme of the recordings also yields another important conclusion about the fractal characterization of the EMG signals under study. The experiments show that fractal dimensions of the EMG signals of each functionality of a muscle stays stable within an error range of 0.05 before the development of fatigue. It is emphasized once more that all these conclusions are based upon the behaviour of the positive order fractal dimensions, since the number of points in the reconstructed attractors is not sufficient for correct estimation of small probabilities.

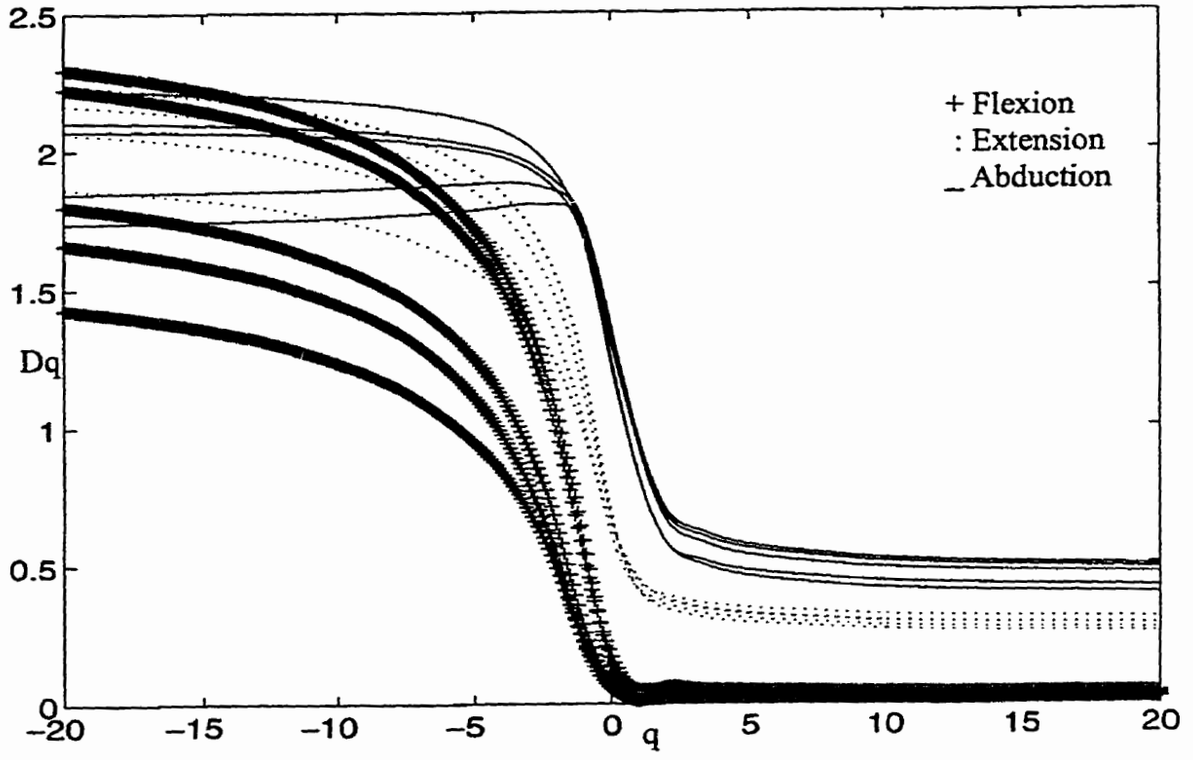

Fig. 6.1.a. The multifractal spectrum of the middle deltoid signals for subject one.

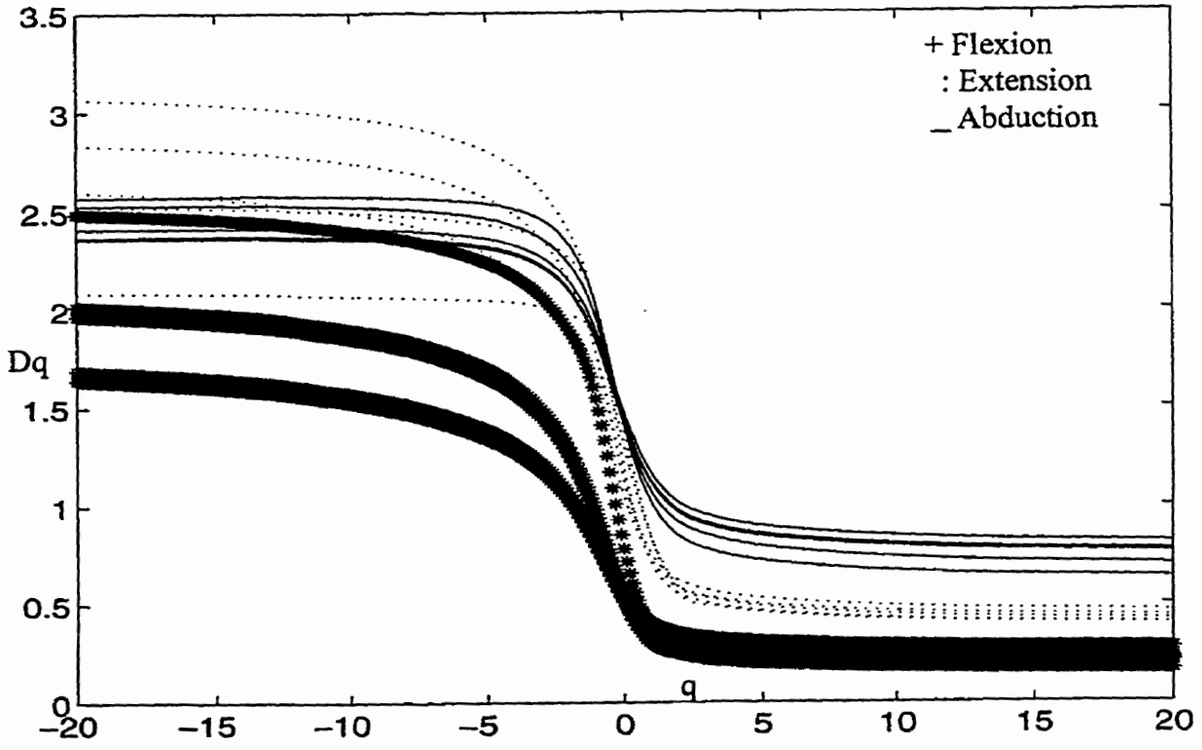

Fig. 6.1.b. The multifractal spectrum of the middle deltoid signals for subject two.

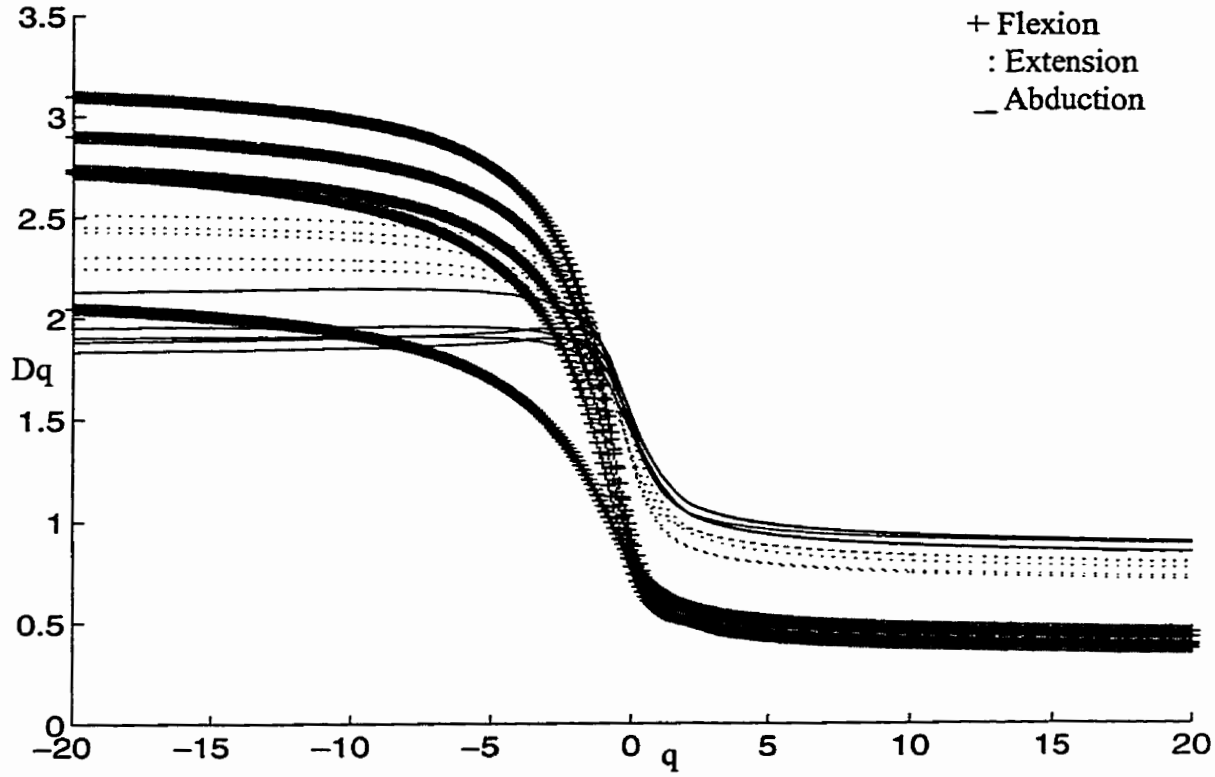

Fig. 6.1.c. The multifractal spectrum of the middle deltoid signals for subject three.

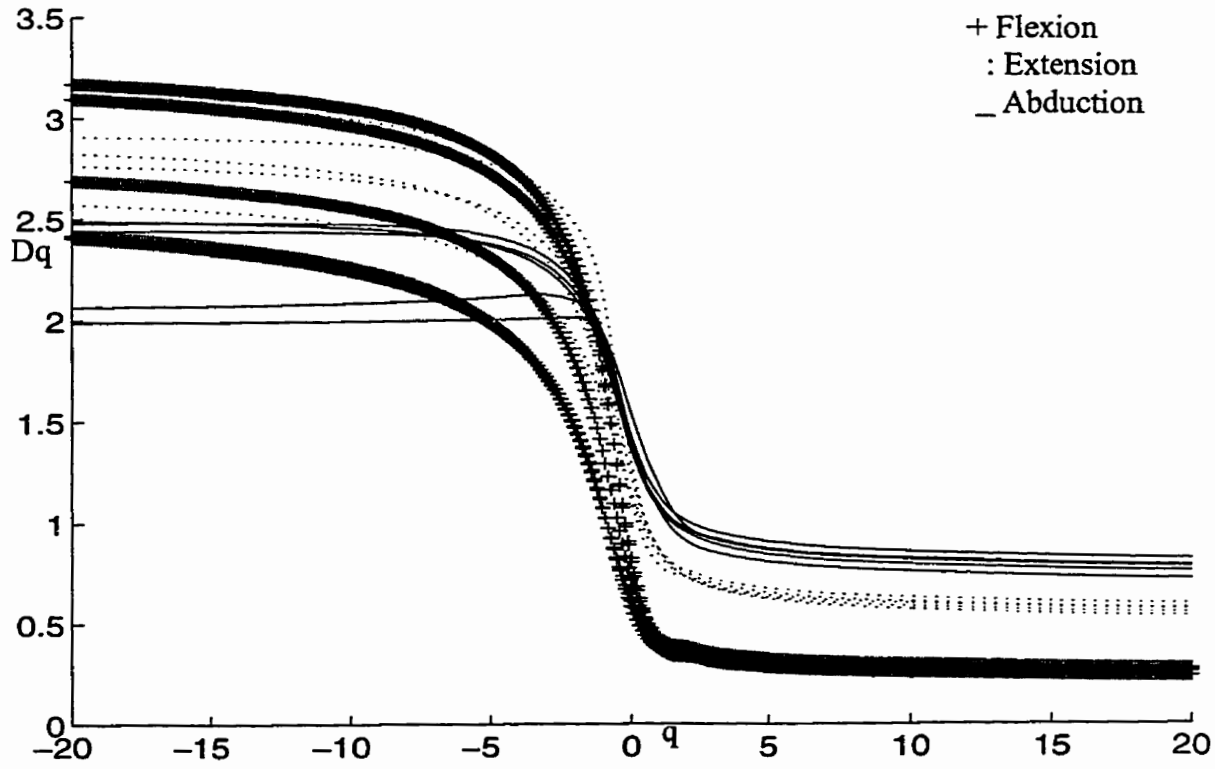

Fig. 6.1.d. The multifractal spectrum of the middle deltoid signals for subject four.

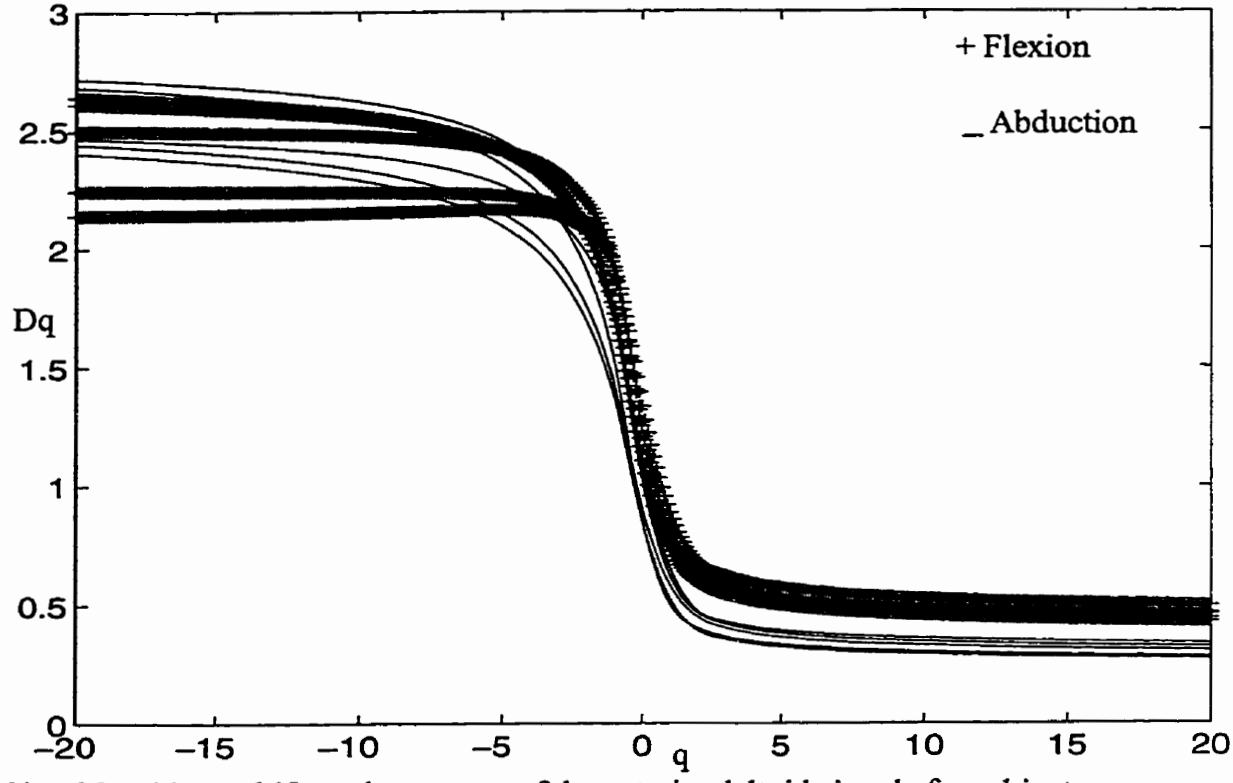

Fig. 6.2.a. The multifractal spectrum of the anterior deltoid signals for subject one.

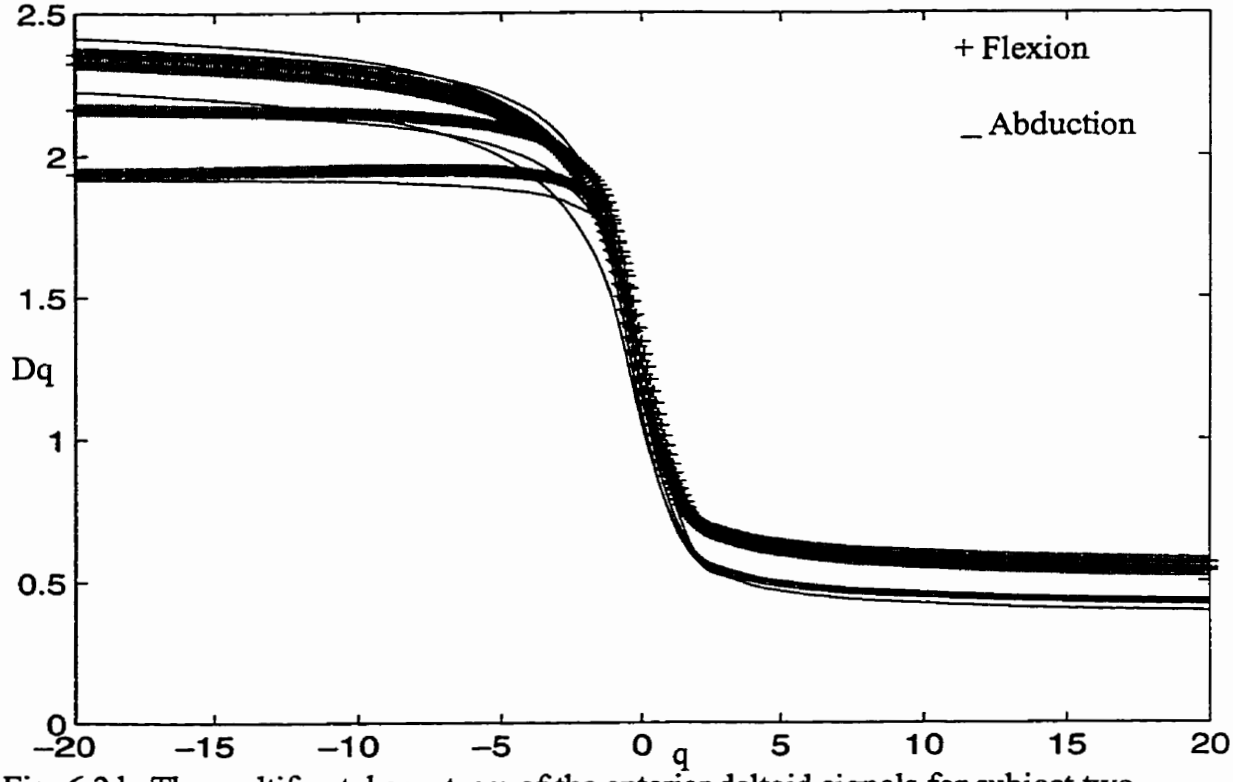

Fig. 6.2.b. The multifractal spectrum of the anterior deltoid signals for subject two.

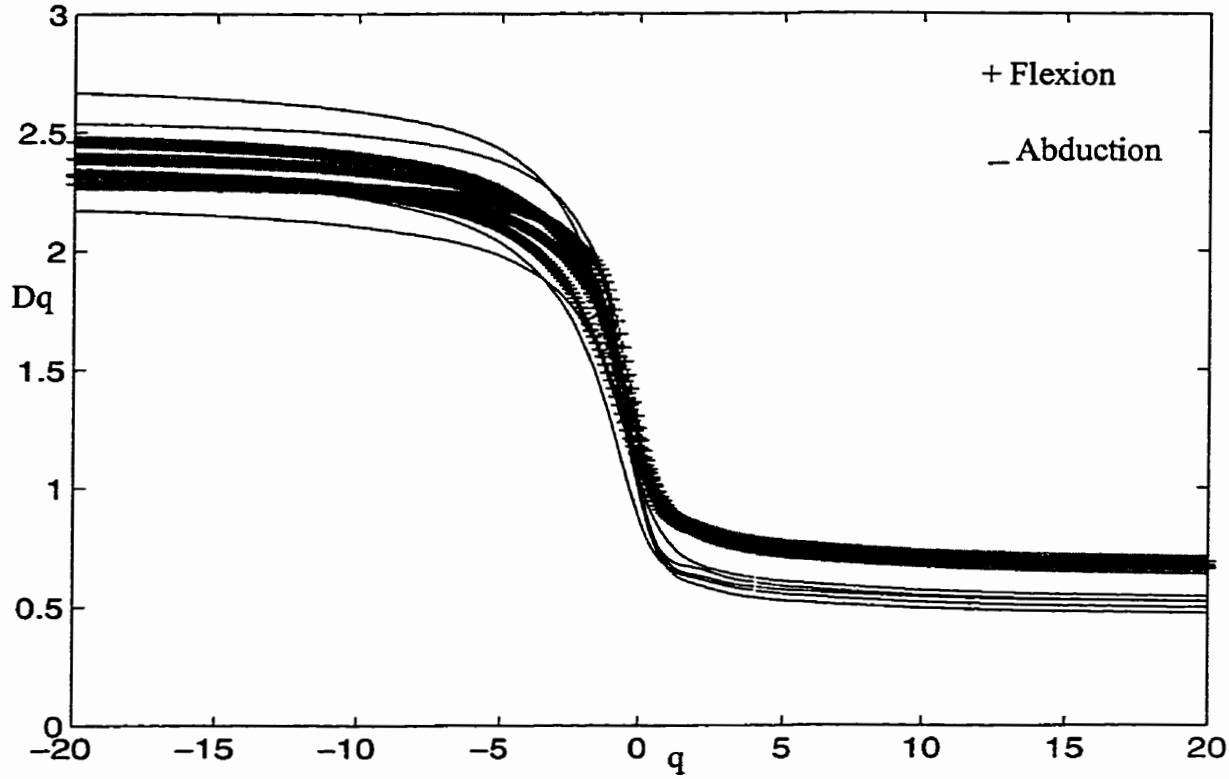

Fig. 6.2.c. The multifractal spectrum of the anterior deltoid signals for subject three.

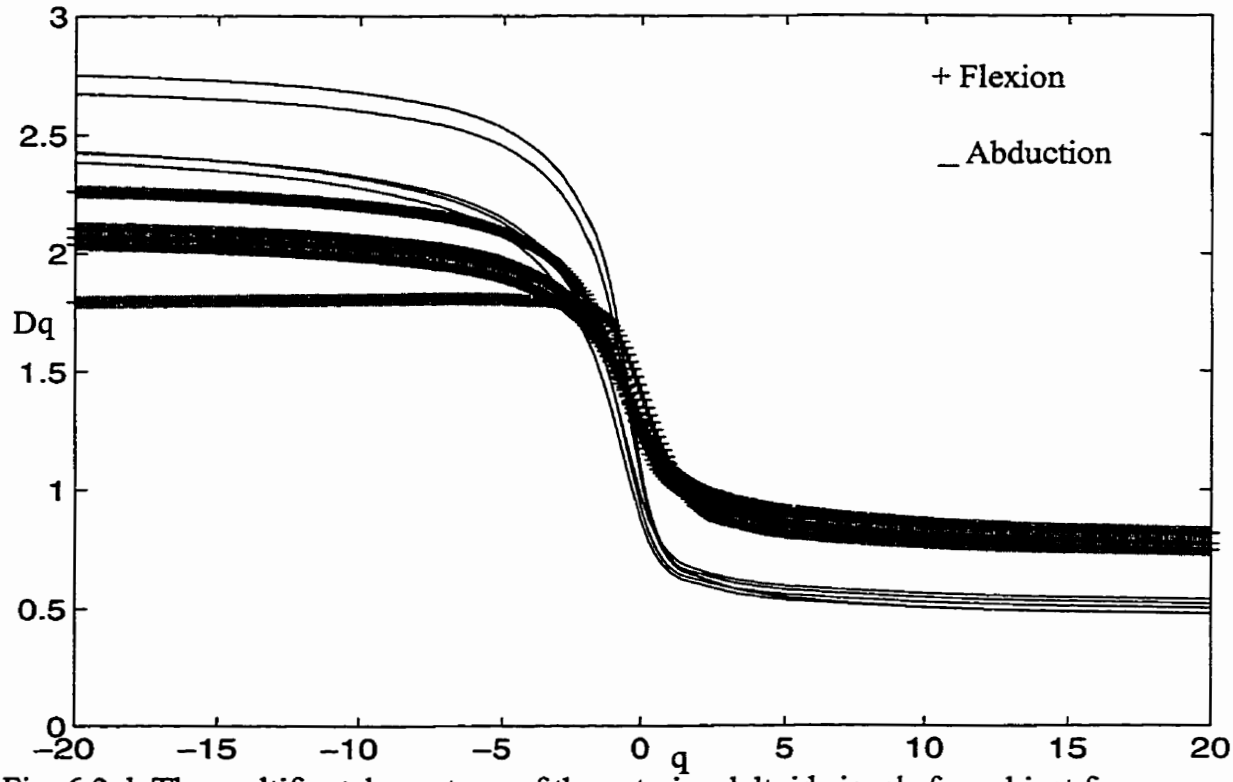

Fig. 6.2.d. The multifractal spectrum of the anterior deltoid signals for subject four.

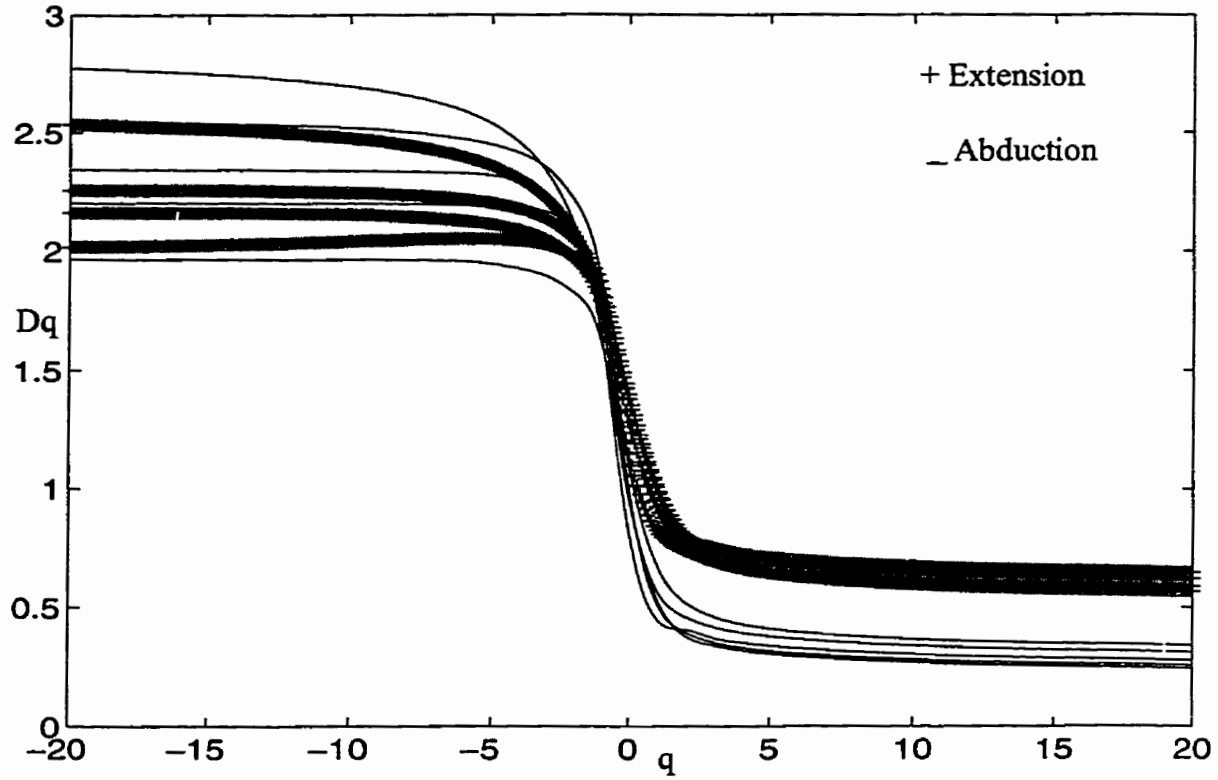

Fig. 6.3.a. The multifractal spectrum of the posterior deltoid signals for subject one.

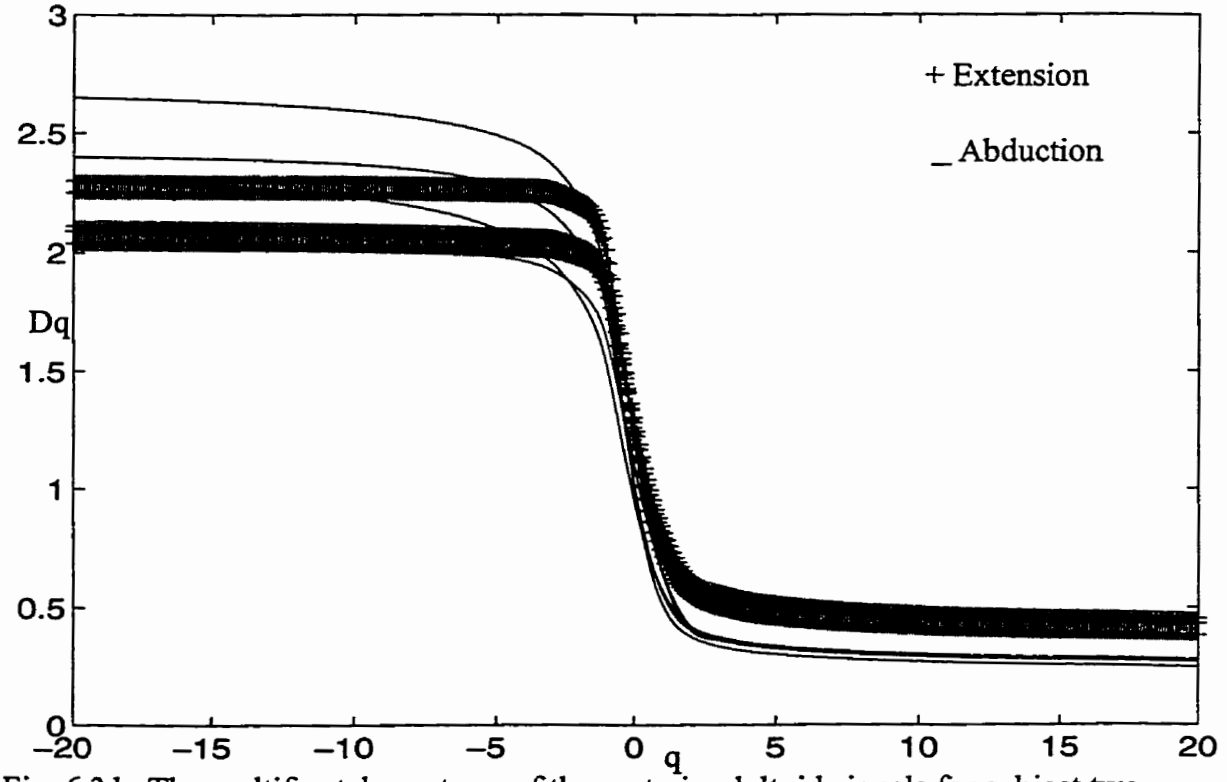

Fig. 6.3.b. The multifractal spectrum of the posterior deltoid signals for subject two.

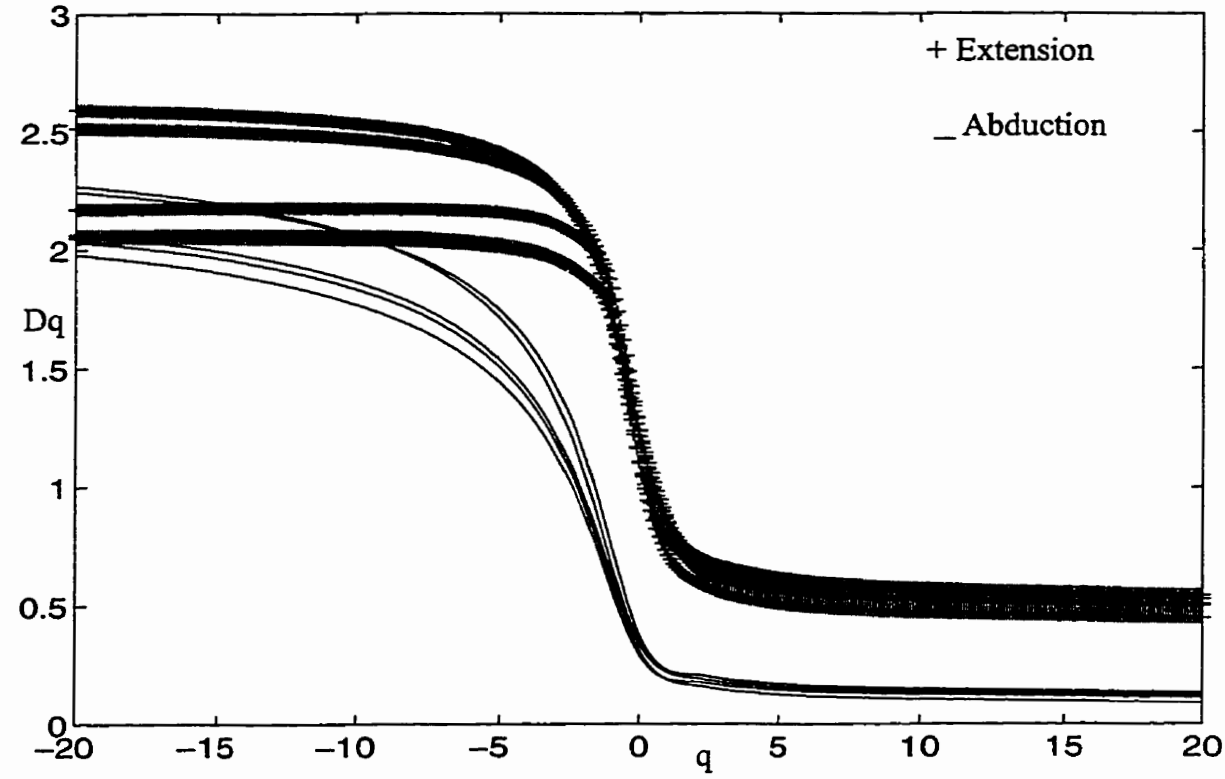

Fig. 6.3.c. The multifractal spectrum of the posterior deltoid signals for subject three.

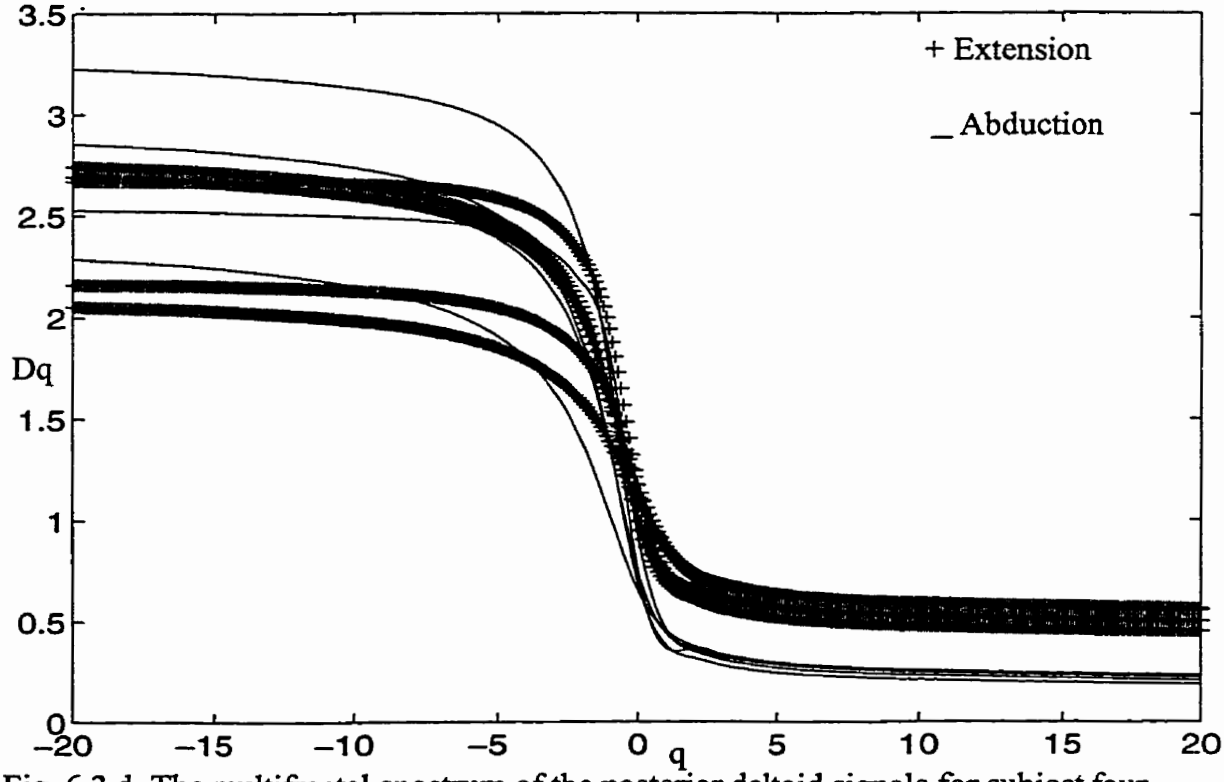

Fig. 6.3.d. The multifractal spectrum of the posterior deltoid signals for subject four.

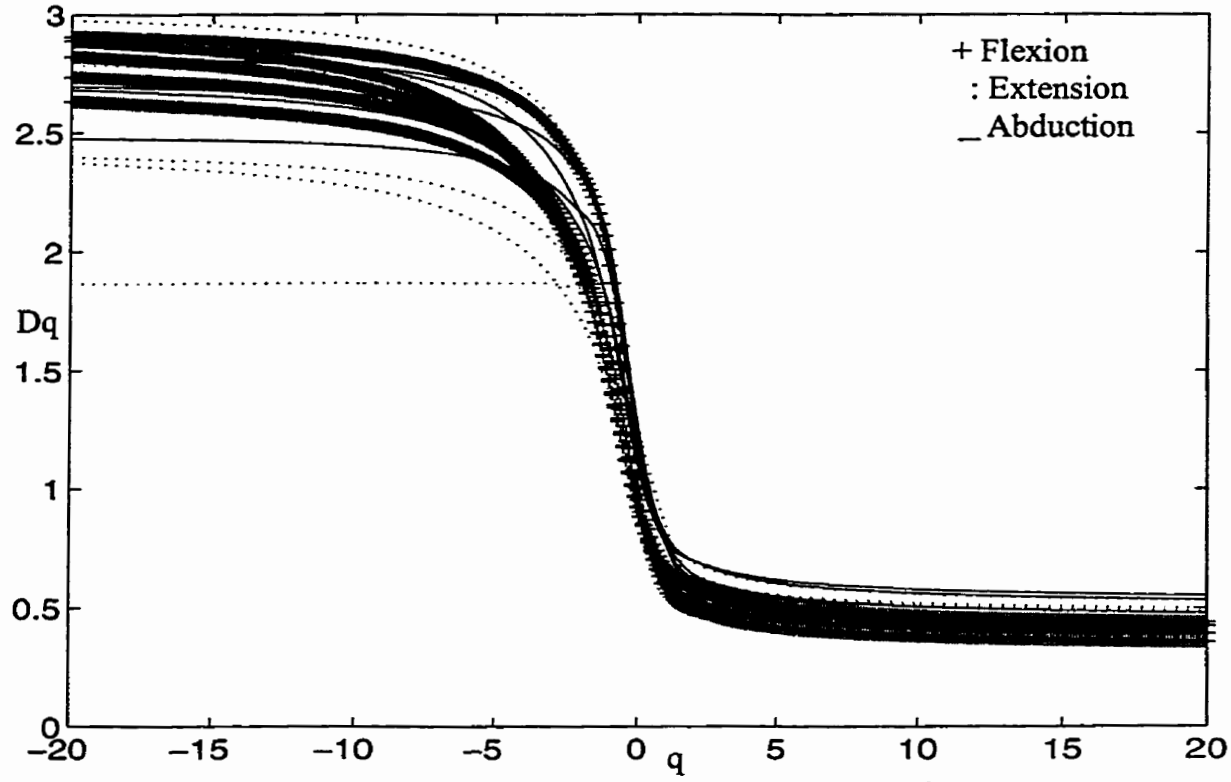

Fig. 6.4.a. The multifractal spectrum of the upper trapezius signals for subject one.

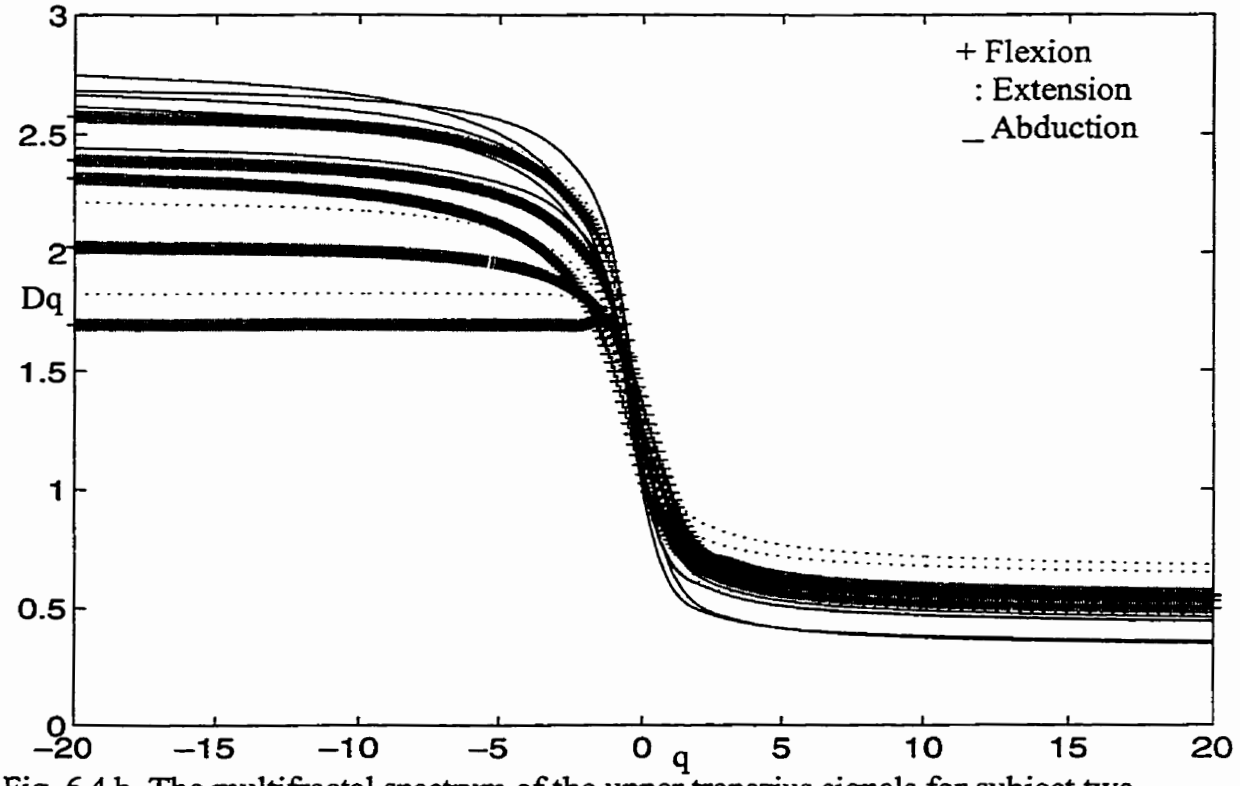

Fig. 6.4.b. The multifractal spectrum of the upper trapezius signals for subject two.

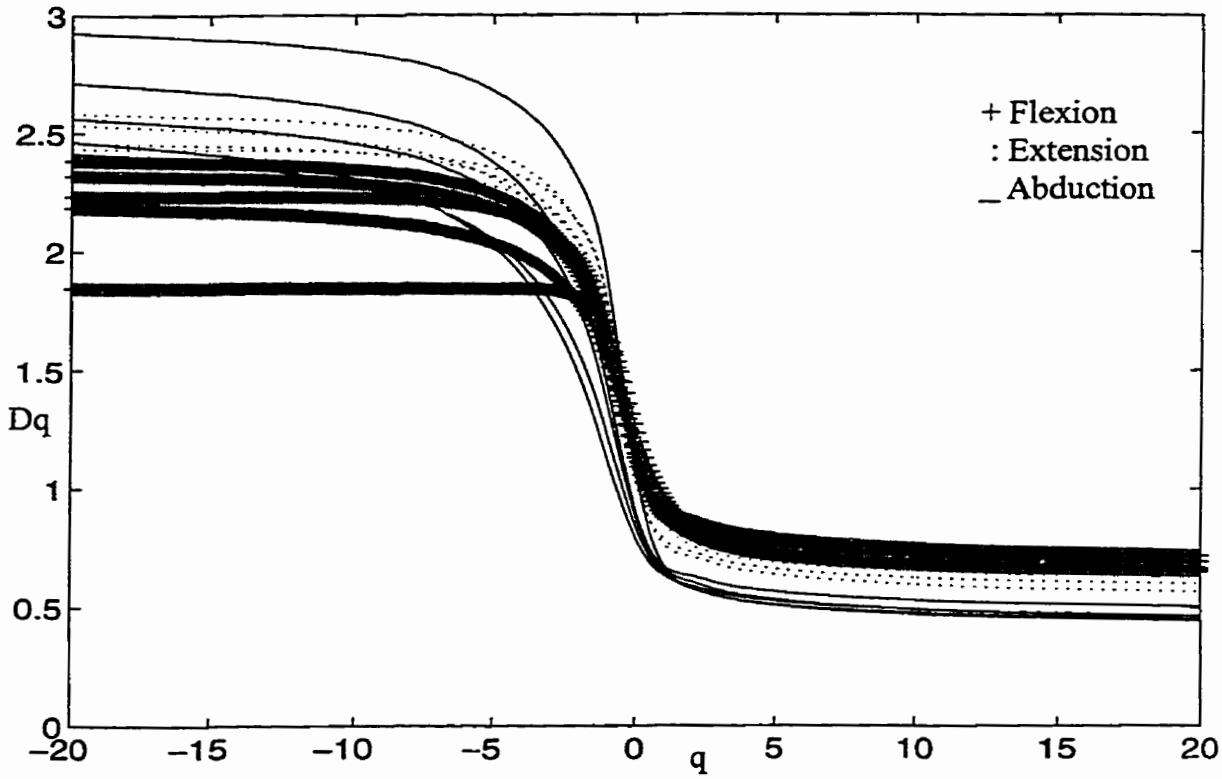

Fig. 6.4.c. The multifractal spectrum of the upper trapezius signals for subject three.

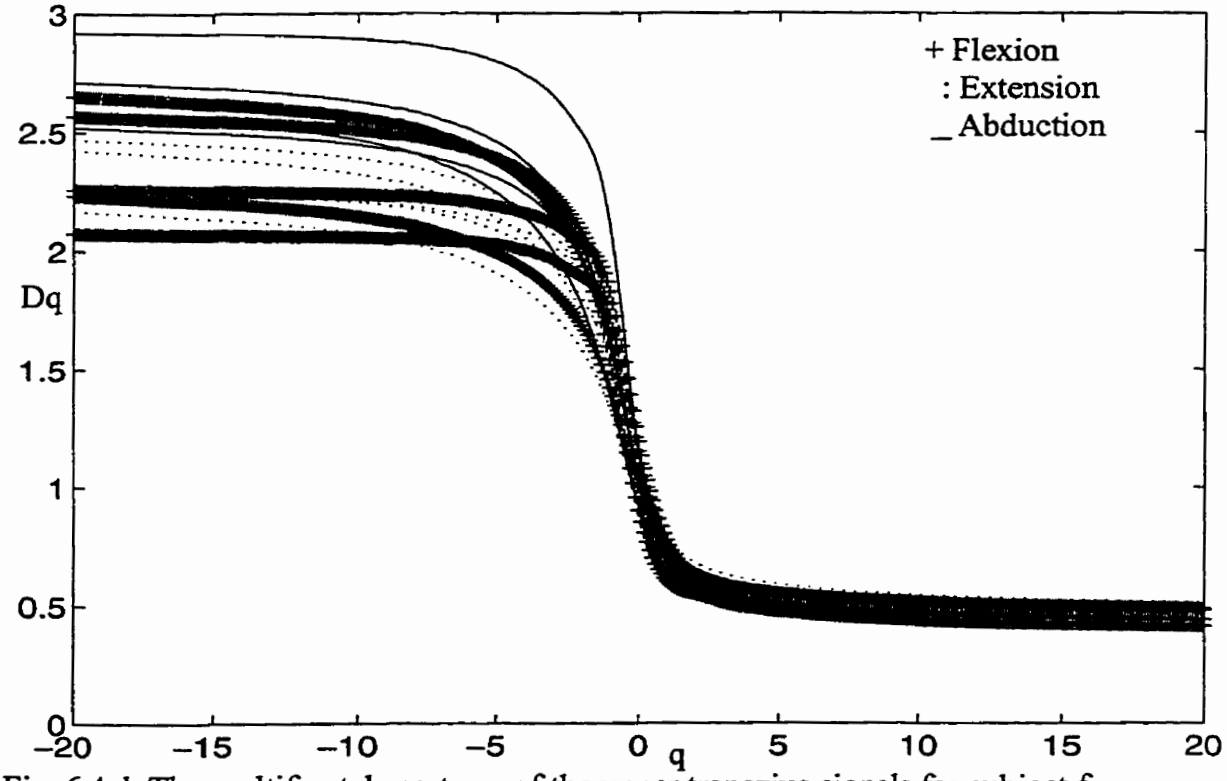

Fig. 6.4.d. The multifractal spectrum of the upper trapezius signals for subject f

	Abduction	Flexion
Abduction	%100	%0
Flexion	%10	%90

Table 6.1. Classification for anterior deltoid.

	Abduction	Extension
Abduction	%100	%0
Extension	%0	%100

Table 6.2. Classification for posterior deltoid.

	Abduction	Extension	Flexion
Abduction	%100	%0	%0
Extension	%10	%90	%0
Flexion	%0	%0	%100

Table 6.3. Classification for middle deltoid.

	Abduction	Extension	Flexion
Abduction	%20	%50	%30
Extension	%40	%20	%40
Flexion	%20	%40	%40

Table 6.4. Classification for upper trapezius.

In the course of the characterization and classification of the signals several precautions were taken to minimize the effect of noise. Signals with very low SNR values, were discarded and no converging embedding dimension was calculated. For the rest of the signals the smallest hypercube well above the range affected by the noise levels was chosen. Nevertheless the calculations are not totally free from the effect of noise levels. A comparison of the experimental results from the middle deltoid and trapezius muscle confirms again that the discrimination of the different classes is not influenced by the different SNR values of the classes. The signals from the three different classes for the trapezius muscle have different SNR values but this alone does not cause a classifiable difference among them. The results of the experiments also gives one an idea of the degree of the effectiveness of cross talk between anterior, posterior, and middle deltoid. As explained the amplitude levels of signals recorded from anterior deltoid in extension and from the posterior deltoid in flexion are too low and a low embedding dimension is not extracted for them. In both these movements, the middle deltoid is quite active. If an influential cross talk existed between middle and anterior, or middle and posterior portions of deltoid, the activity of abduction should have appeared in the signals recorded from anterior and posterior muscles in the two movements mentioned above, which is not the case.

6.2. Summary

This chapter presented the results of characterization and classification of the EMG signals acquired from trapezius and deltoid muscles in the three movements of abduction, extension, and flexion. It is shown that the classification of the functionality of the deltoid muscle is possible by the multifractal dimensions of the EMG signals. The effect of noise and cross talk in the experimental results is also discussed.

It is shown that the multifractal dimensions of the EMG signals can be used as characteristic features which are related to the contribution of the muscle in the movement. Signals of muscles with a supporting contribution generally have smaller fractal dimensions in comparison to the signals of the same muscle when playing a primary role in a movement. The multifractal feature of the EMG signals can be used for discriminating among the different functions of a muscle.

CHAPTER VII

CONCLUSIONS AND RECOMMENDATIONS

7.1 Conclusions

In this thesis it is shown that the EMG signals recorded during the contraction of muscles (specifically deltoid and trapezius) exhibit a chaotic behaviour which is associated with low dimensional strange attractors existing in the phase spaces reconstructed from these single variable signals. A framework is developed for the analysis of the chaotic behaviour of EMG signals using minimum mutual information and false nearest neighbourhood techniques for the reconstruction of the strange attractors and the generalized correlation integral for the calculation of the multifractal dimensions.

It is shown that the multifractal dimensions of the EMG signals can be used as characteristic features which are related to the contribution of the muscle in the movement. Signals of muscles with a supporting contribution generally have smaller fractal dimensions in comparison to the signals of the same muscle when playing a primary role in a movement. The multifractal feature of the EMG signals can be used for discriminating among the different functions of a muscle.

The experimental analysis also indicate that the multifractal dimensions of the EMG from deltoid and trapezius is not effected by cross talk, that the EMG signals with SNR lower than 10 are so contaminated by noise that a strange attractor with an embedding dimension smaller than 20 is not conceivable for them, that the dislocations of the electrode which are smaller than 5 millimeters do not affect the multifractal dimensions of the signals, and that the multifractal dimensions of the EMG signals recorded from a muscle in a certain movement, before the development of fatigue is stable (with a precision of ± 0.1).

7.2 Contributions

This thesis has made the following contributions:

- Verification of the chaotic behaviour of the EMG signal.
- A technique for the estimation of the multifractal dimensions of the EMG signals.
- A study of how the multifractal dimensions of the EMG signals are related to the functionality of the muscle producing the signals.
- A study of the effect of noise levels, cross talk, and dislocations of electrodes during the recordings, on the stability of the multifractal characteristics of the EMG signals.

7.3 Recommendations

The following recommendations are suggested for furthur research on this topic:

- Calculation of multifractal dimensions for signals recorded with higher sampling rates, in order to achieve accurate estimates of smaller probabilities.
- Examining the possibility of classification of flexion, abduction, and extension from the signals recorded from upper trapezius, using recording schemes which minimizes the noise levels as much as possible.
- Examining of the possibility of improving the classification by changing the cut off frequency ranges of the signal filters.

REFERENCES

[Addi97] S. Addison, *Fractals and Chaos*. Philadelphia and Bristol: Institute of Physics Publishing, 1997, 256 pp. {ISBN 0-7503-0399-9 (HBA)}

[AnGM94] C. J. Anmuth, G. Goldberg, and N. H. Mayor, "Fractal dimension of electromyographic signals recorded with surface electrodes during isometric contractions," *Muscle & Nerve*, vol. 17, no. 8, pp. 953-954, 1994.

[AtSV88] H. Atmanspacher, H. Scheingraber, and W. Voges, "Global scaling properties of a chaotic attractor reconstructed from experimental data," *Phys. Rev.*, vol. A37, no. 4, pp. 1314-1322, 1988.

[BaDe85] J. V. Basmajian and C. J. De Luca, *Muscles Alive their Functions Revealed by Electromyography*, Baltimore, MaryLand: Williams & Wilkins, 1985, 561 pp. {ISBN 0-683-00414-X}

[BSAM73] T. Budzynski, J. Stoyva, C. Adler, and D.J. Mullaney, "EMG biofeedback and tension study," *Psychosomatic Med.* vol. 35, pp. 484-496, 1973.

[CrKa98] J. R. Cram and G. S. Kasman, *Introduction to Surface Electromyography,* Maryland: ASPEN, 1998, 408 pp. {ISBN 0-8342-0751-6}

[Chen97] H. Chen, *Accuracy of Fractal and Multifractal Measures for Signal Analysis,* M.Sc. Thesis, Winnipeg, MB: Department of Electrical and Computer Engineering, University of MAnitoba, 1997, 193 pp.

[Cant83] G. Cantor, " Über unendliche, lineare Punktmannigfaltigkeiten V," *Mathematische Annalen,* vol. 21, pp. 545-591, 1983.

[ChPF97] A. Chandiramani, J. Palace, and C. J. Fowler, "How to recognize patients with Parkinson who should not have urological surgery," *British Journal of Urol-*

ogy, vol. 80, no. 1, pp. 100-104, 1997.

[Deva89] R. L. Devaney, *An Introduction to Chaotic Dynamical Systems*, NewYork, NY: Addison-Wesley, 1989, pp. 331. {ISBN 0-201-13046-7}

[Duda76] S. A. Dudani, *"The distance weighted k-nearest-neighbour rule,"* IEEE transactions on Systems, Man, and Cybernatics, vol. SMC-6, no. 4, pp. 325-327, 1976.

[EKRC86] J. P. Eckmann, S. O. Kamphorst, D. Ruelle, and S. Ciliberto, "Lyapunov exponents from time series," *Phys. Rev.,* vol. 34A, pp. 4971-4979, 1986.

[ErCH97] A. Erfanian, H. J. Chizeck, and R. M. Hashemi, "Chaotic activity during electrical stimulation of paralyzed muscle," *Proc. IEEE 18th Annual International Conf. Eng. in Medicine and Biology Society*, vol. 4, pp. 1756-1757, 1997.

[Farm82] D. Farmer, "Chaotic attractors of an infinite-dimensional system," *Physica*, vol. 4D, pp. 366-393, 1982.

[FrWi73] H. V. Freund and C. W. Wita, "Discharge characteristics of single motor units in normal subjects and patients with supraspinal motor disturbances," *New Dev. Electromyography Clin. Neurophysiol,* vol. 3, pp. 242-250, 1973.

[Fras89] A. M. Fraser, "Information and entropy in strange attractors," *IEEE trans. Inf. theory,* vol. 33, pp. 245-262, 1989.

[FrSw86] A. M. Fraser and H. L. Swinney, "Independent coordinates for strange attractors from mutual information," *Phys. Rev.,* vol. 33A, no. 2, pp. 1134-1139, 1986.

[GaRa92] A. V. Gapanov-Grekhov and M. I. Rabinovich, *Nonlinearities in Action,*

NewYork, NY: Springer-Verlag, 1992, 191 pp. {ISBN 0-387-51988-2}

[GiDe90] C. C. A. M. Gielen and J. J. Denier Van der Gon, "The activation of motorunits in coordinated arm movements in humans," *News in Physiological Sciences*, vol. 5, pp. 159-163, 1990.

[GiCz95] J. A. Gilter, and M. J. Czerniecki, "Fractal analysis of the electromyographic interefrence pattern," *Journal of Neuroscience Methods*, vol. 58, no. 1, pp. 103-108, 1995.

[Grie96] W. S. Grieder, *Variance Fractal Dimension for Signal Feature Enhancement and Segmentation from Noise,* M.Sc. Thesis, Winnipeg, MB:Department of Electrical and Computer Enginerring, University of Manitoba, 1996, 369 pp.

[GrPr83a] P. Grassberger and I. Procaccia, "Characterization of strange attractors," *Phys. Rev. Lett.,* vol. 50, no. 5, pp. 346-349, 1983.

[GrPr83b] P. Grassberger and I. Procaccia, "Measuring the strangeness of attractors," *Physica,* vol. 9D, pp. 189-208, 1983.

[GrPr84] P. Grassberger and I. Procaccia, "Dimension and entropies of strange attractor from a fluctuating dynamics approach," *Physica*, vol. 13D, pp. 34-54, 1984.

[GrSZ85] D. Graupe, J. Salahi, and DeSong Zhang, "Stochastic analysis of myoelectric temporal signatures for multifunctional single-site activation of prostheses and orthoses," *J. Biomed. Eng.*, vol. 7, Jan. 1985.

[Guyt71] A. C. Guyton, *Textbook of Medical Physiology*, Philadelphia, PA: W. B. Sauders Company, 1971, pp. 1032. {ISBN 0-7216-4392-2}

[Heno76] M. Hénon, "A two dimensional mapping with a strange attractor," *Commun.*

Math. Phys., vol. 50, ch. 5, pp. 69-77, 1976.

[HeSY76] E. Hennemenn, B. T. Shahani, and R. R. Young, "Voluntary control of human motor units," *The Motor System: Neurophysiology & Muscle Mechanism,* pp. 73-78, 1976.

[HGRG96] A. J. Hong, J. B. Gelblum, J. J. Rechtien, A. J. Gilte, "Technology assessement of the use of surface EMG in the diagnosis and treatment of nerve and muscle disorder," *Muscle & Nerve*, vol. 19, no. 3, pp. 392-395, 1996.

[Huxl57] A. F. Huxley, "Muscle-structure and theories of contraction," *Prog. Biophys.*, vol. 7, pp. 255-318, 1957.

[JoSm87] D. W. Jordine and P. Smith, *Nonlinear Ordinary Differential Equations*, NewYork, NY: Oxford Applied Mathematics & Computing Science Series, 1987, 287 pp.

[KeBA92] M. B. Kennel, R. Brown, and H. D. I. Abarbanel, "Determining embedding dimensions for phase space reconstruction using a geometeric construction," *Phys. Rev.*, vol. 45A, no. 6, pp. 3403-3411, 1992.

[Kins94] W. Kinsner, *Fractal Dimensions: Morphological, Entropy, Spectrum, and Variance Classes,* Tech. Report, DEL94-4, Department of Electrical and Computer Engineering, University of Manitoba, May 1994, 140 pp.

[Kins97] W. Kinsner, *Fractal and Chaos Engineering*, 24.721 Course Notes, University of Manitoba, 1997.

[Koch04] H. von Koch, "Sur une courbe continue sans tangente obtenue par une construction géometrique élémentaire," *Arkiv för Matematik*, vol. 1, pp. 681-704, 1904.

[Lang96] A. Langi, *Wavelet and Fractal Processing and Compression of Nonstationary Signals*, Ph. D. Thesis, Winnipeg, MB:Department of Electrical and Computer Engineering, University of Manitoba, 1996, 466 pp.

[Lewi91] K. Lewit, *Manipulative Therapy in Rehabilitation of the Locomotor System*, Boston: Butterworth Heinemann, 1991.

[Lore63] E. N. Lorenz, "Deterministic non-periodic flow," *J. Atmos. Sci.*, vol. 20, pp. 130-141, 1963.

[Mand80] B. B. Mandelbrot, "Fractal aspects of the iteration of $z \rightarrow \lambda z(1-z)$ for complex λ and z," *Annals New York Academy of Science*, vol. 357, pp. 249-259, 1980.

[Mand83] B. B. Mandelbrot, *The Fractal Geometery of Nature*, NewYork, NY: Freeman, 1983, 468 pp. {ISBN 0-7167-1186-9}

[Mane81] R. Mané, "On the dimension of the compact invariant set of certain nonlinear maps," *in Lecture Notes in Mathematics 898*, Springer-Verlag, pp. 230-242, 1981.

[Mcco96] S. A. J. Mc Comas, *Skeletal Muscle Form and Function*, Champaign, IL: Human Kinetics, 1996, 400 pp. {ISBN 0-87322-780-8}

[MiCR98] B. Michelangelo, O. Cristina, and C. Roberto, "Early developent of EMG localized fatigue in the hand muscles of patients with chronic heart failure," *Archives of Phys. Med. and Re., vol.* 79, no. 1, pp. 41-45, 1998.

[Mous97] Z. M. K. Moussavi, *The Effect of Treatment on Myofascial Trigger Points in Upper Trapezius Muscle: EMG Fatigue Parameters, Joint Range of Motion, Pain and Perception of Disability*, Ph. D. Thesis, Winnipeg, MB: Depart-

ment of Electrical and Computer Engineering, University of Manitoba, 1997, 111 pp.

[PaSc87] K. Pawelzik and H. G. Schuster, "Generalized dimensions and entropies from a measured time series," *Phys. Rev.*, vol. A35, no. 1, pp. 841-844, 1987.

[PCFS80] N. H. Packard, J. P. Crutchfield, J. D. Farmer, and R. S. Shaw, "Geometery from a time series," *Phys. Rev. Lett.*, vol. 45, no. 9, pp. 712-715, 1980.

[PeJS92] H. Peitgen, H. Jürgens, and D. Saupe, *Chaos and Fractals: New Frontiers of Science,* New York, NY: Springer-Verlag, 1992, 894 pp. {ISBN 0-387-97903-4}

[RBOA87] F. J. Romeiras, A. Bondeson, E. Ott, T. M. Antonsen, and C. Grebogi, "Quasiperiodically forced dynamical systems with strange non-chaotic attractors," *Physica*, vol. 26D, pp. 277-294, 1987.

[Rifa98] R. Rifaat, *Multifractal Analysis of DNA,* M.Sc. Thesis, Winnipeg, MB: Department of Electrical and Computer Engineering, University of MAnitoba, 1998, 107 pp.

[RoCD93] M. T. Rosentien, J. J. Collins, and C. J. De Luca, "A practical method for calculating largest Lyapunov exponents from small data sets," *Physica*, vol. 65D, pp. 117-134, 1993.

[RuTa71] F. Ruelle, F. Takens, "On the nature of turbulence," *Comm. Math. Phys.*, vol. 20, pp. 167-192, 1971.

[SCIM97] F. Stocchi, A. Carbone, M. Inghiller, A. Monge, S. Ruggieri, A. Berardelli, and M. Manfredi, "Urodynamic and neurophysilogical evaluation in Parkinson's disease and multiple system atrophy," *Journal of Neurology Neurosur-*

gery and Psychiatry, vol. 62, no. 5, pp. 507-511, 1997.

[ScTh81] E. M. Schmidt & J. S. Thomas, "Motor unit recruitement order: modification under volitional control," *Progress in Neurophysiology*, vol. 9, pp. 145-148,1981.

[Shaw97] D. B. Shaw, *Classification of Transmitter transients using Fractal Measures and Probabilistic Neural Networks*, M.Sc. Thesis, Winnipeg, MB:Department of Electrical and Computer Engineering, University of Manitoba, 1997, 375 pp.

[SiOG98] D. U. Silverthorn, W. C. Ober, C. W. Garrison, and A. C. Silverthorn, *Human Physiology an Integrated Approach*, Upper Saddle River, New Jersey: Prentice Hall, 1998, 783 pp.

[Take81] F. Takens, "Detecting strange attractors in turbulence," *in Lecture Notes in Mathematics 898,* Springer-Verlag, pp. 366-381, 1981.

[WoNK82] S. Wolf, M. Nacht, and J. Kelly, "EMG feedback training during dynamic movement for low back pain patients," *Behav. Ther.*, vol. 13, pp. 395-406, 1982.

[WSSV85] A. Wolf, J. B. Swift, H. L. Swinney, and J. A. Vastano, "Determining Lyapunov exponents from a time series," *Physica*, vol. 16D, pp. 285-317, 1985.

APPENDIX A

A.1. Structure Chart

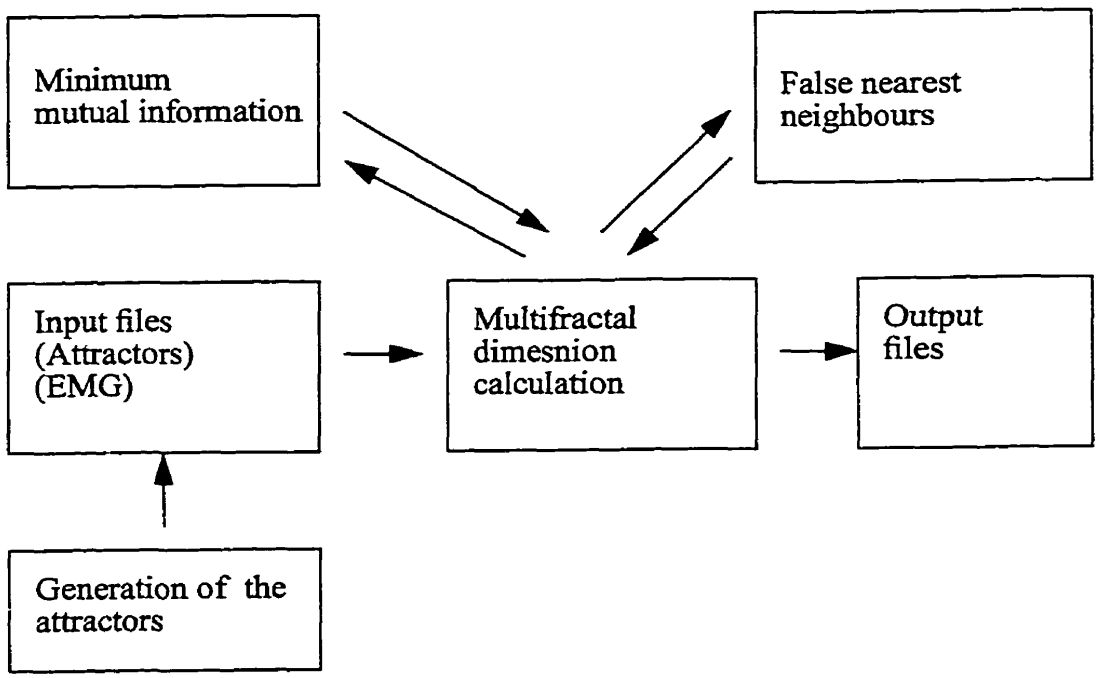

This chart shows how the varoius functions of the program are related to each other and how the modules in the program interact.

APPENDIX B

Source Code

```
/*#########################################################################

Program: Calculation of the percentage of the false nearest neighbours.

Program description: This program calculates the percentage of the false
nearest neighbours of the reconstructed phase space for different embedding
dimensions. The embedding dimensions, the time series and the lag are the
inputs and the threshold values for the recognition of false neighbours
are chosen by the user. The output is the file which contains the percentage
of false neighbours in each pass from one enbedding dimension to a higher one.

#########################################################################*/
#include <stdio.h>
#include <stdlib.h>
#include <math.h>
#include <malloc.h>


const  int   lag=1;        // lag of the time series
const  int   R=10;         // number of the Rtolerance factors
const  int   N=2000;        // series size
const  int   M=7;          // number of embedding dimensions

// enter the values of Rtol
// enter embedmin and embedmax and Rv and Atol
int main()
{

      FILE *fin,  *fout;
      char infile[255];
      char outfile[255];
      double  time[N+1];
      double  D1[N+1];
      double  D2[N+1];
      double  D3[N+1];
      double  result[M+1][R+1];
      double  Rtol[R+1];
      int   m,n,i,j,r;
      double  sum,  mindist, minind, nextdist, distance;
      double  Rv ,Ra, Rb, Rt, Rr, Atol;
      int     embedmin;
      int     embedmax;


      for (i=1 ; i <= M ; i++)
      {
```

```
 for  ( j=1 ; j <= R ; j++)
   {
     result[i][j]=0;
    }
     }

Rtol[1]=0.001;
Rtol[2]=0.005;
Rtol[3]=0.01;
Rtol[4]=0.05;
Rtol[5]=0.1;
Rtol[6]=0.5;
Rtol[7]=1;
Rtol[8]=5;
Rtol[9]=10;
Rtol[10]=15;
/*Rtol[11]=;
Rtol[12]=;
Rtol[13]=;
Rtol[14]=;
Rtol[15]=;
Rtol[16]=;
Rtol[17]=;
Rtol[18]=;
Rtol[19]=;
Rtol[20]=;
Rtol[21]=;
Rtol[22]=;
Rtol[23]=;
Rtol[24]=;
Rtol[25]=*/



embedmin=1;
embedmax=7;
Rv=0.6;
Atol=0.75;

fin=fopen("/home/ee/tina/emgfiles/programs/noise.asc","r+");
fout=fopen("/home/ee/tina/emgfiles/programs/false1.asc","w");

for (i=1 ; i<=N ; i++)
 {
  fscanf(fin,"%lf\n", &time[i]);
```

```
  // printf("%lf\n",time[i]);
  }


for ( m=embedmin ; m<=embedmax  ; m++)
{


   for ( i=1 ; i<=N ; i++)
    {
      mindist=10000;

      nextdist=0;

      for  (j=1 ; j <= N ; j++)
       {
         if ( i!=j)
            {
              distance=0;
              for  ( n=0 ; n <= m-1 ; n++)
                {
                 distance+= (double)pow ( (time[i+(lag*n)]-time[j+(lag*n)]) , 2);
                 }
               if (distance < mindist)
                 {
                  mindist=distance;

                 nextdist=(double)pow ( (time[i+(lag*m)]-time[j+(lag*m)]) , 2);
                  }

            }
       }


      D1[i]=mindist;
      D2[i]=nextdist;
     // printf("%e",mindist);
      }



   for ( i=1  ; i<= N  ; i++ )
   {
```

```
        Rr=pow(D2[i],0.5)/pow(D1[i],0.5);
        Rb=(double)pow(D1[i]+D2[i],0.5);
        for  ( r=1 ; r<= R ; r++)
          {
           Rt=Rtol[r];
           if  ( Rr > Rt  || ( Rb<(Rv+Atol) &  Rb>(Rv-Atol) ) )
                    {
                      result[m][r]++;
                    }




          }
        }

      } // membed


  for ( i=1 ; i<=M ; i++)
  {
     for (j=1 ; j<=R ; j++)
          {

           result[i][j]=result[i][j]/N;
           fprintf(fout,"%e\n",result[i][j]);

          }
   }


 fclose(fin);
 fclose(fout);

} // main
```

```
/*#########################################################################

Program: Calculation of the minimum mutual information.

Program description: This program calculates the minimum mutual information
of a time series. The input is the time series and the grid size for estimation
of the probabilities. The output is the mutual information for the different
lag ranges.
#########################################################################*/
#include <stdio.h>
#include <stdlib.h>
#include <math.h>
#include <malloc.h>



const int  N=8000;      // series size
const int  L=448;          //bigger than double the size of the max value of the abs  time
series
                  // L/2 should be integer

const int gridsize=4;     // should be integer, L/gridsize should be integer
const int dist=212;       // abs of minx+1
const int m=112;       // L/gridsize

int main()
{

      FILE *fin,  *fout;
      char infile[255];
      char outfile[255];
      int  time[N+1];
      double Att[L+1][L+1];
      double prow [N+1];
      double pcolumn[N+1];
      int i,j,k,l;
      int lag;
      int  z;
      int length;
      double Grid [m+1][m+1];
      double sum;
      double mf[41];

  z=gridsize;

// for (i = 0; i <= L+1 ; i++) {
```

```
//      Att[i] = (double *) malloc((L + 1) * sizeof(double));}



      fin=fopen("/home/ee/tina/emgfiles/programs/aa_ch0.asc","r+");
      fout=fopen("/home/ee/tina/emgfiles/programs/mmi4.asc","w");

      for (i=1 ; i<=N ; i++)
       {
        fscanf(fin,"%d\n", &time[i]);

        //printf("%d\n",time[i]);
       }

 for ( lag=1 ; lag<=40 ; lag++)
 {


 for (i=1 ; i<= L ; i++)
 { for  ( j=1 ; j<=L ; j++)
    {
      Att[i][j]=0;
      }
       }


 for  ( k=1 ; k <= (N-lag) ; k++)
 {
   Att[time[k]+(dist)][time[k+lag]+(dist)]+=1;
  // printf("%d\n",time[k]+(dist));
   };


 for ( i=1 ; i <= m ; i++)
 {  for ( j=1 ; j<=m ; j++)
    {
      sum=0;
      for ( k=1; k<=gridsize ; k++)
        {  for  (l=1; l<= gridsize ; l++)
          {
           if ( Att[((i-1)*z)+k][((j-1)*z)+l]==1)
             {
               sum++;
               }}}
       Grid[i][j]=sum/8000;
```

```
        //printf("%e\n",sum);
        }
        }

    for (k=1 ; k<= m ; k++)
    {
     sum=0;
      for ( l=1 ; l<=m ; l++)
        {
          sum=Grid[k][l]+sum;
        };
       pcolumn[k]=sum/8000;
       //printf("%e\n",sum);
     };


   for (k=1 ; k<=m ; k++ )
   {   sum=0;

       for ( l=1; l<=m ; l++)
         {
          sum=Grid[k][l]+sum;
          };
        prow[k]=sum/8000;
       // printf("%e\n",sum);
    }


  sum=0;
  for ( k=1 ; k<=m ; k++)
  {  for ( l=1 ; l<=m ; l++)
   {
     if ( Grid [k][l] !=0){
     sum=sum+(Grid[k][l]* (double)(log(Grid[k][l]/(prow[k]*pcolumn[l]))));
     //printf("%e\n",Grid[k][l]);
     // printf("%e\n",prow[l]);
     //printf("%e\n",pcolumn[k]);
     //printf("%e\n",(Grid[k][l]*(double) (log(Grid[k][l]/(prow[l]*pcolumn[k])))));
      }
     }
      }
  mf[lag]=sum;
  fprintf(fout,"%e\n",mf[lag]);


}
```

```
  fclose(fin);
  fclose(fout);

}

/*##########################################################################

Program: Calculation of the multifractal dimensions of a time series.

Program description: This program is in C language, and calculates the
multifractal dimensions of an input time series. The embedding dimension and
the lag of the reconstruction are inputs along with the time series. The number
of dimensions to be calculated and the hypercube sizes are chosen by the user.
The output is the array of summation of probabilities.

##########################################################################*/


#include <stdio.h>
#include <stdlib.h>
#include <math.h>
#include <malloc.h>
const int  size=2000;  // size of the time series, usually for one second
                // that is the number of samples per second of EMG

const int embed=2;     // this is the embedding dimension
const int lag=1;       // this is the lag  used in reconstruction of phase space

const int vnum=13;     // this is the number of vels we want to use, change vels variable
const int qmax=20;     // this is the largest moment order we want to use for
                // calculation of the renyi dimentions
const int M=(size-((embed-1)*(lag)));   // number of points in phase space


int main()
{
        FILE  *fin, *fout;
        float time[size+1];
        double distance;
        int i,j,q,v,n,k,t;
        double sum,temp;
        double probs[vnum+1][M+1];
        double pprobs[vnum+1][M+1];
        double cql[vnum+1][(qmax*2)+2];
        double vels[vnum+1];
```

```
        char infile[255];
        char outfile[255];
        int euc;
        int vel;
        double temp2;
        double temp3;

euc=2;


 // initializing arrays

for ( i=1 ; i<=vnum ; i++)
   {for  ( j=1 ; j<=M  ; j++ )
     {  probs[i][j]=1;
        pprobs[i][j]=1;


      }
    }


vels[1]=0.001;
vels[2]=0.002;
vels[3]=0.004;
vels[4]=0.008;
vels[5]=0.016;
vels[6]=0.032;
vels[7]=0.064;
vels[8]=0.128;
vels[9]=0.256;
vels[10]=0.512;
vels[11]=1.024;
vels[12]=2.048;
vels[13]=4.096;


// The vel ranges are defined
/*   for (i=1 ; i<=vnum ; i++ )
      {
       printf("enter  the vel size number  %d\n",i );
       scanf ("%d",&vel);
      vels[i]=vel;
      } */

// This section inputs the time series
```

```
// printf ("please enter the time series filename\n");
// scanf("%s",infile);
 fin=fopen("/home/ee/tina/emgfiles/programs/noise.asc","r+");
 fout=fopen("/home/ee/tina/emgfiles/programs/test.asc","w");
/* if ((fin=fopen(infile,"r+"))==NULL)
   {
   printf("Error opening file.\n");


   }*/


 for (i=1 ; i<=size ; i++)
   {
   fscanf(fin,"%lf\n", &time[i]);

   //printf("%lf\n",time[i]);
   }


/// printf("please enter the name of the output file\n");
// scanf("%s", outfile);


/* if ((fout=fopen(outfile,"w"))==NULL)
  {
   printf("Error opening output file.\n");
  } */


// In this section every point in the phase space is visited
// The number of points which fall in a vel centered in each
// point of the phase space is calculated and enetred in prob array
// all ranges of vel sizes are taken into account in each visit



 for ( i=(((embed-1)*lag)+1) ; i<=size ; i++)
   {
   for (j=(i+1) ; j<=size ; j++)
    {
     if (i!=j)
       {
         //fprintf(fout,"%d %d ",i,j);
         sum=0;
```

```
            for ( n=0; n<=embed-1 ; n++ )
             {

             temp2=(time[i-(n*(lag))]-time[j-(n*(lag))]);

             //printf("%f  %f ",time[i-(n*(lag))],time[j-(n*(lag))]);
            // printf("%e ",temp2);
             sum+= (double)pow(temp2,euc);
              }
            //printf("%e ",sum);
            distance=(double)pow(sum,0.5);
            printf("%e \n",distance);
            for ( k=1 ; k<=vnum ; k++ )
            {
              if (distance>0 & distance<=vels[k])
                { probs[k][i-((embed-1)*lag)]++;
                  probs[k][j-((embed-1)*lag)]++;};
            }

          }
        }
      }



  for (i=1 ; i<=vnum ; i++)
    { for ( j=1 ; j<=M ; j++)
       {
         probs[i][j]=(probs[i][j]/M);

       }
     }

/* for ( i=1 ; i<=vnum ; i++)
   {for  ( j=1 ; j<=M  ; j++ )
     {
     printf("%d %d %e ",i,j, probs[i][j]);


     }
   }  */
```

```
// In this section the probabilities in array probs are taken to powers
// corresponding to the moment orders and  put into array cql


for (v=1 ; v<=vnum ; v++)
  {  for  ( q=0; q<=qmax; q++)
     {
      if (q!=0)
       {
        for ( i=1 ; i<=M ; i++)
          {  pprobs[v][i]=probs[v][i]*pprobs[v][i];
           //printf("%d %d %e ", v,i,pprobs[v][i]);
           }

        sum=0;
        for (i=1 ; i<=M ; i++)
          { sum+=pprobs[v][i];
           // printf("%e ", pprobs[v][i]);
                      }
        cql[v][(qmax+1)+q]=sum;
        //printf("%e ", sum);
        sum=0.0;
        //printf("%e ", sum);
        for (i=1 ; i<= M ; i++)
          {
           if ( pprobs[v][i] != 0 )
             {
              temp3=(1.0/(pprobs[v][i]));
              // printf("%d %d %e ",v,i,temp3);
              sum=temp3+sum;
             //printf("%e ",sum);
             };
          }
        cql[v][(qmax+1)-q]=sum;
       // printf("%e ",sum);
       }

      if (q==0)
       {
        sum=0;
        for(i=1; i<= M ; i++)
          { sum=pow(probs[v][i],0)+sum;}
        cql[v][qmax+1]=sum;
        //printf("%e ",sum);
       }
```

```
      }
    }

/*  for  (i=1 ; i<=9 ; i++)
 {
 for (j=1 ; j<= 41 ; j++)
 {
   printf("%e  %d %d ",cql[i][j],i,j);
   }}
*/

  for ( j=1 ;j<= ((qmax*2)+1)  ; j++)
  {
     for (i=1 ; i<= vnum ; i++)
          {

           cql[i][j]=cql[i][j]/M;

          }
   }


for ( j=1 ;j<= ((qmax*2)+1)  ; j++)
  {
     for (i=1 ; i<= vnum ; i++)
          {

           fprintf(fout,"%e\n",cql[i][j]);

          }
   }


 fclose(fin);
 fclose(fout);

 }
```

```
/*#########################################################################

Program: Calculation of the multifractal dimension for a strange attractor.

Program description: This program is in C language. This program calculates the
multifractal dimension of a known attractor. The embedding dimension of the
attractor and the time series corresponding to the trajectory of each variable
are the inputs. The number of fractal dimensions to be calculated and the hyper
cube sizes are chosen by the user. The output is the array of summation of the
probabilities.

#########################################################################*/


#include <stdio.h>
#include <stdlib.h>
#include <math.h>
#include <malloc.h>
const int  size=15000;  // size of the time series,

const int embed=3;     // this is the embedding dimension


const int vnum=15;    // this is the number of vels we want to use, change vels variable
const int qmax=20;    // this is the largest moment order we wnt to use for
                // calculation of the renyi dimentions

const int delay=10000;
int main()
{
      FILE  *xcoord, *ycoord, *zcoord, *fout;
      double xtime[size+1];
      double ytime[size+1];
      double ztime[size+1];

      double distance;
      int i,j,q,v,n,k,t;
      double sum,temp;
      double probs[vnum+1][size+1];
      double pprobs[vnum+1][size+1];
      double cql[vnum+1][(qmax*2)+2];
      double vels[vnum+1];
      double xdelay,ydelay,zdelay;
      char outfile[255];
      int euc;
      int vel;
```

```
        double temp2;
        double temp3;

euc=2;


 // initializing arrays

for ( i=1 ; i<=vnum ; i++)
   {for  ( j=1 ; j<=size ; j++ )
     {  probs[i][j]=1;
        pprobs[i][j]=1;


      }
    }



// The vel ranges are defined
/*   for (i=1 ; i<=vnum ; i++ )
     {
      printf("enter  the vel size number  %d\n",i );
      scanf ("%d",&vel);
     vels[i]=vel;
     } */

vels[1]=128;
vels[2]=256;
vels[3]=512;
vels[4]=1024;
vels[5]=2084;
vels[6]=4096;
vels[7]=8192;
vels[8]=16384;
vels[9]=22768;
vels[10]=45536;
vels[11]=91072;
vels[12]=182144;
vels[13]=364288;
vels[14]=728576;
vels[15]=1457152;
```

```
// This section inputs the x,y,z coordinates.


 xcoord=fopen("/home/ee/tina/emgfiles/programs/rosslerx.asc","r+");
 ycoord=fopen("/home/ee/tina/emgfiles/programs/rosslery.asc","r+");
 zcoord=fopen("/home/ee/tina/emgfiles/programs/lrosslerz.asc","r+");
 fout=fopen("/home/ee/tina/emgfiles/programs/rosslerdim5.asc","w");


 for (i=1 ; i<=delay ; i++)
   {
    fscanf(xcoord,"%e\n", &xdelay);
    fscanf(ycoord,"%e\n", &ydelay);
    fscanf(zcoord,"%e\n", &zdelay);

    }



for (i=1 ; i<=size ; i++)
   {
    fscanf(xcoord,"%e\n", &xtime[i]);
    fscanf(ycoord,"%e\n", &ytime[i]);
    fscanf(zcoord,"%e\n", &ztime[i]);

    }




// In this section every point in the attractor is visited
// The  number of points which fall in a vel centered in each
// point of the attractor is calculated and enetred in prob array
// all ranges of vel sizes are taken into account in each visit



 for (  i=1 ; i<=size  ; i++)
   {
    for (j=(i+1) ; j<=size ; j++)
     {
      if (i!=j)
        {
```

```
            sum=0;
            sum+=(double)pow(xtime[i]-xtime[j],2);
            sum+=(double)pow(ytime[i]-ytime[j],2);
            sum+=(double)pow(ztime[i]-ztime[j],2);
            //fprintf(fout,"%e\n",sum);
            distance=(double)pow(sum,0.5);
           // printf("%e\n",distance);
            for ( k=1 ; k<=vnum ; k++ )
            {
              if (distance>= 0 & distance<=vels[k])
                { probs[k][i]++;
                  probs[k][j]++;};
             }

          }
        }
      }



  for (i=1 ; i<=vnum ; i++)
    { for ( j=1 ; j<=size ; j++)
       {
         probs[i][j]=(probs[i][j]/size);

       }
     }

/* for ( i=1 ; i<=vnum ; i++)
   {for  ( j=1 ; j<=size ; j++ )
     {
     printf("%d %d %e  ",i,j, probs[i][j]);


     }
    }  */
```

// In this section the probabilities in array probs are taken to powers
// corresponding to the moment orders and put into array cql

```
for (v=1 ; v<=vnum ; v++)
  {  for  (  q=0; q<=qmax; q++)
     {
      if (q!=0)
       {
        for ( i=1 ; i<=size ; i++)
          {  pprobs[v][i]=probs[v][i]*pprobs[v][i];

           }

        sum=0;
        for (i=1 ; i<=size ; i++)
          { sum+=pprobs[v][i];

                        }
        cql[v][(qmax+1)+q]=sum;

        sum=0.0;

        for (i=1 ; i<= size ; i++)
          {
           if ( pprobs[v][i] != 0 )
            {
             temp3=(1.0/(pprobs[v][i]));

             sum=temp3+sum;

            };
          }
        cql[v][(qmax+1)-q]=sum;

       }

      if (q==0)
       {
        sum=0;
        for(i=1; i<= size ; i++)
          { sum=pow(probs[v][i],0)+sum;}
         cql[v][qmax+1]=sum;

       }

     }
  }
```

```
 for ( j=1 ;j<= ((qmax*2)+1)  ; j++)
 {
    for (i=1 ; i<= vnum ; i++)
         {

          cql[i][j]=cql[i][j]/size;

         }
  }


for ( j=1 ;j<= ((qmax*2)+1)  ; j++)
 {
    for (i=1 ; i<= vnum ; i++)
         {

          fprintf(fout,"%e\n",cql[i][j]);

         }
  }


 fclose(xcoord);
 fclose(ycoord);
 fclose(zcoord);
 fclose(fout);

 }
```

```
/*#########################################################################
Program: Generation of the Henon attractor.

Program description: This program generates the x and y variable trajectories
of the Henon attractor. The parameters of the equation and the size of the series
are the inputs. The trajectories are saved in the output files.

#########################################################################*/
#include<stdio.h>
#include<math.h>

#define a 1.4
#define b 0.3
#define N 100000


main()
{
 int k;
 double x[N+1],y[N+1];
 double xmax,xmin,ymax,ymin;
 FILE *fp;
 FILE *xf;
 FILE *yf;

 fp=fopen("henon.asc","w");
 xf=fopen("xhenon.asc","w");
 yf=fopen("yhenon.asc","w");
 x[0]=0.8;
 y[0]=0.8;
 xmax=0;
 xmin=0;
 ymax=0;
 ymin=0;
 for(k=0;k<N;k++)
 {
  x[k+1]=y[k]+1.0-(a*x[k]*x[k]);
  y[k+1]=b*x[k];

  fprintf(fp,"%lf %lf\n",x[k],y[k]);
  fprintf(xf,"%lf\n",x[k]);
  fprintf(yf,"%lf\n",y[k]);
  if(x[k]>xmax)

  {
    xmax=x[k];
```

```
    }
  if(x[k]<xmin)
  {
   xmin=x[k];
   }
  if(y[k]>ymax)
  {
   ymax=y[k];
   }
  if(y[k]<ymin)
  {
   ymin=y[k];
   }
  }
  fclose(xf);
  fclose(yf);
  fclose(fp);
  printf("\n xmax=%lf xmin=%lf",xmax,xmin);
  printf("\n ymax=%lf ymin=%lf\n",ymax,ymin);
  return;
}
```

```
/*#########################################################################

Program: Generation of the Lorenz attractor.

Program description:This program generates the x, y, and z variable trajectories
of the Lorenz attractor. The parameters of the equation and the size of the
series are the inputs. The outputs are the files with the variable trajectories.

#########################################################################*/
#include <stdio.h>
#include  <math.h>

#define  a  10
#define  b  2.67
#define  r  28
void  RungKutta (double x,double y,double z,double *xnew,double *ynew,double *znew);
unsigned long int N=5000;
main()
{
  double x,y,z,xnew,ynew,znew;
  int i;
  FILE  *frx;
  FILE  *fry;
  FILE  *frz;
  frx=fopen("lorenzx.asc","w");
  fry=fopen("lorenzy.asc","w");
  frz=fopen("lorenzz.asc","w");
  x=12;
  y=12;
  z=34;
  for (i=0;i<N;i++)
  {    RungKutta(x,y,z,&xnew,&ynew,&znew);
       fprintf(frx,"%e\n",x);
       fprintf(fry,"%e\n",y);
       fprintf(frz,"%e\n",z);
       x=xnew;
       y=ynew;
       z=znew;
   }

  fclose(frx);
  fclose(fry);
  fclose(frz);

  }
```

```
void RungKutta(double x,double y,double z,double  *xnew,double *ynew,double *znew)
{
   double d0x,d0y,d0z,d1x,d1y,d1z,d2x,d2y,d2z,d3x,d3y,d3z;
   double xt,yt,zt;
   double dt, dt2,dt3;
   dt=0.01;
   dt2=dt/2;
   dt3=0.3333333333;


   d0x=-1*a*(x-y)*dt2;
   d0y=(-1*x*z+r*x-y)*dt2;
   d0z=(x*y-b*z)*dt2;

   xt=x+d0x;
   yt=y+d0y;
   zt=z+d0z;

   d1x=-1*a*(xt-yt)*dt2;
   d1y=(-1*xt*zt+r*xt-yt)*dt2;
   d1z=(xt*yt-b*zt)*dt2;

   xt=x+d1x;
   yt=y+d1y;
   zt=z+d1z;

   d2x=-1*a*(xt-yt)*dt;
   d2y=(-1*xt*zt+r*xt-yt)*dt;
   d2z=(xt*yt-b*zt)*dt;

   xt=x+d2x;;
   yt=y+d2y;
   zt=z+d2z;

   d3x=-1*a*(xt-yt)*dt2;
   d3y=(-1*xt*zt+r*xt-yt)*dt2;
   d3z=(xt*yt-b*zt)*dt2;

   *xnew=x+(d0x+d1x+d1x+d2x+d3x)*dt3;
   *ynew=y+(d0y+d1y+d1y+d2y+d3y)*dt3;
   *znew=z+(d0z+d1z+d1z+d2z+d3z)*dt3;
     }
```

```
/*#########################################################################
Program: Generation of the Rossler attractor.

Program description: This program generates the x, y, and z variable
trajectories of the Rossler attractor. The inputs are the parameters of the
equations and the size of the series. The output is the files contaning the
variable trajectories.
#########################################################################*/


#include <stdio.h>
#include  <math.h>

#define  a  0.2
#define  b  0.2
#define  c  5.7
void  RungKutta (double x,double y,double z,double *xnew,double *ynew,double *znew);
unsigned long int N=40000;
main()
{
  double x,y,z,xnew,ynew,znew;
  int i;
  FILE  *frx;
  FILE  *fry;
  FILE  *frz;
  frx=fopen("rosslerx.asc","w");
  fry=fopen("rosslery.asc","w");
  frz=fopen("rosslerz.asc","w");
  x=-1;
  y=0;
  z=0;
  for (i=0;i<N;i++)
  {   RungKutta(x,y,z,&xnew,&ynew,&znew);
      fprintf(frx,"%e\n",x);
      fprintf(fry,"%e\n",y);
      fprintf(frz,"%e\n",z);
      x=xnew;
      y=ynew;
      z=znew;
   }

  fclose(frx);
  fclose(fry);
  fclose(frz);

  }
```

```
void RungKutta(double x,double y,double z,double  *xnew,double *ynew,double *znew)
{
   double d0x,d0y,d0z,d1x,d1y,d1z,d2x,d2y,d2z,d3x,d3y,d3z;
   double xt,yt,zt;
   double dt, dt2,dt3;
   dt=0.01;
   dt2=dt/2;
   dt3=0.3333333333;


   d0x=-(y+z)*dt2;
   d0y=(x+a*y)*dt2;
   d0z=(b+x*z-c*z)*dt2;

   xt=x+d0x;
   yt=y+d0y;
   zt=z+d0z;

   d1x=-(yt+zt)*dt2;
   d1y=(xt+a*yt)*dt2;
   d1z=(b+xt*zt-c*zt)*dt2;

   xt=x+d1x;
   yt=y+d1y;
   zt=z+d1z;

   d2x=-(yt+zt)*dt;
   d2y=(xt+a*yt)*dt;
   d2z=(b+xt*zt-c*zt)*dt;

   xt=x+d2x;;
   yt=y+d2y;
   zt=z+d2z;

   d3x=-(yt+zt)*dt2;
   d3y=(xt+a*yt)*dt2;
   d3z=(b+xt*zt-c*zt)*dt2;

   *xnew=x+(d0x+d1x+d1x+d2x+d3x)*dt3;
   *ynew=y+(d0y+d1y+d1y+d2y+d3y)*dt3;
   *znew=z+(d0z+d1z+d1z+d2z+d3z)*dt3;

  }
```